Deep Inelastic Compton Scattering of high energy γ Photons. on an Isoscalar Target.

Philip Noon

Imperial College

Blackett Laboratory

London

Thesis submitted for the degree of

Doctor of Philosophy in the University of London

January 1985.

Abstract

The analysis is presented of events, containing a high p_t photon (1 GeV/c < p_t < 4 GeV/c) in the final state, produced when a ^{6}Li target was exposed to a photon beam of mean energy 80 GeV/c. The events were recorded in a lead-scintillator sandwich calorimeter positioned at about 90° in the γ-nucleon centre of mass.

The inclusive p_t spectrum of the photons is compared to that of π^0's and to those of γ's and π^0's produced with an incident π^- beam and it is concluded that there is a significant contribution due to Deep Inelastic Compton Scattering (DICS). The magnitude of the signal is in agreement with that expected from the standard fractionally charged model of quarks and excludes all integer charged models which predict a signal of more than twice that observed.

The events are then studied topologically and it is found that they exhibit the behaviour that would be expected if most of the signal were caused by the lowest order DICS diagram. There are insufficient events to determine if there is a charge asymmetry in the hadrons accompanying the high p_t photon.

Acknowledgements

I would like to thank Ion Siotis, my supervisor, for his guidance, especially during the last year.

I wish to thank the members of the NA-14 collaboration for their help throughout my time on the experiment and especially the following people: Mark Burchell, Anthony Duane, Paul Gregory, Tejinder Virdee and David Websdale.

I am very grateful to Chris Seez for the time and effort he has spent explaining the intricacies of the Ilsa calorimeter and its analysis, and for providing me with a number of diagrams for use in this thesis.

On a social note, my thanks are due to all those people, who during my stay in Geneva, helped to keep me sane through the week only to undo all the good work at the St. Pauli each Friday night!

Professor Ian Butterworth originally accepted me into the Imperial College HENP group and Professor David Binnie has since accepted the decision without complaint; I am grateful to both of them.

The SERC provided financial assistance during the period of study.

CONTENTS

Photon Hard Scattering 8
1.1 Pointlike Interactions of the Photon. 9
1.2 Hadron-like Interactions of the Photon 9
1.3 QED Compton Scattering 12
1.3.1 The Issue of Quark Charges 13
1.3.2 Non-inclusive effects of DICS 14
1.3.3 Higher order corrections 15
1.3.4 Other contributions to the prompt photon yield . . 18
1.3.5 Indirect background photons 18

The NA-14 Apparatus 20
2.1 Overview 20
2.2 The Beam 22
2.2.1 The Beamline 22
2.2.2 Tagging 25
2.2.3 The Beam Spectrum 27
2.2.4 The π^- beam 27
Secondary beam 27
Tertiary beam 29
2.3 The E.M. Calorimeters 29
2.3.1 OLGA 30
2.3.2 CROWN 31
2.4 Wire Chambers 33
2.5 Hodoscopes and the μ filter 33
G1 34
G2H 35
G2V 35
2.5.1 The muon filter 35
2.6 The Pretrigger (PT1) 35
2.7 The ILSA calorimeter 36
2.7.1 An ILSA quadrant 37
2.7.2 ILSA performance in a test beam 37
2.7.3 Calibration 40
2.7.4 The ILSA high p_t trigger 42

The Inclusive Analysis 44
3.1 Introduction 44
3.2 General facts 44
Geometry 44
π^0 separation 45
Energy-p_t correlation 45
Parent-child effect 45
3.3 Data sample 45
3.4 The VDM Monte-carlo 46
3.4.1 QED Compton Simulation 47
3.5 Pattern recognition and photon reconstruction 48
3.6 The Analysis 49
3.7 π^0 Analysis 50
3.8 Single photon analysis 50
3.8.1 μ rejection 50
3.8.2 Shower Development Cuts 52
3.8.3 Merged π^0 rejection 52

3.9 Normalization - methods used. 55
3.10 Normalization - counting hadronic events. 56
3.10.1 Pion beam 57
3.10.2 γ beam 58

The Inclusive Results 60
4.1 Objections to the use of π^- beam. 60
4.2 The π^- beam p_t plots. 62
4.3 Comparison of γ beam and π^- beam data 64
4.4 Interpretation of the inclusive result 67

The Enrichment of the Data. 69
5.1 The QED monte-carlo 69
5.2 Event Reconstruction 70
5.3 Enrichments 71
5.3.1 Merged π^0's 72
5.3.2 Recupperation of γ's missed in ILSA 72
5.3.3 Making π^0's with γ's in OLGA and CROWN 76
5.3.4 Electrons from photon conversion in the target . . 77
5.4 Assessment of the enrichment achieved. 79
Merged π^0's 81
Relaxation of reconstruction conditions 83
π^0's made with OLGA,CROWN 83
Electrons from photon conversion 83

Topology and Charge Asymmetry in DICS events. 85
6.1 Introduction 85
6.2 Topological Aspects 86
6.2.1 Acceptance Correction 87
6.2.2 Azimuthal Distributions 89
6.2.3 A More Sophisticated Measure 94
6.2.4 A Lund Clustering Algorithm (LUCLUS) 97
6.3 Charge Asymmetry 100
6.4 Conclusions 102

References 105

TABLES

1. NA-14 Beam Parameters 25

2. Comparison of two ways of evaluating DARM hadronic acceptance. 57

3. Sensitivities (evts/nb) as calculated by the DARM method. 59

4. Fate of the 'other' γ from π^0 decay in candidate γ events 72

5. Measured and theoretical origin of events above

2.45 GeV/c. 81

6. The LUCLUS jet finding results. 100

7. Asymmetry results using the p_t definition of leader 102

8. Asymmetry results using the energy definition of leader . . 102

FIGURES

1. Lowest Order Pointlike Interactions of the Photon 10

2. The photon interacting via its anomalous structure function. 11

3. The photon interacting as a vector meson 12

4. Processes calculated by Aurenche et al (ref 25). 16

5. Corrections to DICS as a fraction of Born contribution. . . 17

6. Contributions to the inclusive, invariant π^0 cross-section . . 19

7. The NA-14 Apparatus 21

8. A schematic representation of the NA-14 Beamline 24

9. Difference between tagging energy and elastic ψ energy . . 26

10. Elastic ψ energy spectrum 28

11. The calorimeters as viewed from the target 30

12. Peyrou Plot for beam energy 100 GeV. 31

13. One cell of OLGA 32

14. The geometry of the beam-killers and moustaches. 34

15. An ILSA quadrant. 38

16. ILSA response as a function of energy in electron test beam. 39

17. Response of ILSA to electrons and hadrons. 41

18. ILSA $\gamma\gamma$ Mass plots. 51

19. The CUTUP algorithm - finding the most significant dip. . 54

20. Distribution of $P = d_{meas}/d_{exp}$ 55

21. Comparison of 'clean' and 'dirty' π^- beams. 62

22. The construction of π^- beam plots. 64

23. Comparison of π^- beam and γ beam p_t spectra. 65

24. The comparison of $\gamma N \rightarrow \gamma X$ with theory. 68

25. $\gamma\gamma$ mass plot in (1,1) quadrants with relaxed energy cuts 74

26. 'photon'-charged track distance in projection. 76

27. $\gamma\gamma$ invariant mass plots 78

28. P/E for charged tracks hitting the calorimeters. 79

29. Angular distribution of electrons about the trigger particle. 80

30. Fraction of events rejected by enrichment as function of p_t 82

31. Correcting for moustache acceptance in $\Delta\phi$ plots. 88

32. Azimuthal distribution of charged tracks 90

33. $\Delta\phi$ distributions for trigger $p_t > 1.5$ GeV/c. 91

34. The extraction of ε from $\Delta\phi$ distributions. 92

35. ξ as a function of $\Delta\phi$ for $p_t > 2.45$ GeV/c. 95

36. X-distribution for γ events with $p_t > 2.45$ GeV/c 96

37. X-distributions at (a) all p_t, (b) $p_t > 2.45$ GeV/c. 97

38. Evaluation of ε from X-distributions. 98

39. Asymmetry as a function of p_t. 103

- Chapter 1 -

PHOTON HARD SCATTERING

It has been accepted for many years that nucleons are composite particles. Their constituents have been probed in lepto-production experiments[1] and at e^+e^- machines.[2] These interactions all involve the presence of a virtual photon and there is no reason why real photons, coupling directly to nucleon constituents, should not initiate similar events.

One such interaction, Deep Inelastic Compton Scattering (DICS),[1] the subject of this thesis, was first suggested as a means of investigating nucleon structure by Bjorken and Paschos in 1969.[3] Until recently, however, it had not been possible to study the process in a favourable kinematic region with sufficient sensitivity to measure the small effects predicted. Since 1982, NA-14 has been recording data with a high energy, high intensity photon beam which makes possible just such an investigation.

This thesis describes the analysis and interpretation of events containing a high p_t photon detected by the Imperial College Lead Scintillator Array (ILSA) which covered angles of about 90° in the γ-nucleon centre of mass. It begins with a chapter which briefly sketches the various aspects of photon interactions with emphasis on the fundamental knowledge which can be gleaned from those point-like

---

[1] This process is also referred to in this thesis as QED Compton Scattering (QEDC).

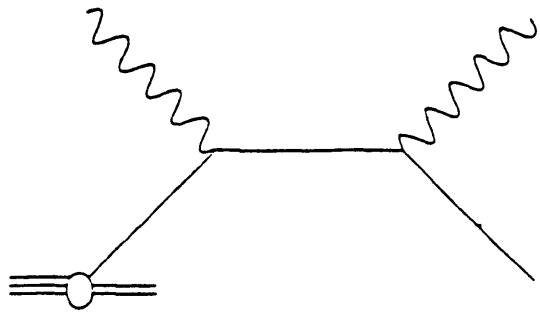
processes producing a prompt photon in the final state.

1.1 Pointlike Interactions of the Photon.

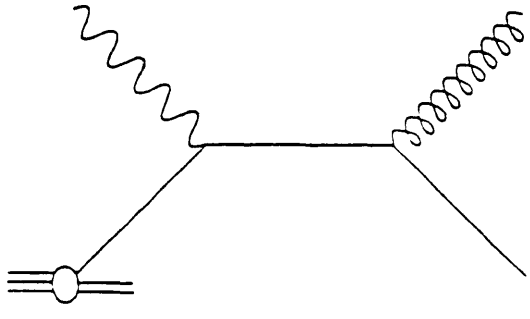
The three simplest processes involving direct coupling of the incident photon to partons are shown in figure 1. The first of these is DICS, simple Compton scattering from a quark. Replacing the final state photon by a gluon gives the so-called QCD Compton diagram (QCDC). QCDC occurs at a rate ~ α_s/α_{qed} times higher than QEDC but is more difficult to recognise since the radiated gluon fragments into a jet whereas the photon of QEDC appears in the final state. Third, by replacing the virtual photon of Bethe-Heitler pair production by a gluon one obtains the Photon-Gluon fusion diagram. This is topologically indistinguishable from QCD Compton producing 2 jets plus target fragments in the laboratory. Since they occur at the Born level, all three processes are relatively easy to calculate, the principal inputs being the structure functions of the nucleon. Measurement of QCDC and γ-g fusion would constitute an important test of QCD and NA-14 is currently engaged in trying to extract from the data information on these processes.

1.2 Hadron-like Interactions of the Photon

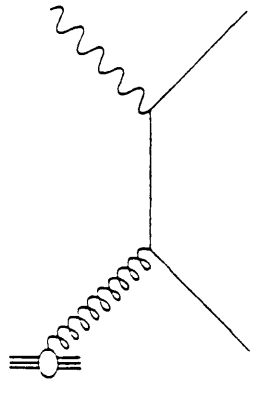
As well as coupling directly to the partons of the target, the photon can interact via fluctuations to a quark-antiquark pair (the photon structure function) . The photon structure function can be divided into two distinct parts. Figure 2 shows the photon interacting via its 'anomalous' structure function. In this case the photon fluctuates into a quark and an antiquark pair which do not interact with each other. One of the quarks then interacts with the target. This part



(a) QED Compton scattering



(b) QCD Compton scattering



(c) γ-g fusion

Figure 1: Lowest Order Pointlike Interactions of the Photon

of the structure function can be calculated by a number of methods[4-7] and shows a $\ln Q^2$ dependence which accounts for its being termed anomalous.

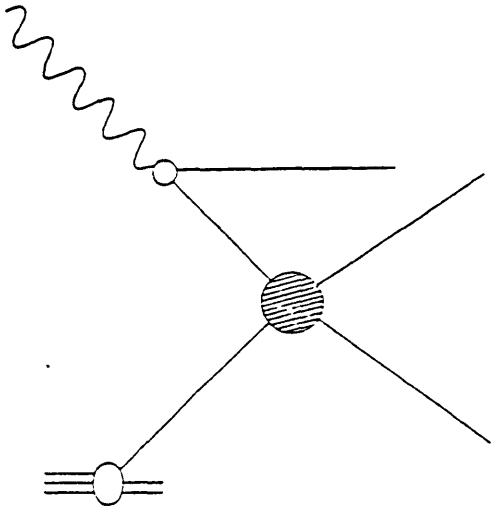


Figure 2: The photon interacting via its anomalous structure function.

If, after the formation of the quark-antiquark pair, gluons are exchanged, a structure function is built up and the photon becomes effectively a vector meson (figure 3). This is the most important contribution to the photon's hadronic interaction cross section.

The photon spends ~ $\alpha_{qed} \approx 1/137$ of the time behaving in this manner and hence its total hadronic cross-section is ~1% of that of a vector meson. This fact is used throughout the analysis to provide a model for non-pointlike processes. A vector meson, the ρ for example, can be considered to be a linear combination of π^+ and π^-. Hence, if the reactions

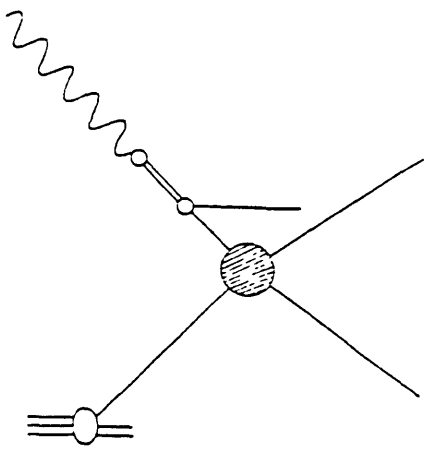


Figure 3: The photon interacting as a vector meson

$$\pi^{\pm}N \rightarrow \pi^{0}X \qquad (1.1)$$

are measured, then the VDM contribution to $\gamma N \rightarrow \gamma X$ can be determined. In fact, since processes (1.1) have been experimentally determined to have the same cross-section,[8] it is necessary only to measure one of them. This part of the structure function behaves in the conventional manner i.e. $\sim 1/\ln Q^2$. A comprehensive review of this Vector Dominance Model (VDM) is given elsewhere.[9]

1.3 QED Compton Scattering

This thesis concerns the experimental observation of Deep Inelastic Compton scattering. It is interesting in itself to demonstrate the existence of the effect but there is the added benefit that a

measurement of the QED Compton cross section may provide a direct determination of the quark charge.

1.3.1 The Issue of Quark Charges

The standard theory assigns to quarks fractional charges.[2] It is possible however to construct theories in which quarks are assigned integer charges (ICQ theories) and several have been proposed. The simplest of these ICQ theories is that of Han and Nambu[10,11] but this suffers from the difficulty of not being renormalisable and so is not an attractive proposition. A theory which includes integer charged quarks and maintains the exact low energy symmetry of the standard model ($SU(3)xU(1)_{em}$) has been suggested[12-14] but this is theoretically rather contrived. The most popular of the ICQ theories is that based on the spontaneously broken colour gauge theory $SU(3)xU(1)_{em}$. This model was first put forward by Pati and Salam[15] and has since been taken up by numerous authors.[16-20] The symmetry is broken at some low energy to produce integrally charged quarks and massive charged gluons. In this theory, the electromagnetic current J_i can be written as

$$J_i = J_f + MJ_8 \qquad (1.2)$$

where $M = (m_g^2/m_g^2-q^2)$

J_f is the em current in the FCQ model

J_8 is a colour octet contribution

At energies well below the colour threshold E_c, only colour singlet processes are relevant and so the theory gives the same answers as the standard fractionally charged theory in first order electromagnetic interactions. However, in interactions involving two photons, the octet part contributes and the two theories have different

---

[2] This theory is referred to hereafter as the fractionally charged quark model (FCQ).

results.

$$\langle J_i J_i \rangle_1 - \langle J_f J_f \rangle_1 = M^2 \langle J_8 J_8 \rangle_1 \qquad (1.3)$$

where $\langle \ldots \rangle_1$ indicates a singlet contribution

From equation 1.2 it can be seen that processes involving a photon of negative q^2 the octet contribution will be suppressed and the predictions tend to those of the fractionally charged model. Hence, it is difficult to distinguish between the two theories in reactions like $\gamma^*\gamma \rightarrow$jets at e^+e^- machines.[21] Interactions involving two real photons are required. One such process is DICS; $\gamma N \rightarrow \gamma X$. In this case it is necessary to assume that the interaction is instantaneous so that there are no colour fluctuations (and hence no charge fluctuations since the 'gluons' of the integer charge theory are charged).[22-24]

It is clear from the above that it is difficult for measurements of processes involving even two real photons to conclusively distinguish between integrally and fractionally charged quarks. It is however possible to rule out specific theories, including the standard fractionally charged theory, if their predictions differ from experimental observation.

1.3.2 Non-inclusive effects of DICS

As well as manifesting itself in the inclusive cross section, QED Compton produces final state hadrons with some interesting and identifiable features. Figure 1a has a very distinctive topology. If the presence of target fragments is ignored, the final state consists simply of a single jet recoiling against a photon. Even after allowing for fragmentation, this should still be experimentally observable.

In the standard FCQ theory, when scattering photons from an isoscalar target, u quarks are favoured over d quarks by a factor of 16. Consequently, at high p_t, where the data should be rich in events of this type, one would expect to see more positive tracks than negative leading the spray of hadrons which balances the scattered photon in p_t.

Observation of these effects would give 'independent' support to the existence of a prompt photon signal.

1.3.3 Higher order corrections

A number of higher order corrections to the simple QEDC diagram of figure 1a have been calculated by Aurenche et al.[25] They have calculated various contributions from diagrams of the types shown in figure 4.

The contribution to the single photon yield in ILSA of each category as a fraction of the Born contribution is shown as a function of p_t in figure 5. They are not negligible but are sufficiently small at high p_t to suggest that corrections of even higher order can be safely disregarded. The magnitude of these results is confirmed by Duke and Owens.[26]

In the gauge ICQ model discussed above the lowest order diagrams have been calculated but there exists no determination of the contributions of higher orders. The ICQ Born contribution is proportional to[27]

$$\sigma \propto \frac{1}{3} \sum_f \left[\sum_c Q_{fc}^2 \right]^2 \qquad (1.4)$$

whereas that of the fractionally charged model varies according to

$$\sigma \propto 3 \sum_f Q_f^4 \qquad (1.5)$$

where the summation is over flavour f

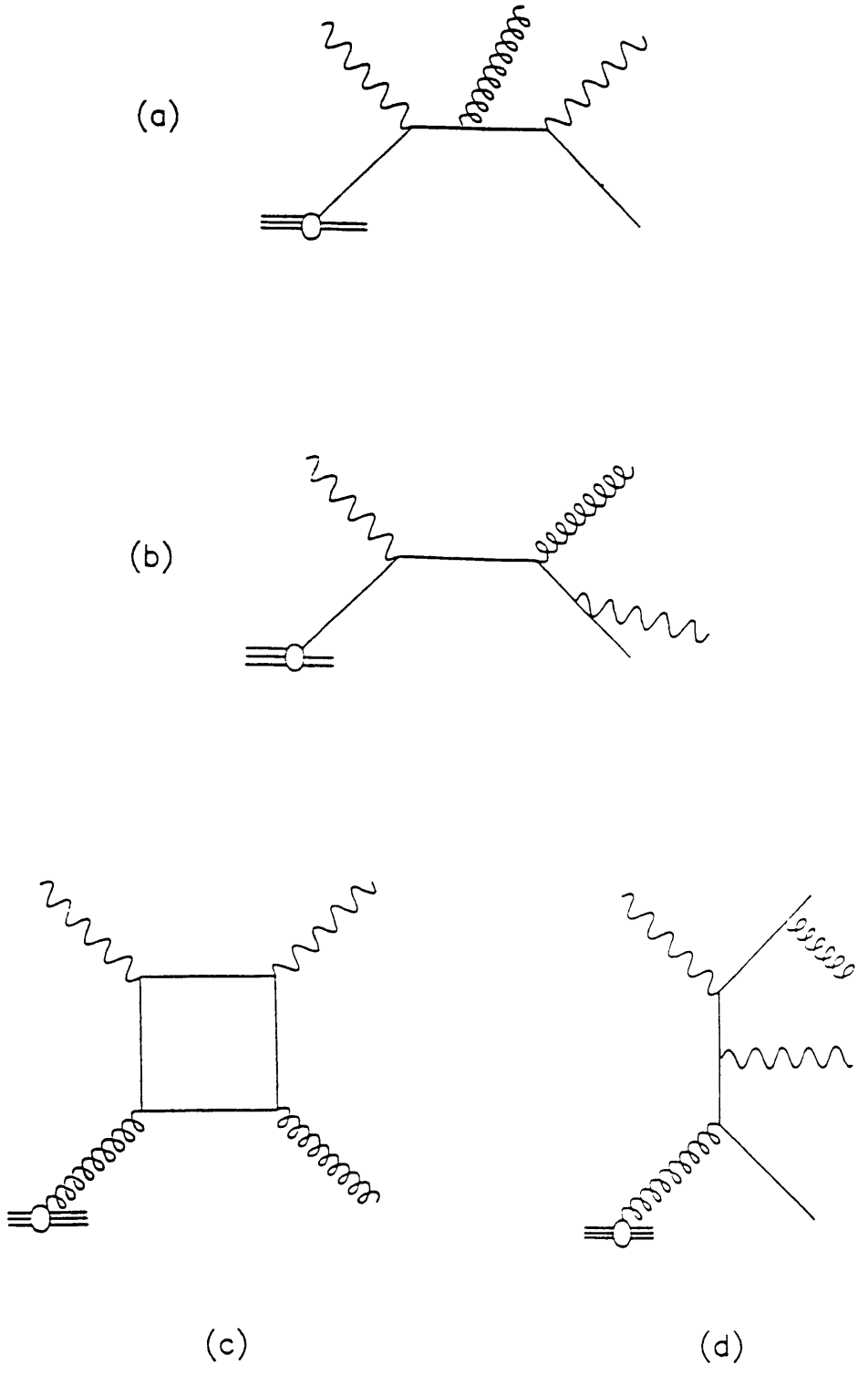


Figure 4: Processes calculated by Aurenche et al (ref 25).

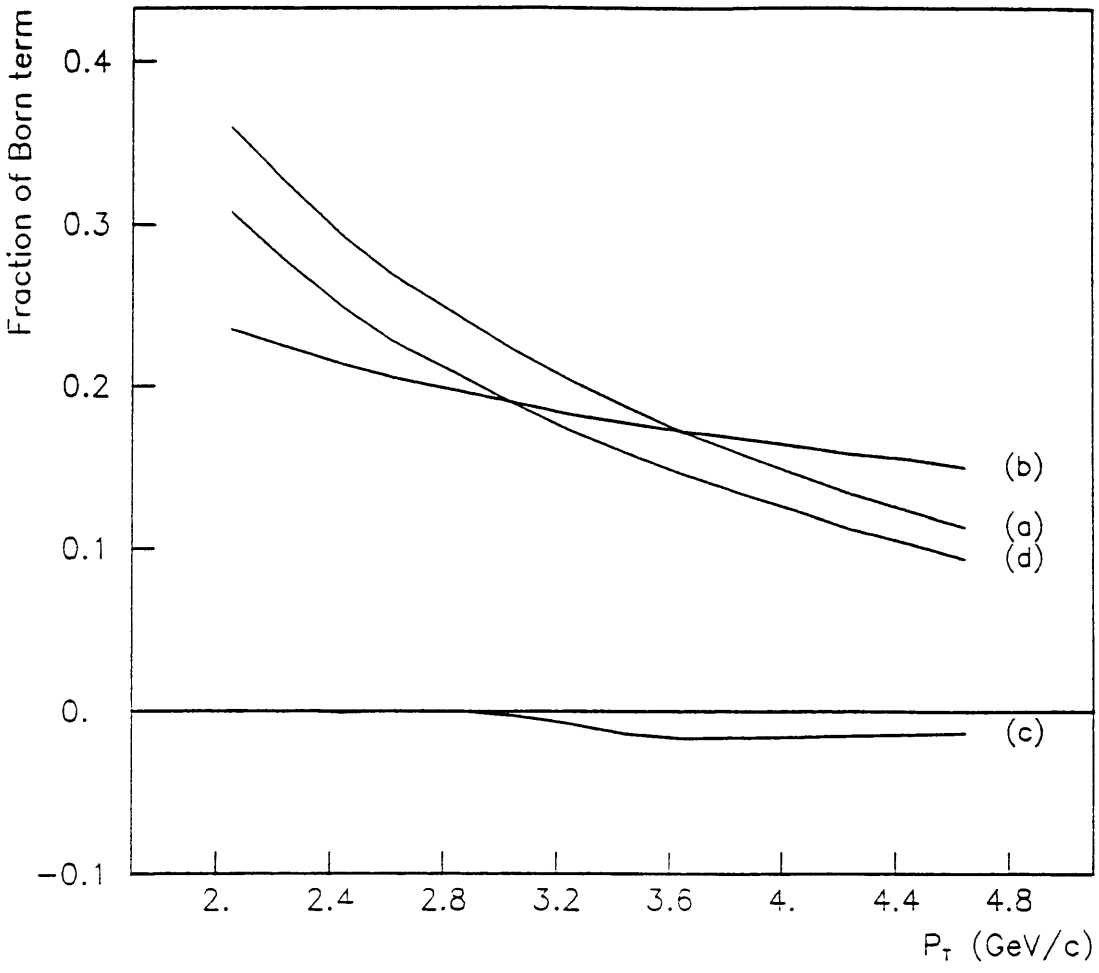


Figure 5: Corrections to DICS as a fraction of Born contribution. (a),(b),(c),(d) refer to the categories of diagrams shown in figure 4.

This means that the ICQ model predicts a Born contribution to the prompt photon yield 2.65 times greater than that predicted by the standard model. One would expect that the higher order corrections would contribute positively to the cross-section thus making the true prediction even greater than this.

1.3.4 Other contributions to the prompt photon yield

There are two sources of direct photons from the hadron-like interactions of the photon.

1. The contribution from the anomalous part of the photon structure function has been calculated in both reference 26 and by Tu and Wu.[28] Both find that the contribution is small at high p_t.

2. There is some prompt photon production in hadron-hadron interactions and hence the meson-like component of the photon will contribute to the overall yield. However, the effect is small when compared to the rate of photons due to DICS.

1.3.5 Indirect background photons

Most photons in the final state will be due to the decay of neutral mesons like the π^0,η etc. It is necessary experimentally to try to reconstruct the mesons and thus eliminate the photons from the list of QEDC candidates. Nevertheless, there will still remain substantial pollution of the prompt photons by these decay products. The inclusive invariant cross-section for π^0 production from 3 sources has been calculated[29] and the results are shown as a function of p_l for p_t = 3 GeV/c in figure 6.

The relevant value of p_l for ILSA is about 25 Gev/c and it can be seen that by far the largest contribution at this p_l is from VDM interactions. This strongly suggests that π^0 photoproduction can be considered to be due to the same processes as produce π^0 in a pion beam and hence that the indirect background to prompt photon

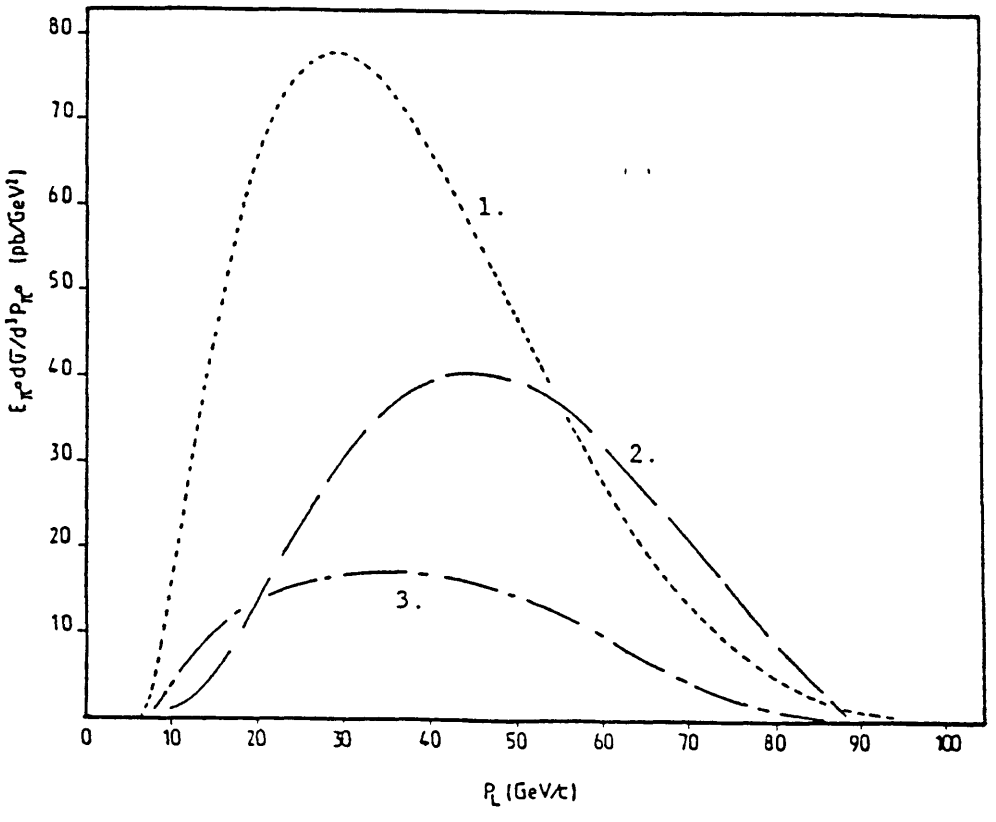


Figure 6: Contributions to the inclusive, invariant π^0 cross-section as a function of p_l for p_t = 3 GeV/c due to:

1) VDM.
2) The photon's anomalous form factor.
3) Pointlike interactions.

production in a photon beam will differ from the same background in a pion beam by a numeric factor only. This fact is used throughout the analysis presented in this thesis.

- Chapter 2 -

THE NA-14 APPARATUS

2.1 Overview

The NA-14 apparatus is shown in figure 7. Photons are incident on an isoscalar ^{6}Li target which sits in the field of the AEG magnet. The target is 10% of a radiation length and hence a large number of low energy electromagnetic pairs is produced. These are swept out of the spectrometer by the 0.8 Tm integrated field in the AEG. The gap between the AEG and the larger (3.2 Tm) Goliath magnet is taken up by a series of Multi-Wire Proportional Chambers (collectively called STACK 1) and an electromagnetic calorimeter (the CROWN). The regions covered by the AEG and Goliath contain no detectors. There are two reasons for this. First, the low energy electromagnetic pairs would spiral in the magnetic fields, creating difficult operating conditions for the chambers and many spurious hits. Second, the tracking algorithms are made easier by avoiding having to do pattern recognition and track fitting in high (non-uniform) field regions.

After the exit of Goliath there is a large area chamber used for triggering on high p_t hadrons. It has a cathode pad readout system which gives 2-dimensional information on the position of particles. The tracks are pinpointed to an accuracy of about 2cm. Following this is STACK 2, a second collection of MWPC's, and a hodoscopic

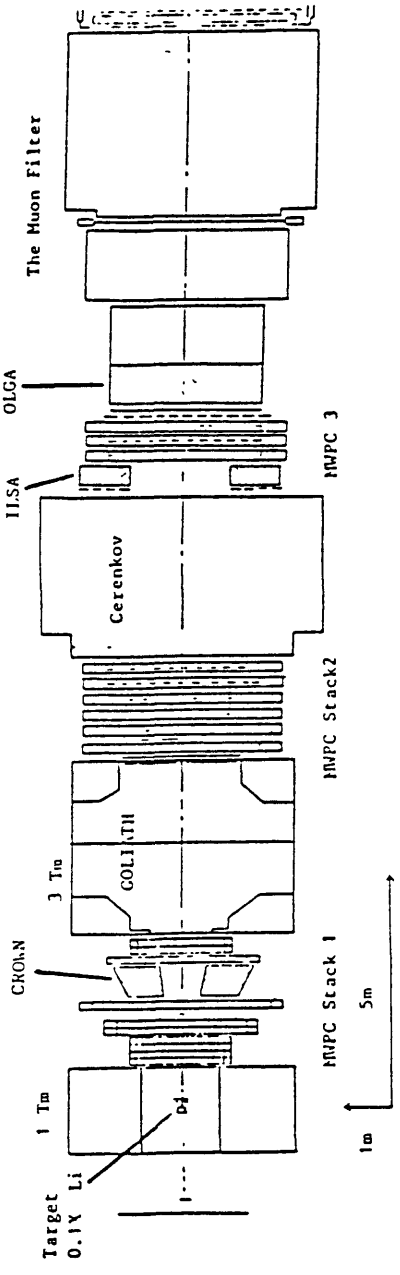


Figure 7: The NA-14 Apparatus

Cerenkov counter. The Cerenkov was not fully operational in 1982, when most of the data analysed here was recorded, and is not used in the analysis. Beyond the Cerenkov lie the two electromagnetic calorimeters, ILSA and OLGA, of interest in the study of QED Compton. Between them are the lever arm chambers which are used to increase the charged track momentum resolution. Finally, beginning more than 15 m downstream of the experimental target is the muon filter.

Below, those detector components directly relevant to this thesis are described in greater detail.

2.2 The Beam

2.2.1 The Beamline

NA-14 is situated in the BEG (Broadband Electron and Gamma) beam in the CERN North Area. This beam was designed to produce the highest possible flux of photons for a given number of protons incident on the primary target. This is achieved via the classical two step method.

The beamline is shown schematically in figure 8. About 2 10^{12} protons of energy 400 GeV are incident on the 50cm long beryllium primary target during each 2 second spill from the SPS. Approximately 70% of the protons interact producing, amongst other things, high energy π^0's, which decay to produce the primary photon beam. Beryllium, an element of low atomic number, is chosen because such substances have a high ratio of radiation length to hadronic interaction length. This makes efficient use of the proton beam whilst reducing the probability that a photon will interact within

the target. Its length is a compromise between these two conflicting objectives.

Charged particles emerging from the production target are deflected by sweeping magnets into dumps consisting of 4m of iron. Fourteen metres downstream the neutrals (γ's, K^0's, n's, ν's) encounter a 4mm thick lead converter. The low ratio of radiation length to interaction length ensures a high flux of high energy electromagnetic pairs with a low contamination from charged particles produced by interactions of the neutral hadrons. Forty percent of the photons convert producing pairs of mean energy 140 GeV. While a converter of greater thickness would increase the flux, it would also lead to more hadron contamination.

The electrons so produced are swept around a chicane by five magnets, the positive and remaining neutral particles being dumped in a 5m iron wall. Electrons are used in preference to positrons to reduce the μ contamination. Positive protons produce about twice as many μ^+ as μ^-. Following the chicane the electrons are focused by two quadrupole magnets onto a 500 micron lead radiator sheet. Approximately 10% of the electrons produce, by bremsstrahlung, a single high energy photon. A thicker radiator would result in more multiple bremsstrahlung which would seriously degrade the usefulness of the tagging system. The major parameters of the beam are summarised in table 1.

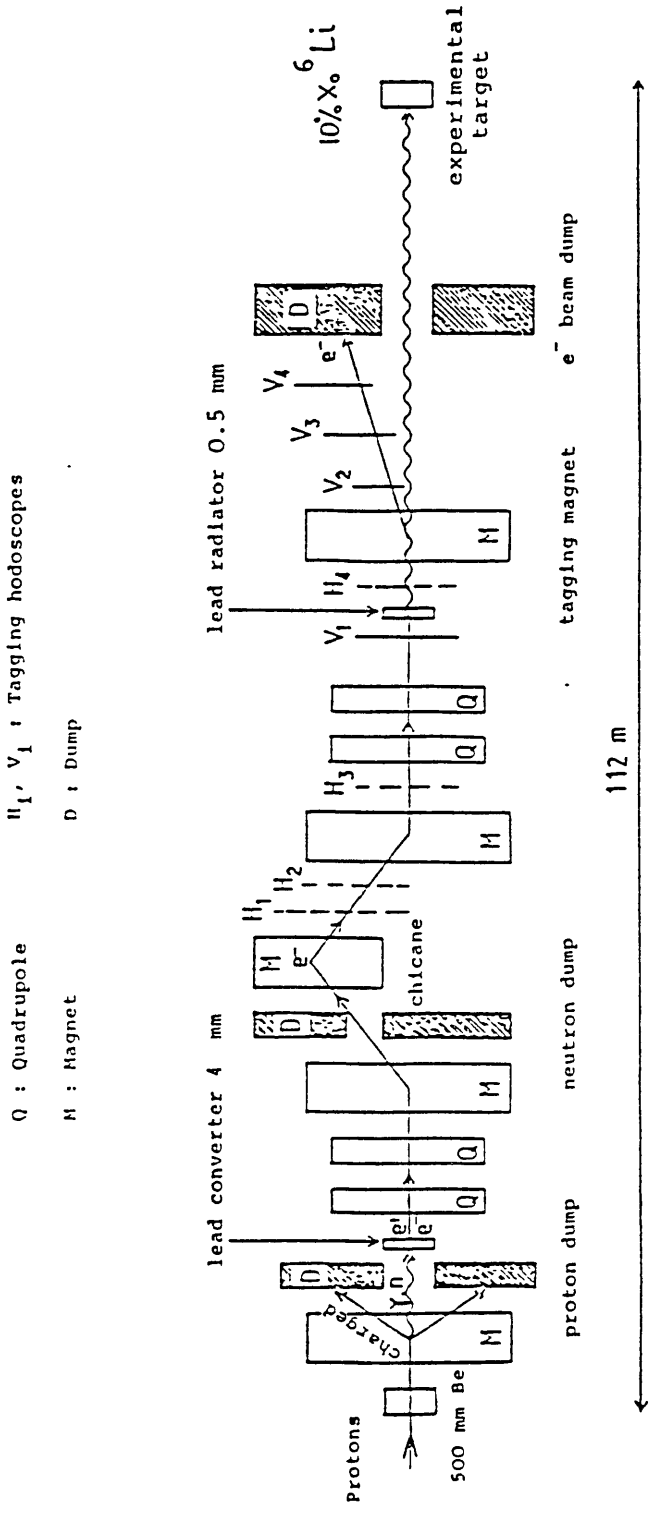


Figure 8: A schematic representation of the NA-14 Beamline

Table 1: NA-14 Beam Parameters

Primary proton beam	intensity	2.0×10^{12}
	energy	400 GeV
Electron beam	intensity	10^8
	energy range	120-250 GeV
Tagged photon beam intensity with a 10% radiation length radiator and photon energy >65 GeV		5×10^6
	mean energy	80 GeV
Beam size (2σ)	horizontal	± 34 mm
	vertical	± 22 mm
Hadronic contamination		$< 10^{-4}$

2.2.2 Tagging

Photons are tagged by measuring the energy of the electron both upstream and downstream of the radiator. The upstream electron is detected by the scintillator hodoscopes H1,H2,H3,H4 (see figure 8) with the help of the scintillator active target information, which can be used to provide an approximate vertex position. In the downstream part the hodoscopes V1,V2,V3,V4 are used along with the Back Tagging Counter (BTC) which is also part of the pretrigger

All the tagging counters are attached to fast photomultipliers and TDC's (providing a timing resolution of about 1 ns) to reduce to a minimum the number of multiple solutions. Scintillator hodoscopes are used in preference to wire chambers because of the intensity of the electron beam. The energy resolution of the tagging is good as can be seen from figure 9 which shows the difference between the

tagging energy and the energy of elastic ψ's measured in the chambers (in the μμ channel). The long positive tail is due multiple bremsstrahlung. The tagging system produces at least one solution for 70% of triggers but in only ~30% does it produce a single unambiguous solution. For this reason the tagging information has not been used in the analysis presented in this thesis.

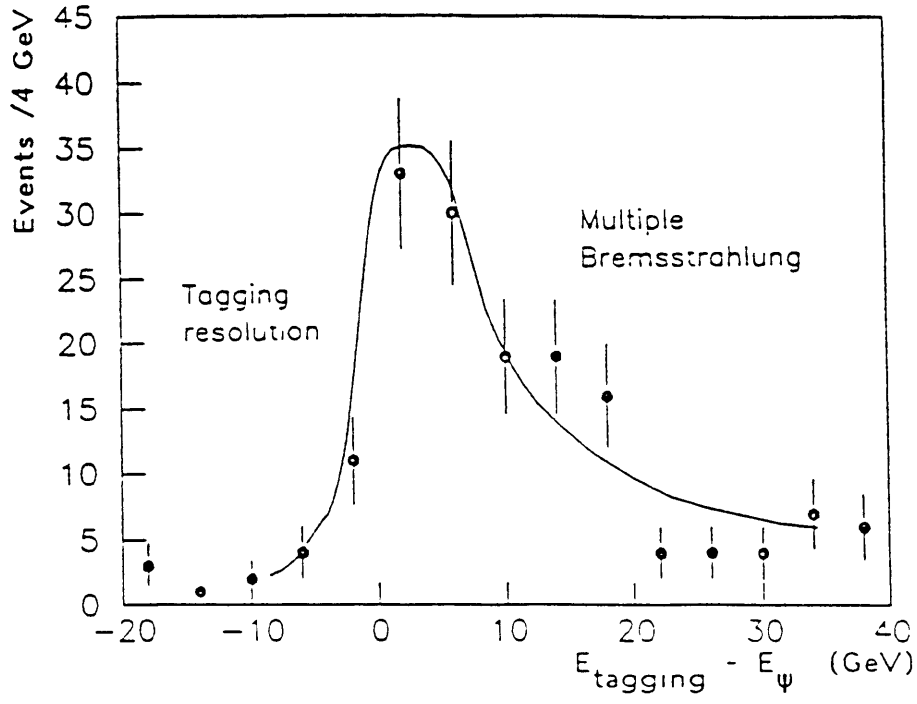


Figure 9: Difference between tagging energy and elastic ψ energy At negative values of ΔE the effects of the finite tagging resolution can be seen. At positive ΔE, multiple bremsstrahlung has caused the tagging to record a higher energy than the true energy of the photon causing the trigger.

2.2.3 The Beam Spectrum

The spectrum of incident photons producing triggers is not that measured by the tagging system. This is because the tagging cannot allow for either multiple bremsstrahlung or the possibility that a photon can give a trigger without satisfying the pretrigger requirement if it is in coincidence with another photon which does.

The spectrum as seen by the triggers can be obtained from the elastic ψ's seen in the experiment. The raw,elastic ψ energy spectrum is shown in figure 10a. The acceptance has been calculated using a monte-carlo program and the energy dependence of the cross-section taken from the literature.[30-35] Unfolding these two functions yields the spectrum shown in figure 10b. The solid line is the result obtained from a monte-carlo simulation of the beam production process allowing for the possibility of multiple bremsstrahlung and γ's in random coincidence.

This spectrum is used throughout the analysis as the input to all monte-carlos requiring the beam energy.

2.2.4 The π^- beam

Pion beams produced by 2 different methods have been used in the experiment. A 'clean' beam of secondary π^-'s was the usual beam but data was also taken with a 'dirty', tertiary π^- beam to try to reproduce the μ flux which accompanies the γ beam.

Secondary beam: This is produced by switching off the magnet directly before the proton dump (figure 8) and removing the 4 mm lead converter. π^- are transported to the experiment in the same way as are e^- when using a γ beam. The primary proton intensity is very much lower than in γ beam mode because the π^-

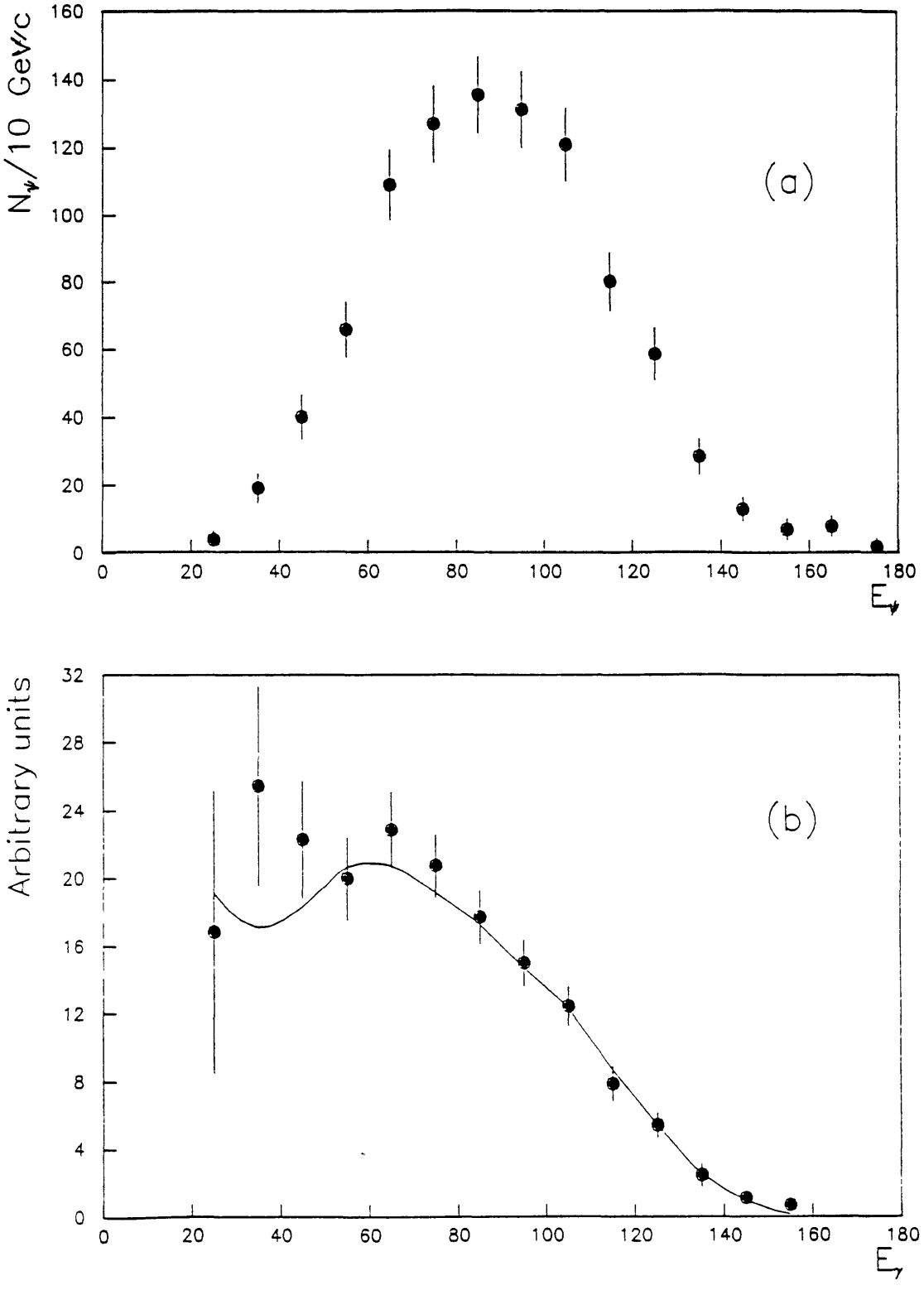


Figure 10: Elastic ψ energy spectrum (a) raw (b) with energy dependence of cross-section and acceptance unfolded.

interaction cross-section is so much greater than is that of the γ beam. In consequence the μ halo is very much reduced compared to the photon beam.

Tertiary beam: Starting from the γ beam setup, the lead converter is removed. K_L^0 and Λ decays then provide a source of π^-'s. The incident proton beam is of the same intensity as it is in γ beam mode because the number of π^-'s produced per primary proton is so much smaller than in the case of the 'clean' beam. A lead brick is inserted after the chicane to remove electrons due to conversions in the air.

The resulting π^- beam has the same muon contamination as the photon beam.

2.3 The E.M. Calorimeters

In the study of DICS the widest possible coverage of electromagnetic calorimetry is necessary not only to increase the acceptance to candidate γ's but also to enable reconstruction of π^0's which would otherwise contaminate the sample. NA-14 has 3 calorimeters for this purpose, each different in construction, providing coverage of ±300 mrad in the lab. Figure 11 shows how the calorimeters appear to a photon emerging from the target and on figure 12 the kinematic coverage of the calorimeters is indicated for an incident beam energy of 100 Gev.

The ILSA calorimeter is discussed fully in section 2.7. The forward and intermediate calorimeters are described below.

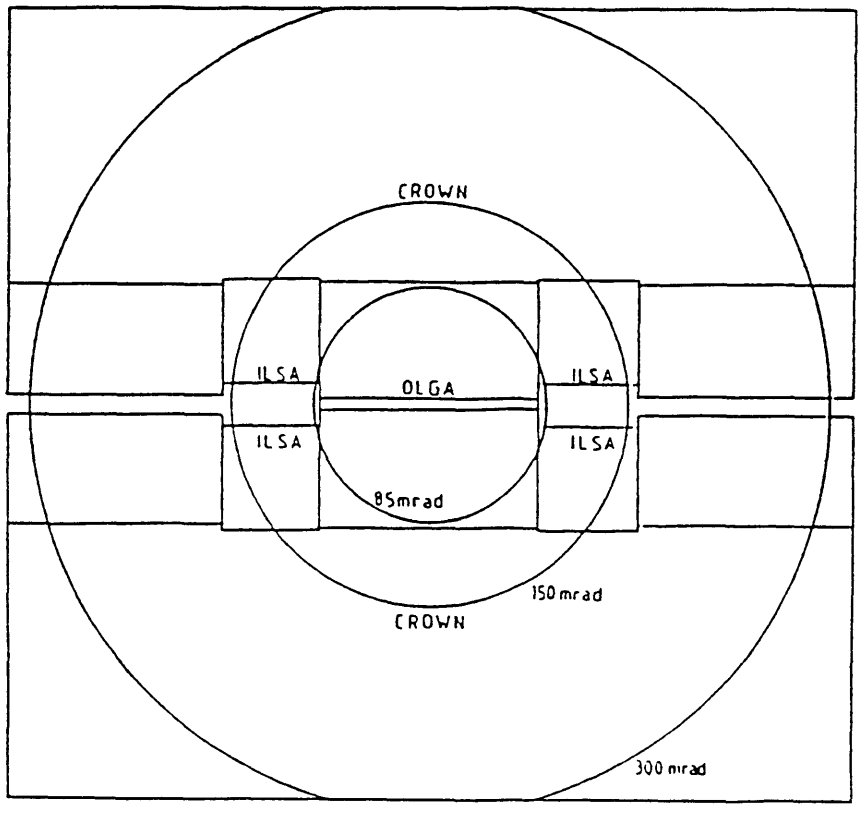


Figure 11: The calorimeters as viewed from the target

2.3.1 OLGA

OLGA covers the forward region of the spectrometer, to about ±80 mrad in the lab. It is situated 15 m downstream of the experimental target and consists of 344 lead glass blocks, each 18.5 radiation lengths deep and presenting an area of 14 x 14 cm^2 to the oncoming particles. The horizontal plane containing the beam axis is not covered because the very high flux of pairs darkens the glass. In front of the blocks lies a position detector, Penelope, comprising two orthogonal planes of scintillator fingers, 1.5 cm wide. In front of Penelope is an active lead glass converter, 3 radiation lengths

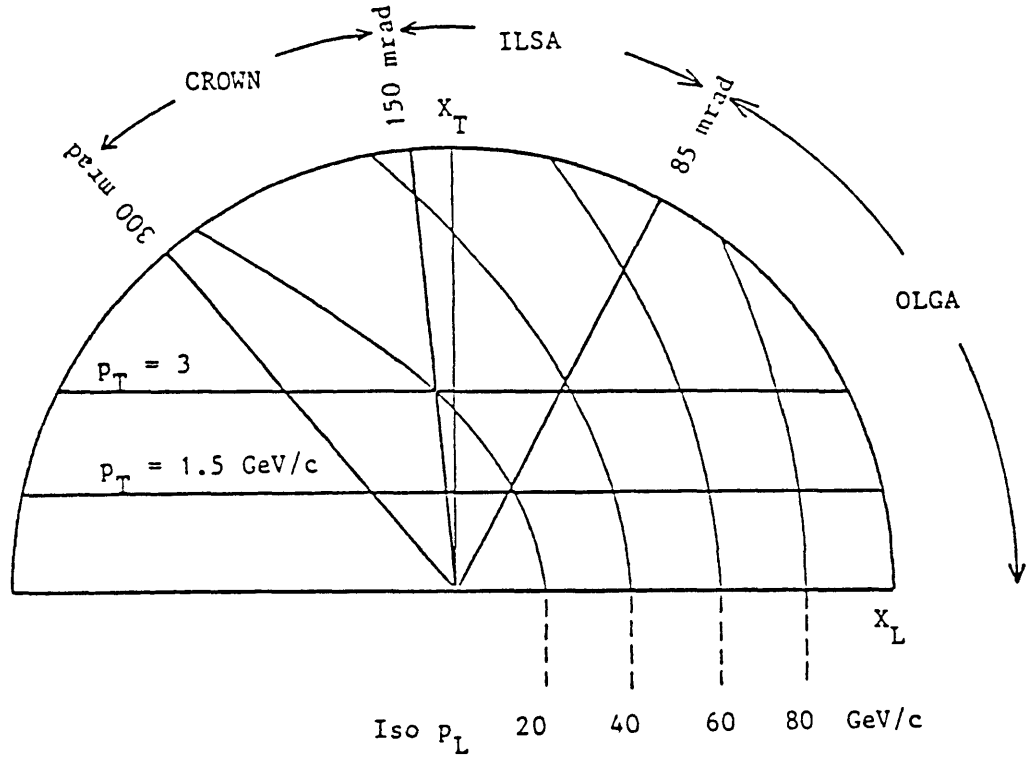


Figure 12: Peyrou Plot for beam energy 100 GeV.

$x_t = p_t/p^*_{max}$

$x_l = p^*_l/p^*_{max}$

and p^*_{max} is the maximum possible energy of a produced particle in the centre of mass ($\approx \sqrt{s}/2$).

thick, and before that an array of veto counters, two for every three lead glass blocks. The layout of one cell of the OLGA calorimeter is illustrated in figure 13.

2.3.2 CROWN

Like OLGA the CROWN is a lead glass array, but here dimensions of the constituent parts are smaller because of the close proximity to the target (~2.5m). The blocks have an area of 9 x 9 cm² and the

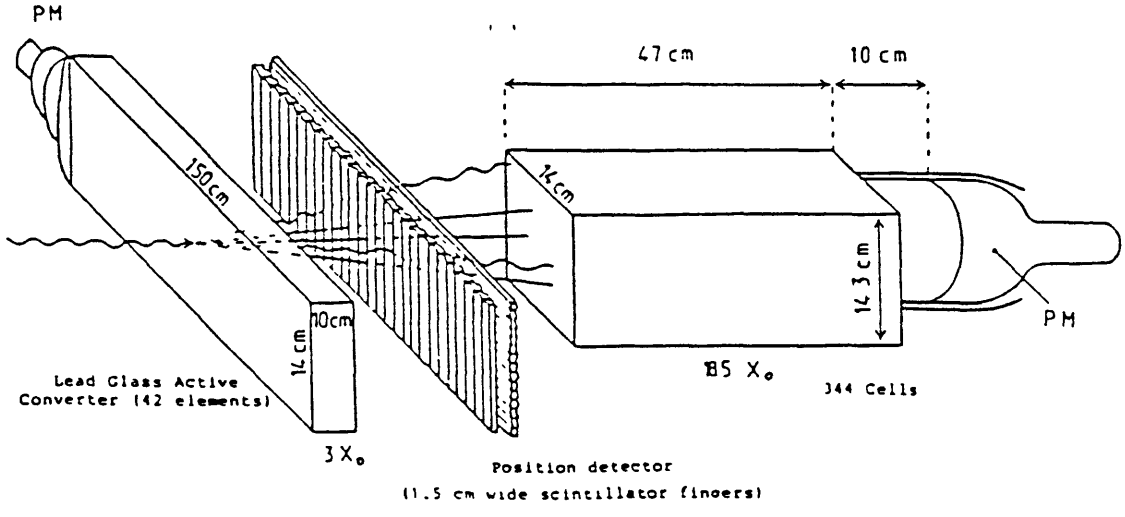


Figure 13: One cell of OLGA

position detector Kali (again consisting of orthogonal scintillator planes) has a finger width of 8mm.[3] Instead of an active converter, CROWN has an inactive lead converter sheet, 5 radiation lengths thick. This is used in preference to lead glass in order to minimise the lateral extent of showers when they strike Kali and hence maximise the capacity to identify π^0's.

The thickness is determined by the need to ensure photon conversion before Kali to enable a strong rejection against neutral hadrons whose showers develop later.

---

[3] The photons from the symmetric decay of a 40 GeV π^0 are separated by 16mm when they hit CROWN.

2.4 Wire Chambers

The charged particle tracking devices are situated between and downstream of the two magnets. The very high flux of pairs rules out the use of drift chambers and only proportional chambers are utilised.

Stack 1 lies immediately downstream of the AEG. It consists of 7 standard MWPC's plus 5 small but very fast chambers, 40 planes in all. All chambers are insensitive in the beam region and the larger chambers have, in addition, 'moustaches' (figure 14) , which have an independent power supply. In the γ beam the moustaches are left inactive to avoid the problems associated with a very high flux of e^+e^- pairs. The small fast chambers (active area 25cm x 20cm) are intended to compensate for the loss of hit wires in the moustache region.

Stack 2 consists of 6 more chambers, directly beyond Goliath. They contain a total of 24 planes, six of which have a very large area (~6m^2) to catch high angle tracks emerging from Goliath.

Finally, the lever arm comprises 3 hexagonal chambers of 3 planes each. These are not utilised in the pattern recognition, their sole use being to increase the precision of momentum measurement.

2.5 Hodoscopes and the μ filter

Immediately following the Li target is the scintillator active target; two rows of small vertical scintillators, 2 mm wide and 6 mm thick. Its primary use is as part of the pretrigger, a signal indicating that an interaction has probably taken place in the target.

There are three large scintillator hodoscopes in the experiment.

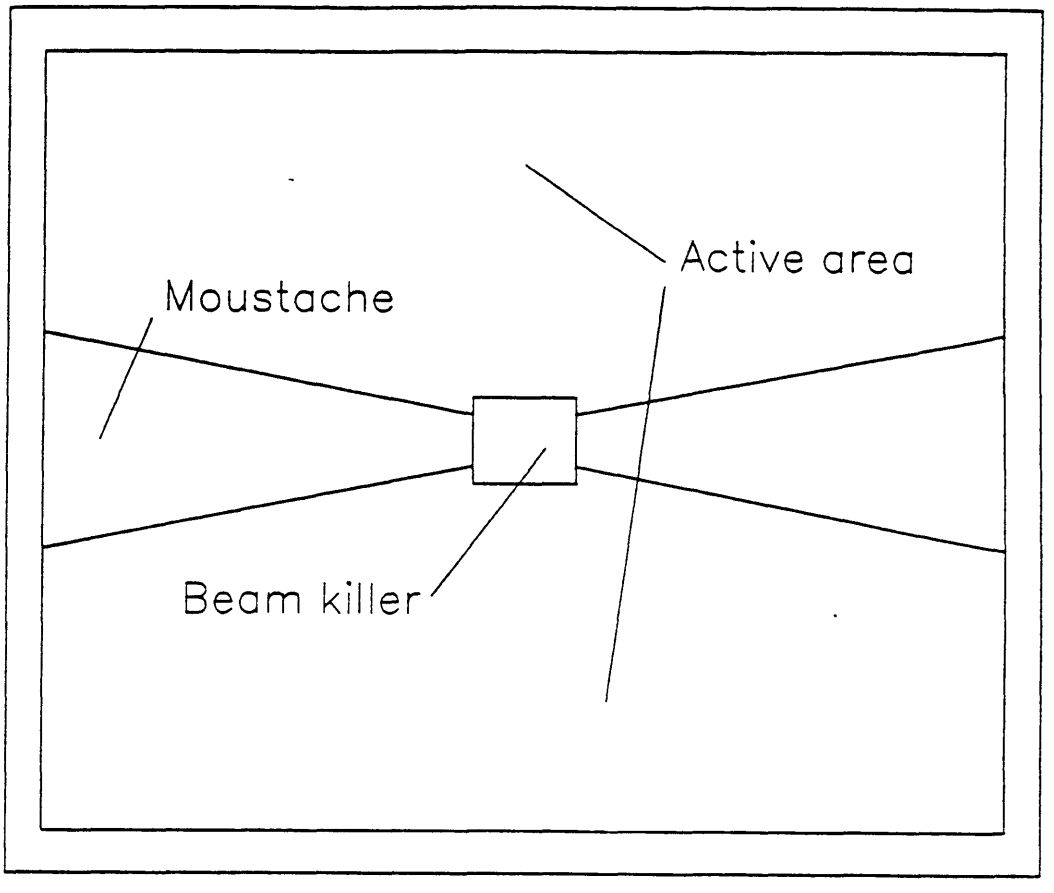


Figure 14: The geometry of the beam-killers and moustaches. The moustaches protect against the large number of e^+e^- pairs which are present in the horizontal plane.

G1: G1 lies before the CROWN calorimeter in Stack 1 and is used to increase the fraction of pretriggers of hadronic origin (see section 2.6) and for timing (it is attached to TDC's). It consists of 80 vertical scintillators, presenting an area of 55 cm x 5.4 cm each, arranged in four planes of twenty, two planes above the beam and two below. The back plane is in each case displaced by 2.7 cm

relative to the front plane. A gap of ±2.5 cm vertically from the beam axis is uncovered because of the flux of e^+e^- pairs.

G2H: G2H consists of 32 elements, 120 cm x 7 cm, horizontally arranged downstream of Goliath. The elements overlap slightly and there is again a small gap at z = ±2.5 cm.

G2V: Positioned downstream of G2H, G2V comprises 24 vertical scintillators each measuring 75cm x 20cm. They are arranged in 2 arrays of 12, one above and one below the beam axis, separated by 6cm.

2.5.1 The muon filter

Muons are detected as those particles traversing an iron wall. The particles are detected by 3 hodoscopes: H1H, placed after 2m of iron and H3H,H3R,H3V at a depth of 5m.

2.6 The Pretrigger (PT1)

All NA-14 triggers are taken in coincidence with a pretrigger whose purpose is to ensure the presence of a photon interacting hadronically in the target. It also provides a timing signal for the experiment (this comes from the tagging apparatus and thus has a resolution of about 1 ns).

A pretrigger consists of demanding:

- A downstream electron of < 80 GeV/c as indicated by the BTC. Given the upstream electron spectrum this corresponds to there being a photon of > 60 GeV/c.
- There must be a signal of less than 2 mip in the charged veto which lies in front of the target. This provides protection against showers from electrons which strike the last of the collimators.
- ≥ 1 hit in the scintillator active target.

- One of the following conditions must be fulfilled:

1. At least one hit in the upper half of each of G1,G2H,G2V or in the lower half.

2. $\geq$ 2 hits in G1

In addition there must be no hit in the μ-veto (figure 7) in the same half (up or down) as the hodoscope hits. From a monte-carlo study it has been found that PT1 has essentially 100% acceptance for QED Compton events except when the photon is produced at high X_L In that case, the struck quark is moving backwards in the centre of mass and may not give the required hodoscope hits. This does not affect prompt photons in ILSA since it is at ~90° in the centre of mass.

Off-line it has been established that the pretrigger is about 10% hadronic.

2.7 The ILSA calorimeter

This thesis is concerned with the study of events recorded with a high p_t photon in ILSA. ILSA will therefore be described in some detail.

ILSA is a lead scintillator sandwich calorimeter placed 13.5m downstream of the experimental target. It consists of four quadrants positioned as shown in figure 11 and treated as separate entities throughout the analysis. The vertical distance between quadrants is 40cm which ensures that the large number of Bethe-Heitler pairs does not cause too many triggers.

2.7.1 An ILSA quadrant

The structure of an ILSA quadrant is shown in figure 15. It consists of 4 layers of calorimeter modules A,B,C,D. A layer consists of 4 modules each presenting a surface area of 25cm x 100cm to the oncoming particles. A module is made of alternating sheets of 5mm thick plexipop scintillator and 3 mm thick lead. The A and B modules contain 6 layers of lead+scintillator (3.5 X_0) and the C and D modules 9 layers (5.5 X_0). The A and C modules are horizontal and the B and D modules vertical. In front of each of the 16 crossings so formed is a charged veto counter 27 cm x 27 cm in extent. A 1 X_0 lead converter sheet sits between the vetos and the A modules to increase the level of conversion before the Ariadne position detector.

Ariadne consists of two crossed planes of 72, 1.5 cm wide scintillator fingers placed immediately after the first, A, layer of modules.

There are two additional orthogonal planes of scintillator, the S and T counters, which are used in the trigger but not in the analysis.

2.7.2 ILSA performance in a test beam

Prior to the start of NA-14 ILSA was extensively tested in test beams of hadrons and electrons at incident energies between 2 and 80 GeV. During the tests the lead sheet in front of the A modules was removed to compensate for the fact that electrons begin showering earlier than photons.

1. The relationship between GeV and minimum ionising particles was determined and has been used since for calibration.

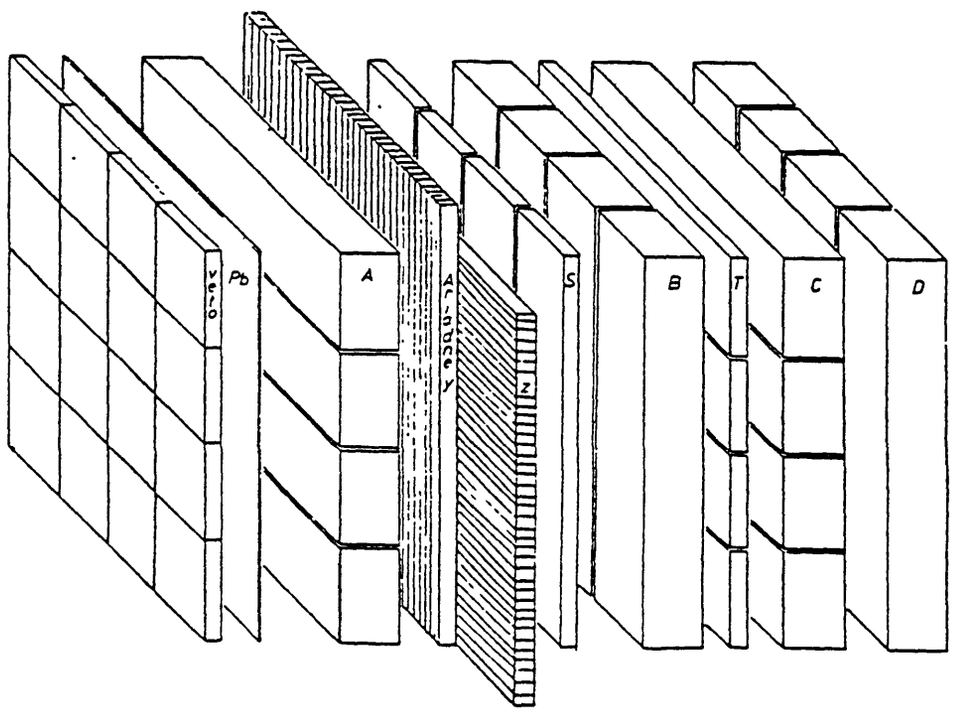


Figure 15: An ILSA quadrant. A,B,C,D are the calorimeter modules. Also shown are the charged vetos, the Ariadne planes and the S and T counters.

2. The energy resolution was measured and up to incident energies of 40 Gev the following relation for the full width at half maximum (FWHM) was found to hold

$$\frac{\sigma(\text{FWHM})}{E} = 1\% + \frac{35\%}{\sqrt{E}} \qquad (2.1)$$

3. The calorimeter response was found to be linear up to energies of 80 Gev (figure 16).

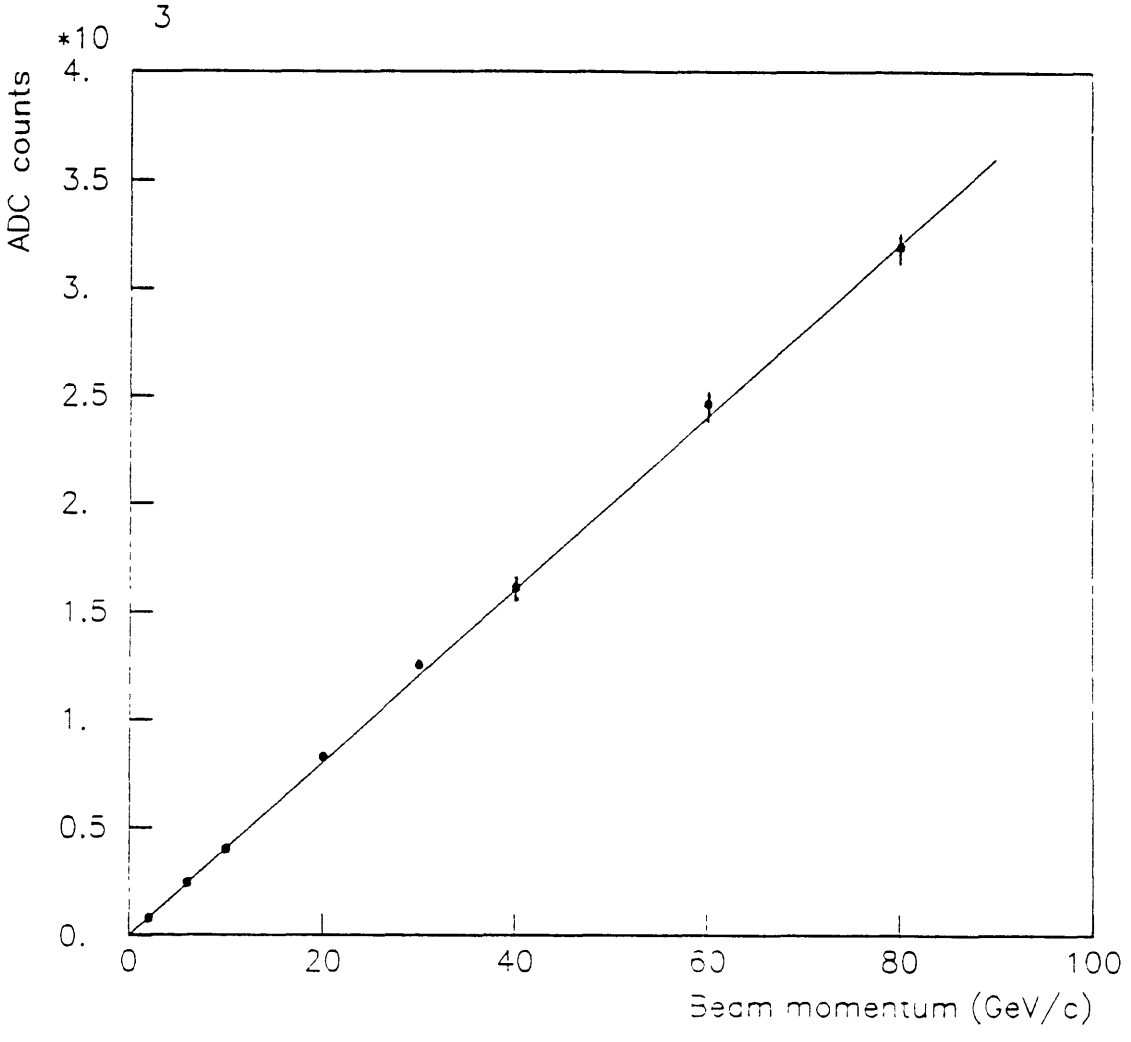


Figure 16: ILSA response as a function of energy in electron test beam.

4. The position resolution of Ariadne was found to vary from 2 mm when the shower is centred on the middle of a finger to 4 mm when centred on the divide between 2 fingers.

5. It is important to have good rejection against hadrons (neutral hadrons can only be rejected by the calorimeter itself). Figure 17 shows plots of energy deposited in A+C against energy deposited in B+D for both incident hadrons and electrons.

   The electromagnetic showers develop in such a way as to deposit half of their energy in the A and C modules and half in the B and D modules. Hadronic showers, on the other hand, behave erratically and can be rejected on this basis.

6. Light attenuation in the Ariadne fingers was measured as a function of distance x from the photomultipliers and found to vary according to the function

$$S(x) = S_0 \exp(ax + bx^2) \qquad (2.2)$$

   For the Ariadne fingers a and b were determined in the test beam to have values of $-0.835\ m^{-1}$ and $0.239\ m^{-2}$ respectively. These values are applied globally to all 576 Ariadne strips and correspond to an attenuation of 45% over the full 1 metre. The treatment of attenuation in the calorimeter modules is described below.

2.7.3 Calibration

ILSA was calibrated using relativistic μ's at the start of each data taking period. A simple S.T coincidence defined the crossing through which the μ had passed and a number of triggers thus obtained were written to tape for each crossing.

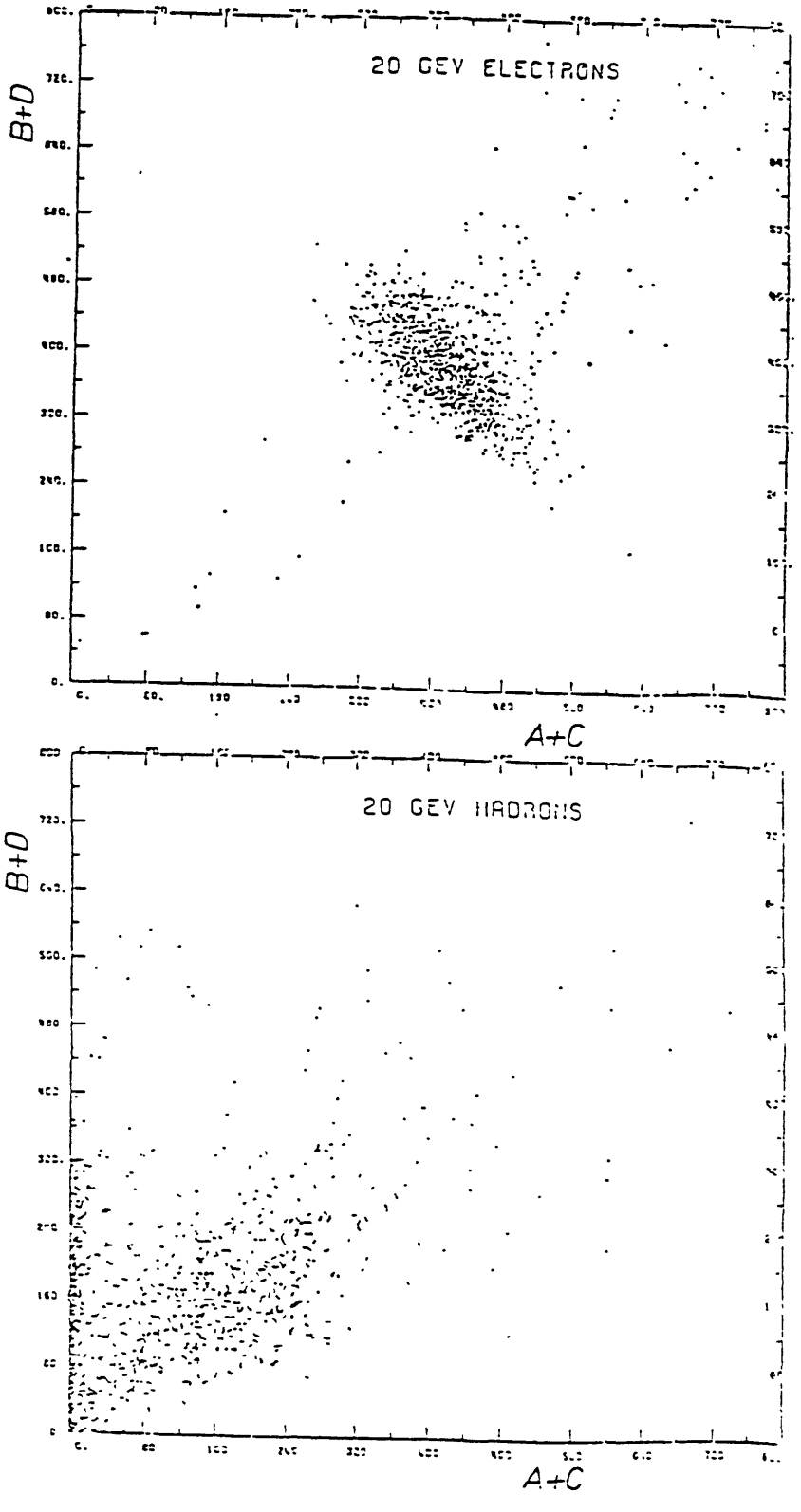


Figure 17: Response of ILSA to electrons and hadrons. The quantity E_a+E_c is plotted versus E_b+E_d.

From this data can be extracted the relationship between number of ADC counts and a single minimum ionising particle. The conversion factor to go from minimum ionising particles to Gev was determined in the test beam. The absolute calibration obtained in this way has quite a large error because in the test beam the photomultiplier gains were set so that a minimum ionising particle corresponded to only a few ADC counts. Therefore the calibration has to be tuned by observing the π^0 mass peak. It is then checked by looking for the η. (In fact the η is barely visible in ILSA for reasons of geometric acceptance.)

The level of attenuation in the calorimeter modules is measured at the same time as the calibration is done. It is in fact not a simple exponential but has a turnover about 18 cm from the photomultipliers due to the complex light reflection path. In practice, though, an exponential is assumed and the signal is given by

$$S(x) = S_0 \exp(ax) \qquad (2.3)$$

Typically $a \approx -0.4\ m^{-1}$ which corresponds to about 35% light attenuation over the full metre.

To make the trigger (section 2.7.4) effective the gains have to be well equalised. This was achieved at the start of each period by adjusting the photomultiplier HT's using relativistic μ's.

Ariadne and the veto counters were calibrated in the same way although in this case only relative calibration was necessary.

2.7.4 The ILSA high p_t trigger

ILSA triggers the experiment when there is a deposit of energy corresponding to a p_t of greater than a preset threshold. This was set at about 800-900 MeV/c and at this level the energy in the D modules is very small so they were not used at all in the trigger.

The signals from each pair of A,C modules are summed. The attenuation in the scintillator, together with the positioning of the calorimeter with respect to the beam axis, ensures that a photon of a given p_t produces roughly the same signal irrespective of the y coordinate of the impact. For the same to be true in the vertical direction it is necessary to attenuate the signals from the pairs of A+C counters relative to each other.

The B modules are not attenuated relative to one another since the difference in p_t of a photon of a given energy hitting the closest module to the beam and hitting the farthest away is much smaller than in the case of the A,C modules. Attenuation again helps to make the response flatter in p_t than would otherwise be the case.

The signals from the (A+C),B,S,T,V counters are sent to a discriminator whose thresholds can be set under software control. The discriminated signals are then sent to custom built, software controllable, CAMAC logic units where the following condition is demanded:

$$\sum_{i,j} T_i . (A_i + C_i) . S_j . B_j \qquad (2.4)$$

where the indices i and j run from 1 to 4 for a quadrant, the "+" represents a linear sum and the "Σ" represents a logical sum (an OR function).

- Chapter 3 -

THE INCLUSIVE ANALYSIS

3.1 Introduction

The object of the inclusive analysis is first to demonstrate the existence of a prompt photon signal and then to compare its magnitude with theoretical predictions. This is done by comparing the p_t spectra of γ's and π^0's produced in the γ beam with those produced using incident pions. The analysis is identical for each data set and is described in this chapter. Much of the detail of the pattern recognition in Ariadne and of the analysis in general have been described elsewhere[36] and here only a brief description will be given with emphasis on new developments.

3.2 General facts

A number of facts about ILSA and particles therein should be borne in mind when considering the following analysis.

Geometry: Taking into account the fiducial volume of ILSA (section 3.6) and considering the nearest and farthest points from the beam axis it can be seen that ILSA covers radial distances R from the axis between

$$110 \text{ cm} < R < 226 \text{ cm} \qquad (3.1)$$

The fact that the Ariadne position detector is 1355 cm from the target yields the fact that

$$6.0 < E/p_t < 12.3 \qquad (3.2)$$

π^0 separation: For the decay $\pi^0 \rightarrow \gamma\gamma$ the lab. angle θ between the 2 γ's is given by

$$m^2 = 2E_1E_2(1-\cos\theta) \qquad (3.3)$$

Bearing in mind again that Ariadne is at 1355 cm the separation of a π^0 at the Ariadne plane is given by:

$$d_{exp} = 183 / \sqrt{(E_1E_2)} \qquad (3.4)$$

Hence for a 20 Gev π^0 the $\gamma\gamma$ separation for a symmetric decay is 18.3 cm. For ILSA therefore the technique adopted to identify π^0's is to combine spatially well separated γ's rather than trying to split up merged showers.

Energy-p_t correlation: From the iso-p_l and iso-p_t lines on figure 12 it can be seen that p_l and p_t are closely related in ILSA. This fact is used frequently in the analysis.

Parent-child effect: The π^0 cross-section is a steeply falling function of p_t ($\sim 1/p_t^8$). A single photon in ILSA coming from π^0 decay will therefore in general be the product of a π^0 of only slightly higher p_t than the detected photon. This is because an asymmetric decay of a π^0 of slightly higher p_t is far more likely than a symmetric decay of one of the (far fewer) π^0's of much higher p_t. This also results in the VDM contribution to the single photon p_t spectrum having very much the same shape as the π^0 spectrum.

3.3 Data sample

The γ beam data was recorded during two SPS periods in 1982 and three in 1983. In fact, because of the poor performance of the SPS in 1983 and the fact that a considerable length of time was given over to π^- running, the bulk of the data was taken in 1982. In total

the experiment wrote to tape about 8.5 10^6 events of which approximately one quarter were ILSA triggers, recorded with a hardware threshold corresponding to a $p_t > 900$ MeV/c.

In each of the periods of 1983, some of the time was devoted to data-taking with a π^- incident beam. Three different energies (70 Gev, 90 Gev, 120 Gev) were used in order to simulate the photon beam spectrum. In addition, the hardware threshold was, for part of the time, increased to $p_t > 1400$ MeV/c to improve the population of the high p_t end of the inclusive p_t spectrum.

3.4 The VDM Monte-carlo

This was used extensively to guide the inclusive analysis. It has been described in considerable detail elsewhere[36,37] but a brief description is nevertheless warranted here.

The cross-section for $\gamma N \rightarrow \pi^0 X$ is assumed to be the same as that for $\pi^- N \rightarrow \pi^0 X$ multiplied by the ratio of the total inelastic cross-sections for photoproduction and pioproduction. The $\pi^{\pm} p \rightarrow \pi^0 X$ cross-section at 100 Gev/c incident energy has been parametrised[8] as

$$E\frac{d^3\sigma}{dp^3} = \frac{A[1-\sqrt{((x_t^2 + (x_l - x_0)^2)}]^f}{(p_t^2 + m^2)^n} \qquad (3.5)$$

where x_l and x_t are the transverse and longitudinal Feynman x variables already defined and

where $f = 3.21$, $x_0 = 0.14$, $n = 5.03$, $m^2 = .96$ $(Gev/c^2)^2$. As will be seen later, this formula when normalized as above describes π^0's detected in ILSA very well. Equation 3.5 refers to the cross-section on a H_2 target and to extrapolate to ^6Li a simple A^n law was used with $n = 1$.[38]

π^0's are generated according to the above cross-section and allowed to decay to two photons. The γ's are tracked through the apparatus, allowing for the possibility of conversion, until one or both or neither of them hits ILSA. The incident particles then cause showers which are created using the EGS[4] monte-carlo program.[39] The measured response of the calorimeter is then used to convert the deposited energy into ADC counts which are then written to tape to be analysed in the same way as the real data. In this way a good simulation is obtained of the kinds of events caused in ILSA by genuine photons: no account is taken of muons, for example, so the TDC and μ-veto cuts cannot be applied.

η,η',ω,ρ production are also taken into account using the same form for the cross-section and ratios $\eta:\pi^0$ etc as measured in hadroproduction. The $\eta:\pi^0$ ratio used is 0.5 and this has since been confirmed by NA-14 for η's detected in OLGA.[5]

3.4.1 QED Compton Simulation

QED Compton photons generated using the program of Aurenche et al[25] were treated in the same way as the VDM monte-carlo data. This means that when it comes to comparison with experimental results both sets of 'theoretical' predictions have been treated in the same way.

---

[4] EGS is a monte-carlo program which generates electromagnetic showers by tracking individual particles through a detector.

[5] The value obtained in NA-14 is .46±.08.

3.5 Pattern recognition and photon reconstruction

Because of the poor spatial resolution of the calorimeter modules the ILSA pattern recognition begins with Ariadne. A cluster in projection is defined as at least two consecutive Ariadne fingers having signals > 0.4 minI (σ_{noise} is less then 0.1 minI for most channels) and with a total of at least 3 minI. Clusters in the Y and Z projections are then associated, the largest with the largest etc., to form photons. Knowing the coordinates of the hit, attenuation in the scintillator is corrected for. If the signals in Y and Z are not brought closer to each other by this process (they should be the same since both planes are crossed by the same number of charged particles) a different cluster association is tried.

Each quadrant is given a label (m,n) according to the number of clusters m and n found in Y and Z respectively.

In the case of (2,1)'s (and (1,2)'s) the projection containing 2 clusters is examined more closely. If the separation of the two clusters is consistent with a π^0 of the measured energy, two γ's are formed and the quadrant retains its (2,1) label.

If the above condition is not satisfied and the two clusters are separated by no more than 2 empty (<.4 minI) strips then one gamma is formed and the label is changed to (1,1). In this case the separate cluster was probably caused by, for example, a large angle bremsstrahlung early in the showering process.

The following energy cuts are then applied to the photons:

$$\begin{aligned} E_a + E_c &> 0.5 \text{ Gev} \\ E_b + E_d &> 0.5 \text{ Gev} \\ E_{tot} &> 1.5 \text{ Gev} \end{aligned} \qquad (3.6)$$

where E_a is the energy in the A module etc.

3.6 The Analysis

Events containing a photon of $p_t > 1$ GeV passing the following list of criteria are filtered off for further analysis.

1. The photon should lie within a fiducial volume defined by a line 5 cms from the exterior edges of the quadrant.

2. The hit should be 'neutral' in that the veto counter positioned directly in front of the hit should contain a below-threshold signal. It is possible for electrons, having received a 1 GeV/c p_t 'kick' in the magnetic field of Goliath, to pass through one veto and hit the calorimeter in a position covered by a different counter. In order to reject these events an 'extended' veto requirement was introduced. If a hit in the calorimeter is within 7 cms of the beamside edge of a vertical module and the next-door veto on the beamside has fired the hit is rejected.

3. The trigger should be in time. The gate of the ILSA calorimeter module ADC's is ≈140ns and μ's from the halo can interact in this time. The time between the arrival of a pretrigger and the occurrence of a trigger condition is recorded by a TDC. Off-line a cut is made at ±12ns about the peak of the distribution, thus reducing the random μ background by a factor of ≈12.

4. The event should have a good vertex.

5. No charged track should be pointing to the calorimeter hit (within 5 cms). As previously stated, Ariadne measures

position to an accuracy of better than 5mm so this is a severe cut.

The first photon in an event satisfying the above is referred to as the 'trigger' photon. At this point the data is divided into two streams, γ's and π^0's the further analysis of which is discussed below.

3.7 π^0 Analysis

As mentioned previously the thrust of this analysis is to obtain samples of single photons and π^0's which are as pure and uncontaminated as possible. In keeping with this policy, π^0's are only reconstructed in events where only two photons appear in the quadrant containing the trigger. No additional cuts are applied to the 'other' (i.e. non 'trigger') photon. The $\gamma\gamma$ effective mass plots for (2,1)'s and (2,2)'s are shown in figure 18. Two γ combinations which have an effective mass between 100 MeV/c^2 and 170 MeV/c^2 are defined to be π^0's.

3.8 Single photon analysis

Again in keeping with the general philosophy of the analysis, only those events where the trigger lies in a (1,1) quadrant are considered as single photon candidates. A number of additional cuts are applied at this stage.

3.8.1 μ rejection

An event is rejected if there is a hit in the μ hodoscopes within 20cms of the trigger (in projection). This is a severe cut and there is a certain amount of random rejection of good events. One can get

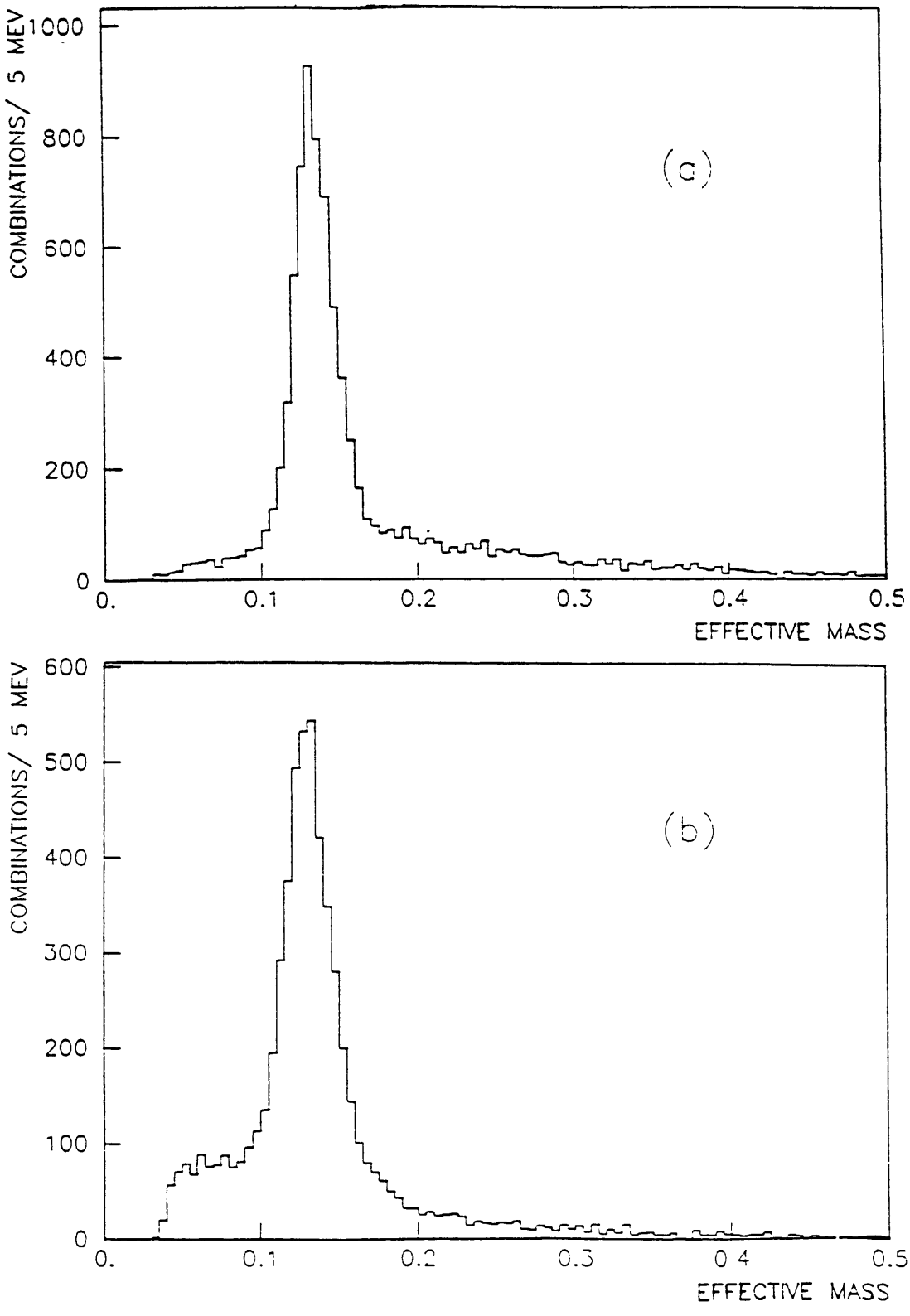


Figure 18: ILSA γγ Mass plots.
(a) In (2,2) quadrants.
(b) In (2,1) quadrants

a handle on this, however, by looking at the π^0 sample. The chance of a shower which reconstructs with another to give a π^0 mass having been caused by a μ interaction is very small. Hence by looking at the rate at which π^0 events would be rejected by this cut, one can calculate a factor to correct the photon data for the random rejection.

$$N_\gamma = \frac{n^0 - n^0_\mu}{1-C} \qquad (3.7)$$

where N_γ is the corrected value
n^0 is the raw value
n^0_μ is the muon subtraction
C is the random vetoing probability

The random vetoing probability C is found to be about 9.6%.

3.8.2 Shower Development Cuts

ILSA takes four samplings of each shower. The longitudinal development of showers can therefore be examined and is used to provide rejection against neutral hadrons as well as against any μ's or charged hadrons that have survived previous cuts. Showers reconstructing to form π^0's are unlikely to be due to anything other than genuine photons and are used to define what the profile of a good electromagnetic shower should be. The cuts imposed do not reject any π^0 candidates.

3.8.3 Merged π^0 rejection

An important source of contamination at high energy (and hence high p_t) is that due to π^0's the γ's from which are merged in both projections. An attempt is made to remove these from the data by examining the shower shape in Ariadne. The algorithm used proceeds as follows:

1. Search for 'the most significant dip' in the Ariadne profile. The method is illustrated in figure 19. On a plot of Ariadne pulse height against finger number the values are considered to be nodes connected by links. First, any upward fluctuations at the edges of showers are removed. Then the shortest link is located and the nodes joined by it are eliminated. The process continues until there remain only three turning points, the shape consisting of two peaks and a trough.

2. The cluster is split, at the trough, into two sub-clusters and the two projections are matched, largest sub-clusters together, to form two sub-showers separated by a distance d_{meas}. The energy of the shower is then divided according to the pulse heights in the sub-showers.

3. The expected separation d_{exp} at the ILSA plane of γ's from a π^0 symmetric decay is calculated according to equation 3.4 and a quantity P is defined as a measure of how 'π^0-like' the shower is.

$$P = \frac{d_{meas}}{d_{exp}} \qquad (3.8)$$

Figure 20 shows the P distribution obtained for the data of one period above a p_t of 2.2 Gev/c. along with that obtained using the VDM monte-carlo.

A clear accumulation can be seen around P = 1. In the inclusive analysis it is important not to remove any genuine single photons because in doing so comparison with theory would become more

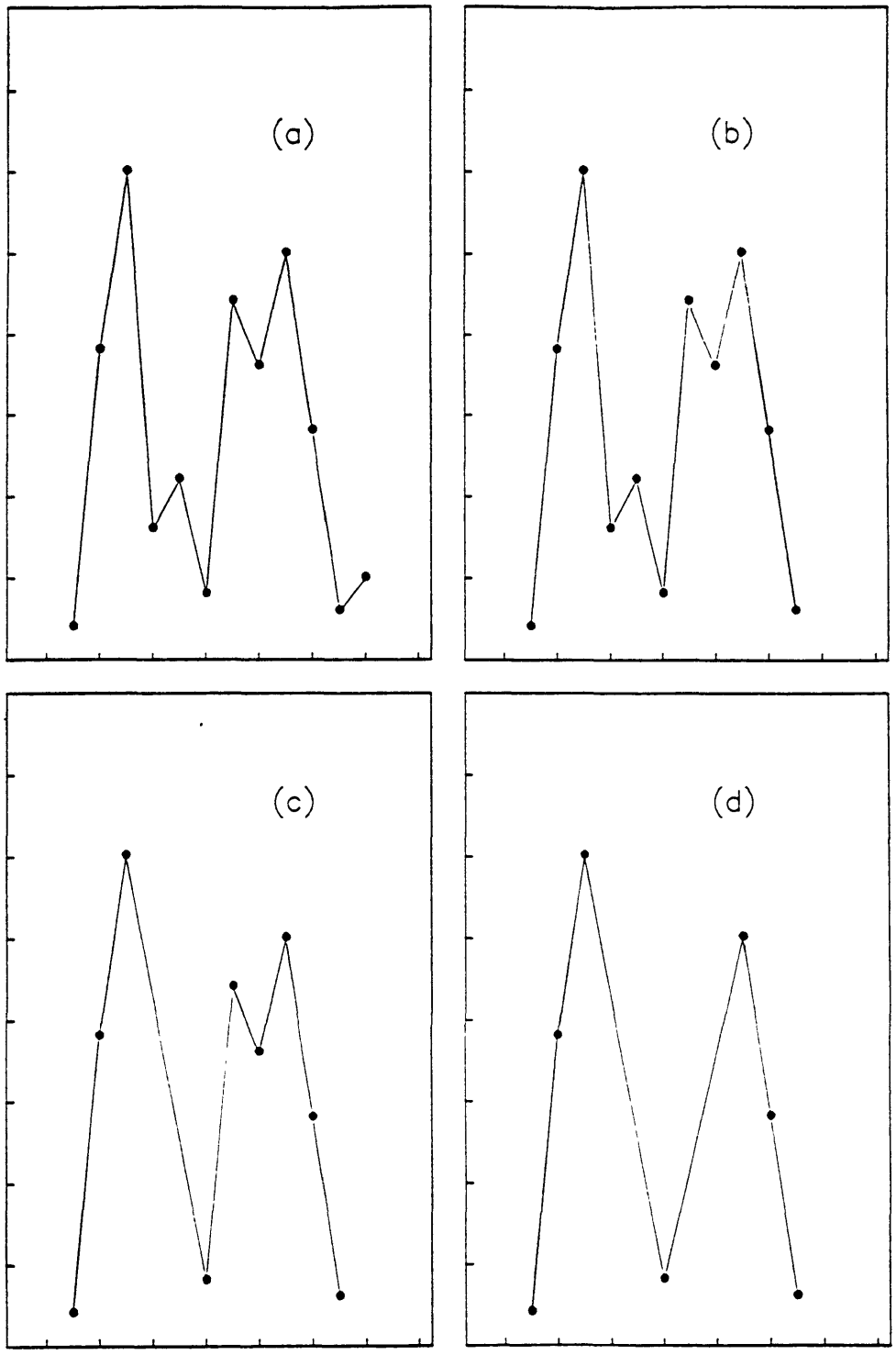


Figure 19: The CUTUP algorithm - finding the most significant dip. (a) Shows the Ariadne pulse height versus strip number. First, spurious upturns at the edge of the shower are eliminated (b). Then the shortest link is removed together with the nodes it connects (c) and the process is iterated until there remain 3 turning points only (d).

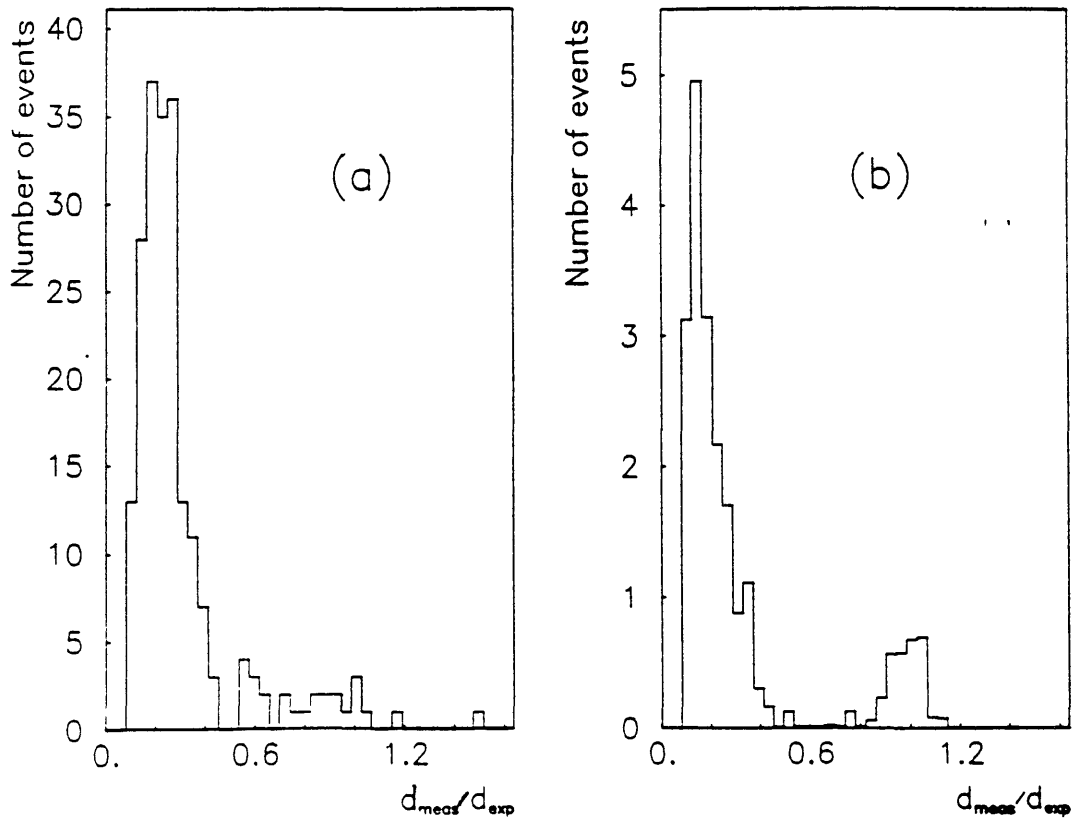


Figure 20: Distribution of $P = d_{meas}/d_{exp}$ in (a) data and (b) monte-carlo.

difficult and much less precise. Consequently events with $P > .7$ were rejected the choice being made on the basis of the figure 20b.

3.9 Normalization - methods used.

In order to compare the magnitude of any observed phenomenon with theoretical predictions, an absolute normalization is needed. Three methods of calculating the sensitivity have been used:

- counting the number of hadronic events. If the acceptance of the counting method is known, along with the beam spectrum, knowledge of the total inelastic cross-section leads to a value for the sensitivity.

- counting the number of electrons in the tagging system. Knowing the total radiator thickness, one can again calculate how many events per nanobarn have been recorded.
- Bethe-Heitler μ pairs. The cross-section for this process is well known and NA-14 has a very good μ capability.

I will here describe the first of these methods. The results obtained using the other techniques agree well, within errors, with that given below.

3.10 Normalization - counting hadronic events.

The number of hadronic events is counted using the so-called double arm pre-trigger (DARM). This demands that, in addition to the normal pre-trigger requirement (PT1), at least one charged track passes through each of the upper and lower halves of the experiment. A track is here defined by hits in each of G1,G2H,G2V. During each SPS spill a few events of this type are written to tape and at the end of the burst the total number of DARMs is also recorded.

This information can then be used to calculate the sensitivity via the formula

$$S = \frac{\Sigma DARM.p}{\sigma_{eff}(Li)} \cdot \frac{1}{\int a(E_b) n_b dE_b} \qquad (3.9)$$

where ΣDARM is the total number of DARM recorded, p is the probability that a DARM event is hadronic with a good vertex, $\sigma_{eff}(Li)$ is the effective hadronic cross-section on ^6Li target and $\int a(E_b) n_b dE_b$ is the acceptance of DARM to hadronic events integrated over the beam spectrum. The various factors are evaluated below.

3.10.1 Pion beam

p: DARM events are fully reconstructed offline and event displays are studied to determine if the events are hadronic with a good vertex. The value obtained is p=0.91±.05.

$a(E_b)$: This is evaluated in two ways. The standard pre-trigger has approximately 100% acceptance for hadronic events and, for incident π^- beam, the events recorded are essentially 100% hadronic. Hence a simple ratio of the number of DARMs to the number of PT1's gives the DARM acceptance to hadronic events. A simple monte-carlo is also used and the results from the two methods are compared in table 2.

Table 2: Comparison of two ways of evaluating DARM hadronic acceptance.

E(Gev/c)	$a(E_b)_{measured}$	$a(E_b)_{mc}$
30		15.5
50		29.0
70	40.5	40.0
90	47.0	
100		46.0
120	53.3	55.0

$\sigma_{eff}(Li)$: This is calculated using the formula

$$\sigma_{eff} = [\sigma_{inel} - \sigma^{0,2\ prongs}(\pi P)]\ \frac{\sigma_{inel}(\pi Li)}{\sigma_{inel}(\pi P)} \qquad (3.10)$$

$\sigma_{inel}(\pi^- p)$ is given in tabulations[40] and has a value of 20.5mb. The acceptance of DARM for 2 prong events is difficult to estimate.

The cross-section for such events is 2-3mb at the relevant energies and if one assumes that the acceptance for these events is 50% of that for ≥ 3 prongs then the bracketed factor in equation (3.10) is about 19±2mb.

The inelastic cross-section for pions of 60 Gev incident on ^{7}Li,C,Al,Cu,Sn and Pb has been measured[41] and can be parametrised as

$$\sigma(A) = 25.75\ A^{0.76} \qquad (3.11)$$

Assuming this relation to be valid for ^{6}Li we arrive at a value for σ_{eff}(Li) of 15.6±1.6mb/nucleon.

$n_b dE_b$: At each beam energy $n_b dE_b$ is taken to be unity for the pion beam.

3.10.2 γ beam

p: For the γ beam this turns out to be .75±.1

$a(E_b)$: is assumed to be the same as for the pion beam. It cannot be evaluated directly in the same way as is the π^- result because of the greater level of background giving a PT1.

σ_{eff}(Li): In the case of a photon beam this is calculated via the expression

$$\sigma_{eff} = [\sigma_{tot}(\gamma p) - \sigma_{el}(\gamma p)].N \qquad (3.12)$$

The nuclear dependence N is obtained by extrapolating the data of Caldwell et al[42] down to A=6. N is then equal to 0.94. The total photoproduction cross-section at high energy is 115μb[43] and the cross-sections for ρ,ω,φ are respectively[44,45] 9.4μb, 1.2μb, ~0.6μb. σ_{eff}(Li) is then 94±6μb for the photon beam.

$n_b dE_b$: The photon spectrum of figure 10b is used.

Inserting the above numbers into the equation 3.9 yields the following answers for sensitivity per 10^6 DARMS.

$$S_{\pi^-}{}^{70} = 145.8 \text{ evts/}\mu\text{b}$$
$$S_{\pi^-}{}^{90} = 124.1 \text{ evts/}\mu\text{b}$$
$$S_{\pi^-}{}^{120} = 110.1 \text{ evts/}\mu\text{b}$$
$$S_\gamma = 20 \text{ evts/nb} \qquad (3.13)$$

where the errors are estimated to be about 20%.

These result in the absolute sensitivities shown in table 3.

Table 3: Sensitivities (evts/nb) as calculated by the DARM method.

1) π^- beam

E_{beam}(Gev)	-------Threshold------- 900 MeV/c	1400 MeV/c
70	.87	6.1
90	1.56	10.25
120	.63	4.4

2) γ beam: 2460 evts/nb

- Chapter 4 -

THE INCLUSIVE RESULTS

The twin aims of the inclusive analysis are to see if there is a detectable direct photon signal and, having established this, to compare its magnitude to that expected from theory. The first of these is done by direct comparison with the results obtained in a π^- beam. This chapter begins with a discussion of possible objections to this procedure. Next, the pion spectra are constructed from the three different incident energies and two trigger thresholds. Then the γ beam spectra are compared to the π^- beam spectra to reveal the existence of a prompt photon signal at high p_t and finally this signal is theoretically interpreted.

4.1 Objections to the use of π^- beam.

The use of a π^--γ comparison to demonstrate the existence of pointlike photon interactions is valid only if the π^- beam is a good measure of all the non-pointlike processes involved. A number of objections could be made to this statement and they are considered in turn below.

- The η/π^0 ratio may not be the same in the two beams.

  In fact this has been measured by NA-14 which finds that

$$\frac{(\eta:\pi^0)_\gamma}{(\eta:\pi^0)_\pi} = 1.05\pm0.3 \qquad (4.1)$$

- ρ,ω,ϕ production is considerably higher in a photon beam than in a pion beam. This is true only for elastic interactions. At high p_t the events are inelastic and the statement no longer holds.
- There may be a direct γ component in the π^- beam. Measurements have been made by a number of experiments[46] which find that the effect is small ($\gamma/\pi^0 \leq 10\%$ for 2 GeV $< p_t <$ 4 GeV). In any case, if prompt photon production by a pion beam is non-zero then so will be that of the vector meson part of the photon. The procedure used will then subtract this contribution leaving only those processes where the photon couples directly to the partons.
- The μ halo is not the same for each beam. This statement is true for the standard 'clean' pion beam (see section 2.2.4) with which the γ beam is compared. It would affect the results if the rejection power of the spectrometer against μ's were insufficient. As already stated, the μ's are rejected from the data sample by timing cuts, veto counters in front of the calorimeters, the μ filter and by recognising charged tracks in the chambers. After all these rejections are applied, the remaining high p_t photons are left-right and up-down symmetric in the experiment. The halo muons are, on the other hand, very asymmetric and it seems unlikely therefore that there remains any significant muon contamination. As an additional check, however, some special runs were made using a 'dirty' pion beam (section 2.2.4). In figure 21 the resulting single photon p_t spectrum is shown. The solid line is that obtained in the 'clean' pion beam. It is clear that there is no significant difference between the two curves.

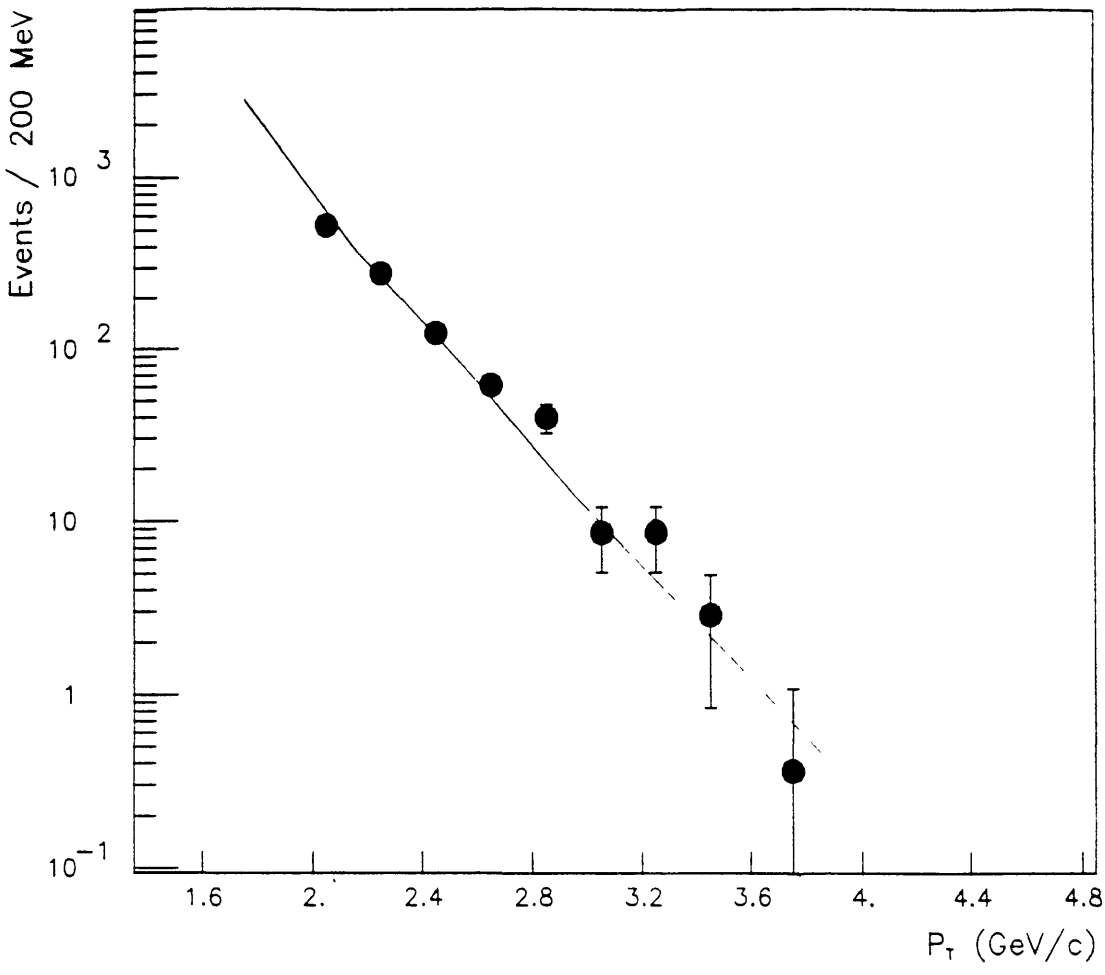


Figure 21: Comparison of 'clean' and 'dirty' π^- beams. The solid line is the 'clean' spectrum, the data points are the 'dirty' spectrum.

From the above it can be seen that the use of the π^- beam for comparison purposes is completely justified.

4.2 The π^- beam p_t plots.

The incident pion data at three different beam energies and two hardware thresholds have to be combined to produce a single p_t plot for the π^0's and a single plot for the γ's. This is done in the following way:

1. Simulate the γ beam spectrum of figure 10b. The data points of the three different beam energies at 1400 MeV/c threshold are added in the ratio 1:1:0.5 (70 GeV:90 GeV:120 GeV). The sensitivity of the plot so produced is, from table 3,

$$6.1 + 10.25 + 0.5 \times 4.4 = 18.5 \text{ events/nanobarn} \qquad (4.2)$$

In fact the 70 GeV data is given greater weight than one might expect from figure 10b in order to compensate for the lack of data at around 30-50 GeV incident energy.

2. Add the 900 MeV threshold data in the same ratio of sensitivities. This corresponds again to adding the data in the ratio 1:1:0.5.

3. Multiply the 900 MeV threshold data by the factor

$$\frac{\text{sensitivity of 1400 MeV/c threshold}}{\text{sensitivity of 900 MeV/c threshold}} = \frac{18.5}{2.75} \qquad (4.3)$$

and put the points on the same plot as the 1400 MeV data. This is shown in figure 22 for the case $\pi^- N \rightarrow \gamma X$.

4. It can be seen from figure 22 that at low p_t the 1400 Mev threshold data points lie below those of the 900 Mev threshold. This is because of the raggedness of the hardware threshold which affects the efficiency of the reconstruction up to much higher p_t's than the nominal threshold value. In the π^0 data the effect is much stronger since then it can affect the data points up to twice the threshold (because of the fact that there are two photons sharing the p_t of the π^0). The threshold affected points are rejected and for the other points one takes the weighted average of the two data sets.

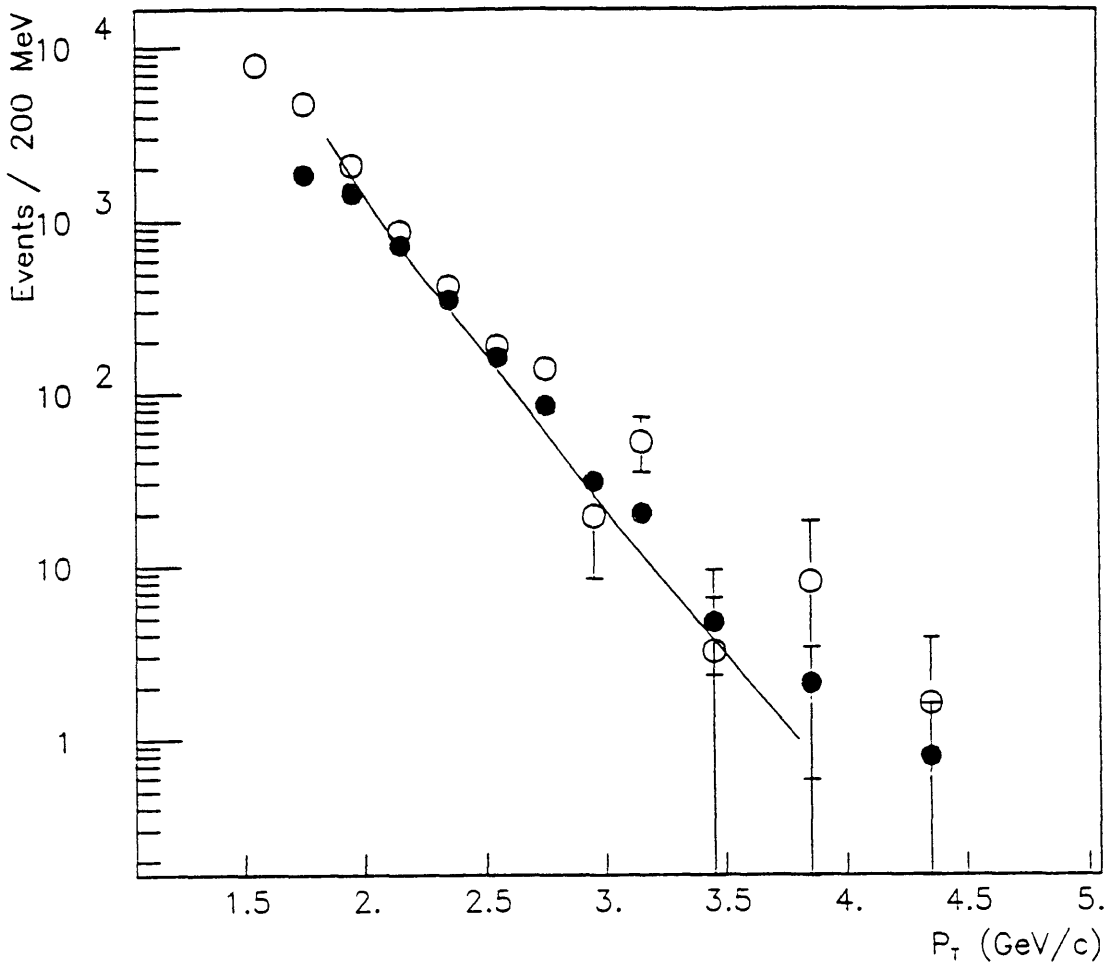


Figure 22: The construction of π^- beam plots. The 70,90,120 Gev beam data having been combined, the data taken with the 2 thresholds are placed on the same plot. The solid line is the final spectrum.

Exactly the same procedure is used for the π^0 data set.

4.3 Comparison of γ beam and π^- beam data

The p_t spectra of the γ's and π^0's produced by incident γ's and π^-'s are shown in figure 23.

The solid lines on the plots have been produced in the following manner.

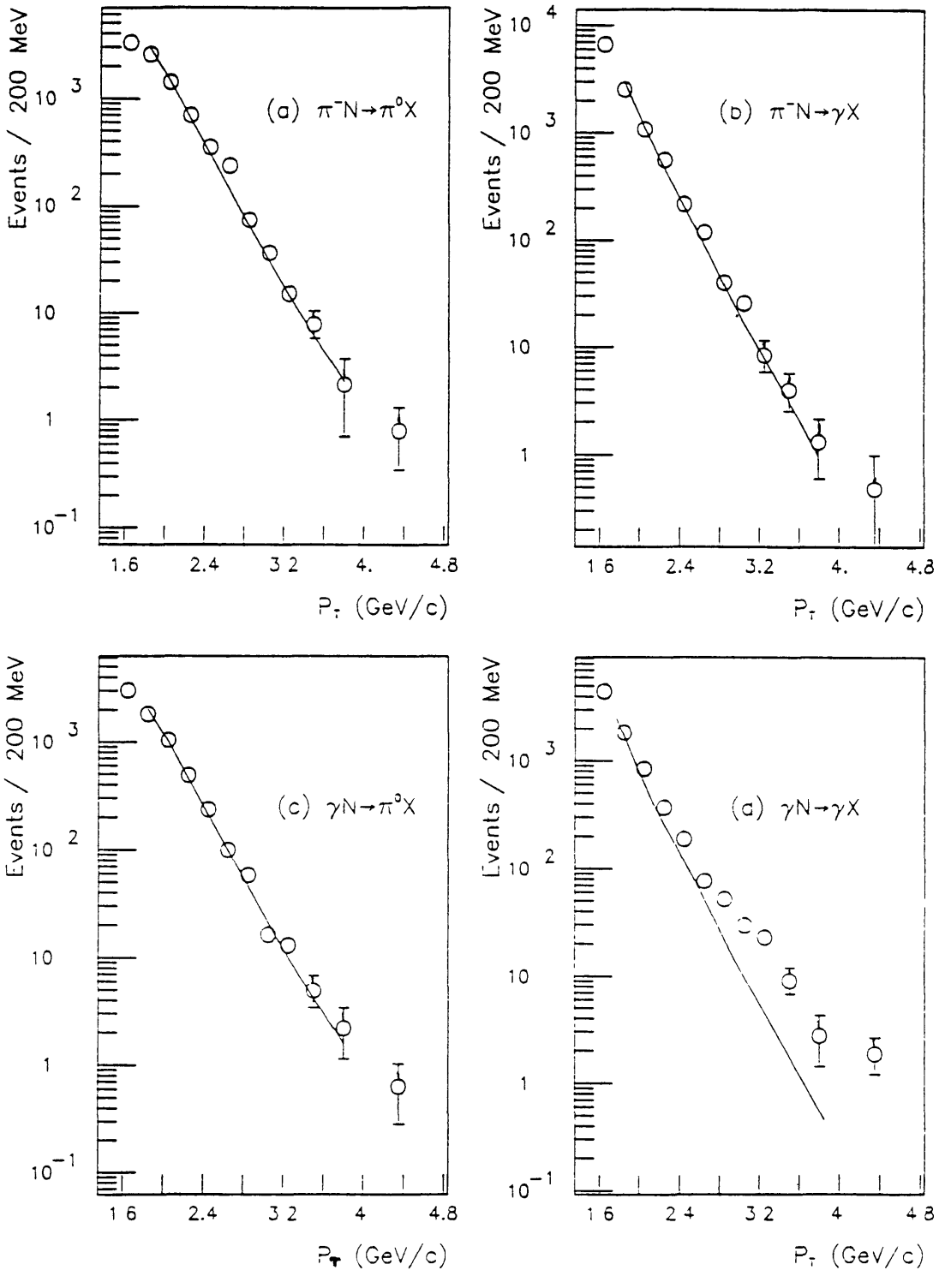


Figure 23: Comparison of π^- beam and γ beam p_t spectra. The data are shown together with (in cases a,b,c) the result of fitting the VDM monte-carlo slope to the data. The solid line on (d) is curve (c) x F.

1. Take the shape of the monte-carlo π^0 spectrum and fit it to the π^0 curve produced by incident π^-. Given the cross-section quoted by Donaldson et al[8] one obtains a value of 16.7 evts/nb[6] which agrees very well with that of 18.5±4.5 evts/nanobarn from the DARM normalization.

2. Take the shape of the VDM monte-carlo single γ spectrum and fit it to the $\pi^-N \rightarrow \gamma X$ data (figure 23b) It can be seen that here the data is also described well by the monte-carlo shape. This indicates that these photons are indeed produced as decay products of π^0's, η's, ω's etc. In fact, if one uses the monte-carlo to predict directly the magnitude of the single photon spectrum, one finds in the data an excess of about 20%. This can be accounted for if there is a γ/π^0 ratio of approximately 6% in the π^- beam at 2 GeV/c $< p_t <$ 4 GeV/c.

3. Fit the $\gamma N \rightarrow \pi^0 X$ data with the monte-carlo π^0 shape once more (figure 23c). The data are well described by the curve. The sensitivity obtained from this fit is 2390 evts/nb which agrees very well with that from the DARM method (2460 evts/nb)

4. Calculate the factor

$$F = \frac{N(\pi^-N \rightarrow \gamma X)}{N(\pi^-N \rightarrow \pi^0 X)} \qquad (4.4)$$

where $N(\pi^-N \rightarrow \gamma X)$ is the number of events on the γ plot
$N(\pi^-N \rightarrow \pi^0 X)$ is the number on the π^0 plot

---

6 In fact, this number should be increased by about 10% to allow for the vetoing effect of other particles in the event. The VDM monte-carlo does not allow for this.

If photons interact only as vector mesons the $\gamma N \rightarrow \gamma X$ data should be well described by

$$F \times N(\gamma N \rightarrow \pi^0 X) \qquad (4.5)$$

The curve (4.5) is shown along with the data points on figure 23d. The line fits the data well at low p_t but at high p_t there is a clear excess.

The absolute position of the background line on figure 23d can also be calculated from the line on figure 23d using the VDM monte-carlo. This gives a result which agrees very well with that shown.

4.4 Interpretation of the inclusive result

Figure 24 shows the $\gamma N \rightarrow \gamma X$ result once more, this time with the theoretical predictions for comparison. As can be seen, the data are well described by the indirect background line plus the DICS contribution as calculated by Aurenche et al.[25] Also shown is the sum of indirect background and the contribution expected from the Born diagram of the integer charged model discussed in section 1.3.1.

As can be seen, the data strongly favour the standard FCQ model of quark charge assignments even when higher order corrections have not been made to the ICQ predictions. One would expect those corrections to make worse the agreement between data and ICQ predictions.

In conclusion, the data agree well with the predictions of the standard FCQ model and rule out ICQ models which predict a level of DICS more than twice that of the FCQ model.

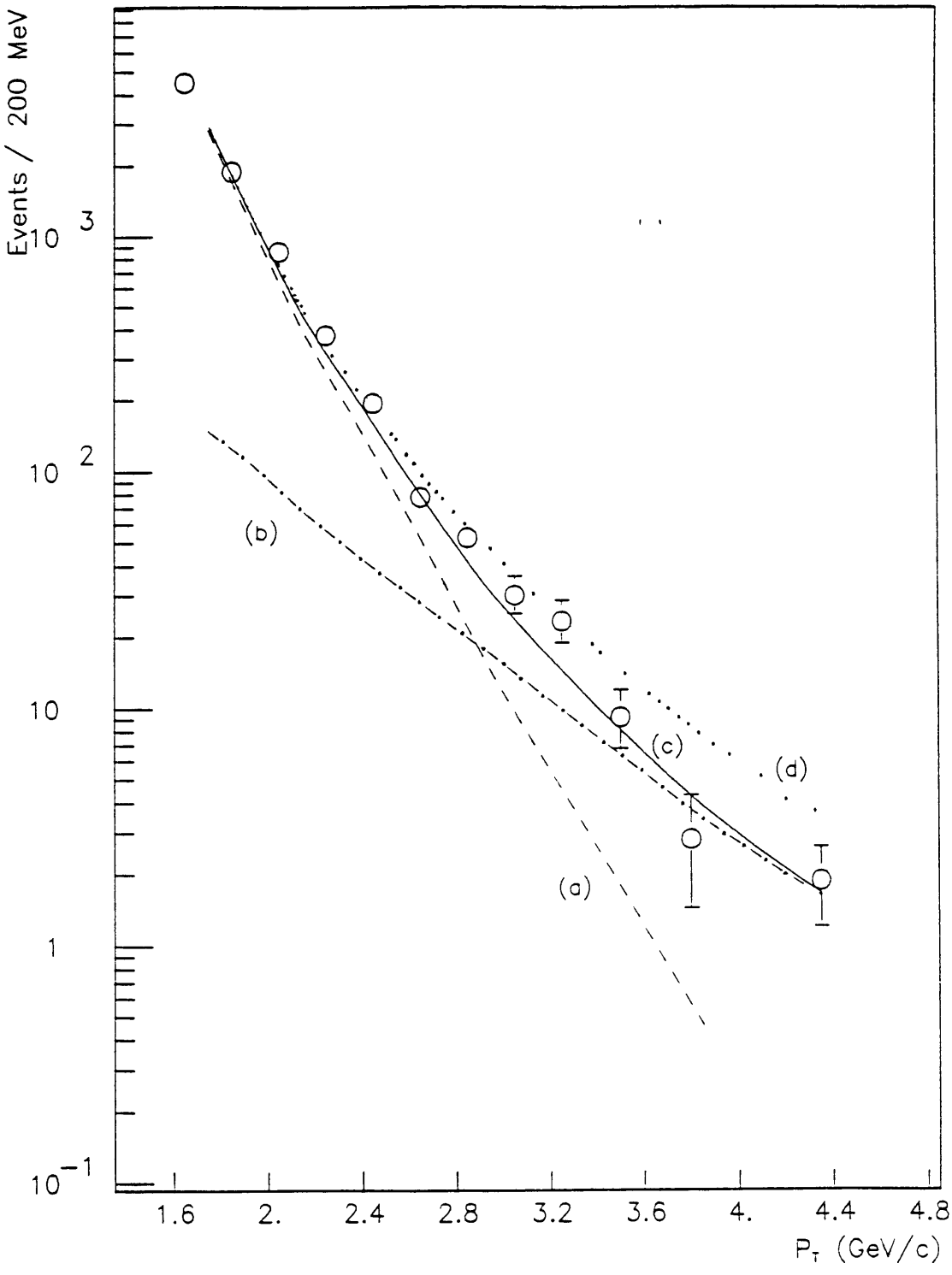


Figure 24: The comparison of $\gamma N \rightarrow \gamma X$ with theory.
(a) the indirect background line.
(b) FCQ Born plus h.o. corrections
(c) the sum of (a) and (b).
(d) the ICQ Born contribution plus background.

- Chapter 5 -

THE ENRICHMENT OF THE DATA.

As discussed in section 1.3.2, if the photons at high p_t are a consequence of simple Born level Compton Scattering, the full events should display some particular characteristics, namely: a specific topology and some level of +/- charge asymmetry in the quark jet. To study these effects one needs a reasonable signal/background ratio but as can be seen from figure 24 at a high enough p_t to achieve this there are insufficient events to do a meaningful analysis. Consequently some method of increasing the signal/background ratio had to be found in order to go to a lower p_t and thereby increase the size of the sample. The methods employed to do this are described in section 5.3

Having obtained a good sample of events, a method of comparing the results with theory is needed and for this a monte-carlo of QED Compton scattering is used. This chapter begins with a description of this monte-carlo.

5.1 The QED monte-carlo

Events were generated according to the lowest order QED Compton diagram (figure 1a). Corrections to this were not included in the program.

Very simple quark structure functions were used,[47] in which only valence quarks are considered, the sea quark and gluon

contributions being ignored. It has been found when using the scheme of Aurenche et al[25] that the cross-section varies only slightly with the choice of structure functions even in extreme cases.

The Lund fragmentation model[48] was used to produce the final state hadrons, the string being stretched between the struck quark and the spectator diquark. The beam was taken to have the energy spectrum shown in figure 10b and discussed in section 2.2.

After generation the events were passed through a program to simulate the performance of the detector, specifically that of the charged particle tracking. Two data sets were produced, one with the moustache areas of the chambers active and one with them inactive, the purpose being to understand the effect of the moustaches on acceptance (section 6.2.1). The performance of the calorimeters was not included in the simulation and instead each γ was labelled with the calorimeter it would hit (if any). At a later stage in the analysis the photon energies were smeared according to the known resolution of the calorimeters.

The tagging system was not simulated and this has consequences for the vertex reconstruction in the analysis. This is discussed in section 6.1.

After the event digitising stage the monte-carlo events were treated in exactly the same way as the real data. This is described in the next section.

5.2 Event Reconstruction

All events, real data and QED monte-carlo, were passed through the Trident track finding, track fitting and vertex package,[49] as

adapted for use on NA-14. Following this the data was processed by the calorimeter reconstruction programs and DST's[7] written. After tests the possibility of using the tagging information was rejected as the program was too time consuming and only a relatively small amount of information produced.

Finally the information was condensed and written to a mini-DST for efficient analysis.

5.3 Enrichments

The background to the QED Compton signal comprises decays of mesons like π^0 and η. The objective of the enrichment process is, therefore, to detect the presence of another photon which may be the partner of the trigger. An idea of where to look to find these γ's can be found by looking at the results of the ILSA VDM monte-carlo. Table 4 shows the fate of the 'other' (i.e. non-trigger) photon from a π^0 decay which gives a (1,1) trigger quadrant in ILSA. Only about 10%, those which do not convert and miss all the calorimeters, are hopelessly lost.

Since the $\eta:\pi^0$ ratio is ~.5 and the $\eta\rightarrow\gamma\gamma$ branching ratio is ~40% about 20% of the indirect background contamination is caused by η's. Where this is the case it is far more difficult to identify because, on the mass plots, the background under the η is much greater than is that under the π^0. In addition the greater mass of the η makes it more difficult to find electrons due to the conversion of the non-trigger γ.

---

[7] Data Summary Tapes

Table 4: Fate of the 'other' γ from π^0 decay in candidate γ events

'Other' indicates that the γ missed all calorimeters.
'Conversion' means that the γ converted before Goliath.
All figures are percentages, errors ranging from 10% – 20%.

Trigger p_t	OLGA	ILSA	CROWN	Other	Conversion
1.7	19.5	24.5	27.5	14	14.5
2.1	16	31.5	26.5	15	11.5
2.5	10.5	36.5	25	13	14
2.9	11.5	47	18.5	12	11
3.3	8.5	53	15.5	10	10

The next two sections deal with the finding of γ's in ILSA which have been missed by the analysis thus far, the following two with photons in the other calorimeters and with conversions respectively.

5.3.1 Merged π^0's

There may still remain some merged π^0's which have been missed by the cut described in section 3.8.3. There, the object was to remove as many contaminating π^0's as possible, whilst at the same time avoiding the removal of any genuine single photons from the sample. In contrast to this, the aim in this analysis, is simply to obtain as large a sample as possible of events rich in hard scattering content. The loss of one or two genuine prompt photons is not so important since no absolute measurement of cross section is involved. Events are therefore rejected with $P > .58$.

5.3.2 Recuperation of γ's missed in ILSA

The ILSA pattern recognition procedure was designed to produce a clean sample of good photons. In this process low energy photons

can easily fail the criteria of at least 3 minI in each Ariadne projection or the energy cuts of equation (3.6) and not be reconstructed. This is not important in the inclusive analysis since the same program is used for both γ beam and π^- beam (and for that matter for the analysis of the VDM monte-carlo data).

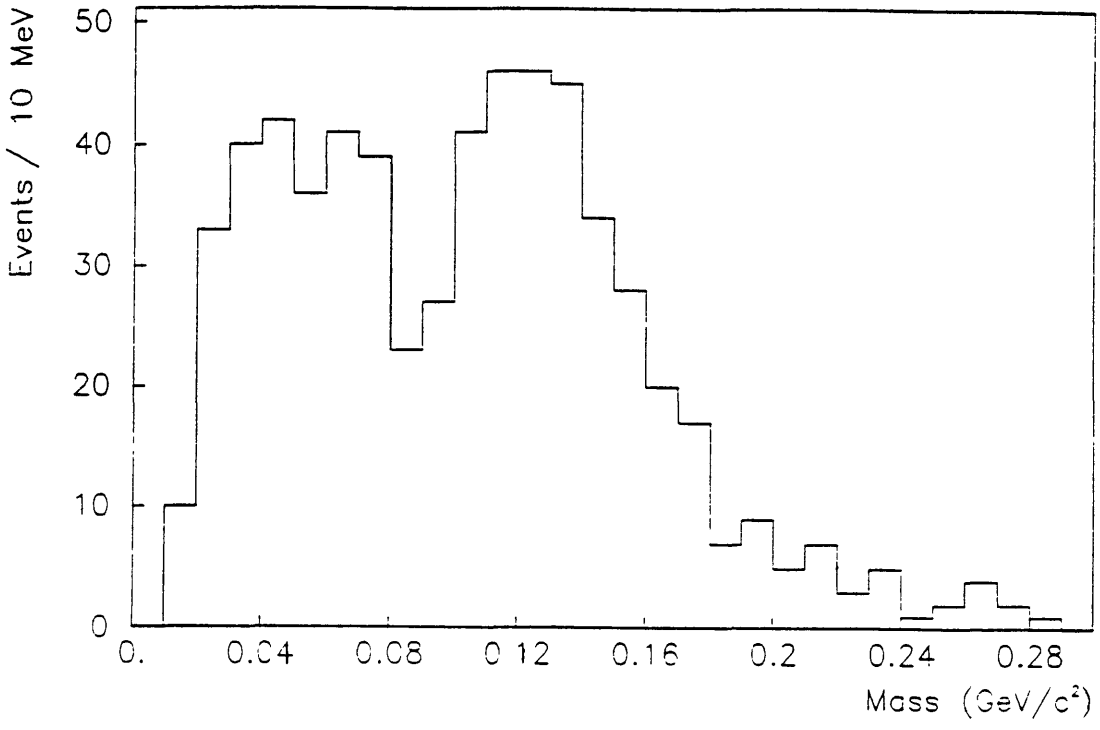
For the purposes of analysing non-inclusive features it is desirable to find and remove such events from the data sample. Instead of asking for 2 consecutive fingers to form a cluster, one demands only one finger and the Ariadne energy requirement is reduced from at least 3minI to > 1.5 minI. The energy cuts applied to 'photons' so formed are also relaxed to

$$\begin{aligned} E_a + E_c &> 0.2 \text{ GeV} \\ E_b + E_d &> 0.2 \text{ GeV} \\ E_{tot} &> 0.5 \text{ GeV} \end{aligned} \qquad (5.1)$$

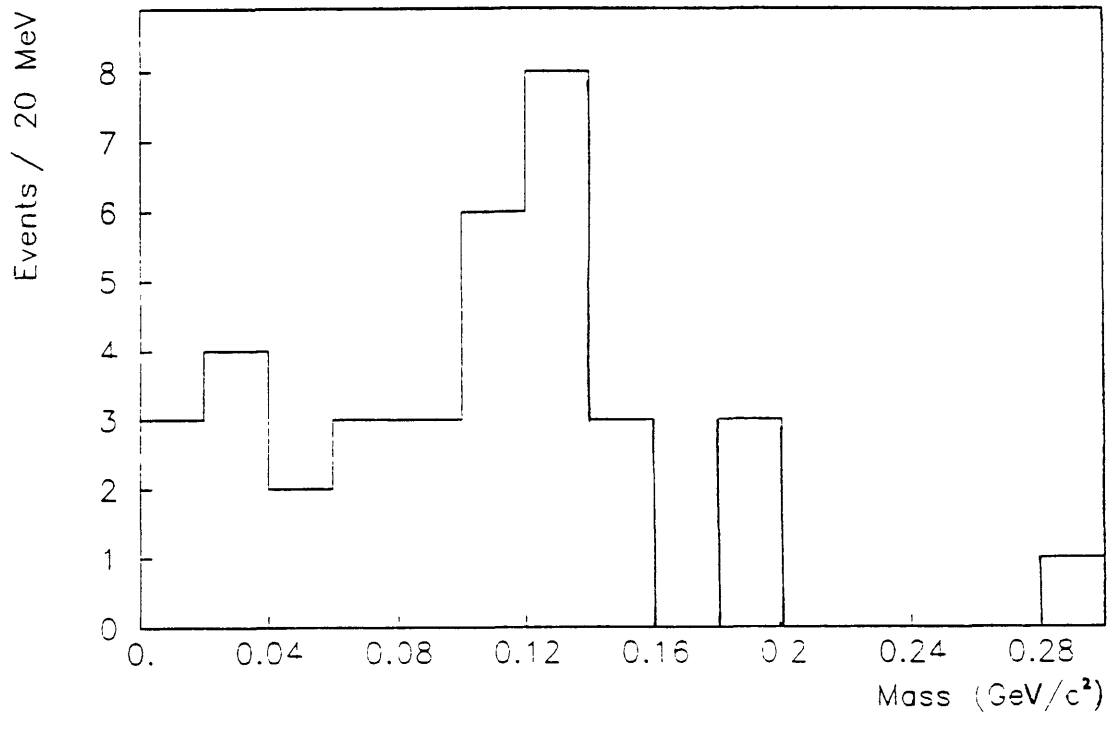
This results in the reconstruction of a considerable number of additional 'photons'. The $\gamma\gamma$ mass plot of the trigger quadrant with these cuts is shown in figure 25a.

There are two clear peaks: one at the π^0 mass and one at a much lower mass. The lower mass peak could be due to, for example, noise in ILSA. If this is the case, then events of all p_t's should have roughly equal probability of falling in that peak. (The 'hit map' of an ILSA quadrant is independent of p_t, the energy of any noise will be fairly constant, and the mass depends only on the square root of the trigger energy.)

Another possible source of background is hadrons. With the Ariadne requirement of > 1.5 minI it is possible that a charged hadron could reconstruct as a cluster and appear on the plot. Since fewer particles will accompany the trigger photon at high p_t (simple



(a) all trigger p_t > 1.5 GeV/c



(b) trigger p_t > 2.2 GeV/c

Figure 25: γγ mass plot in (1,1) quadrants with relaxed energy cuts

kinematics), the background to the π^0 should fall as a function of p_t.

In contrast, the π^0 signal itself should increase as a function of p_t as can be seen from table 4. At a trigger p_t of 3 GeV/c the probability that a π^0 causing a (1,1) trigger in ILSA throws its other γ into ILSA is twice that of a photon at a p_t of 1.5 GeV/c.

One therefore expects that at high trigger p_t the π^0 peak will dominate over the background peak. Figure 25b shows the $\gamma\gamma$ mass plot for trigger p_t's above 2.2 GeV/c. The π^0 peak does indeed stand out above the background. Because of the low energy of the additional reconstructed photons the energy measurement is poor so the width of the peak is not unreasonable.

Some of the events on figure 25b could still be due to accompanying hadrons. On figure 26 is plotted the shortest distance, in projection, between one of the newly found ILSA 'photons' and the extrapolated impact of a charged track. As expected, there is a peak at low values.

Events are therefore rejected in which

a. An extra 'photon' is reconstructed in the trigger quadrant when the relaxed cuts are applied.

b. There is no extrapolated charged track within 10 cm of that 'photon'.

No mass requirement is made of the $\gamma\gamma$ combination since even at low masses there will be quite a reasonable fraction of genuine π^0's because of the resolution.

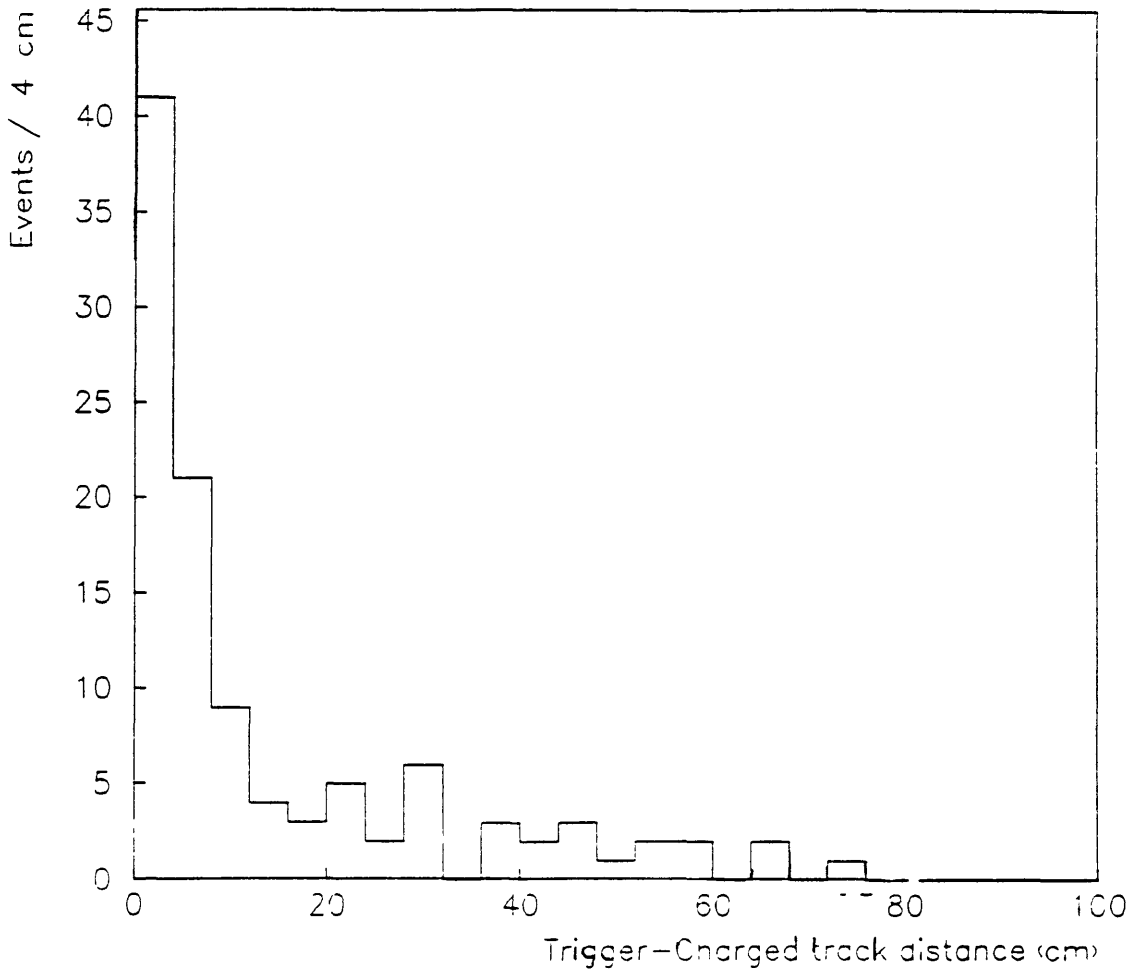


Figure 26: 'photon'-charged track distance in projection. The shortest distance, in projection, between a 'photon' reconstructed by relaxing the cuts and the impact of a charged track.

Having rejected these events the cuts are returned to their old values for the remainder of the analysis.

5.3.3 Making π^0's with γ's in OLGA and CROWN

Up to now, the information available from the CROWN and OLGA calorimeters has not been used at all. At this stage an attempt is made to find a π^0 by combining ILSA triggers with γ's from the other calorimeters. No attempt is made to combine ILSA triggers with

photons from other ILSA quadrants since the minimum distance between a trigger and another quadrant is 45 cm and at reasonably high trigger p_t (and hence energy) equation 3.4 determines that the energy of the 'other' γ be too low to be found.

An energy cut of 1 GeV is applied to the OLGA and CROWN γ's and the resulting $\gamma\gamma$ mass plots are shown in figure 27. Any combination of an ILSA γ with an OLGA γ whose mass M is in the range 90 MeV/c^2 < M < 180 MeV/c^2 is called a π^0 and the event is rejected from the single γ data set. In the case of combinations with the CROWN the range taken is 70 MeV/c^2 < M < 200 MeV/c^2.

5.3.4 Electrons from photon conversion in the target

The NA-14 ^{6}Li target plus scintillator active target contain a total of 15% of a radiation length of material. One of the photons from a π^0 decay can convert in the target leaving just one to give a trigger in ILSA. If the mass of the π^0 is ignored the electron positron pair so produced will be travelling in the same direction as the trigger photon. If either the electron or the positron can be found then the event can be rejected.

First the electrons are identified by means of the ratio of the momentum measured in the chambers to the energy deposited on hitting one of the calorimeters. This ratio is shown in figure 28. Any particle with .7 < P/E < 1.5 is defined to be an electron.

For the electrons the quantity θ is plotted (figure 29), where θ is the space angle between the electron and the trigger. The entries are weighted by $(1/2\pi\theta)$ to take account of the solid angle effect. Events with an electron at θ < 50 mrad are rejected.

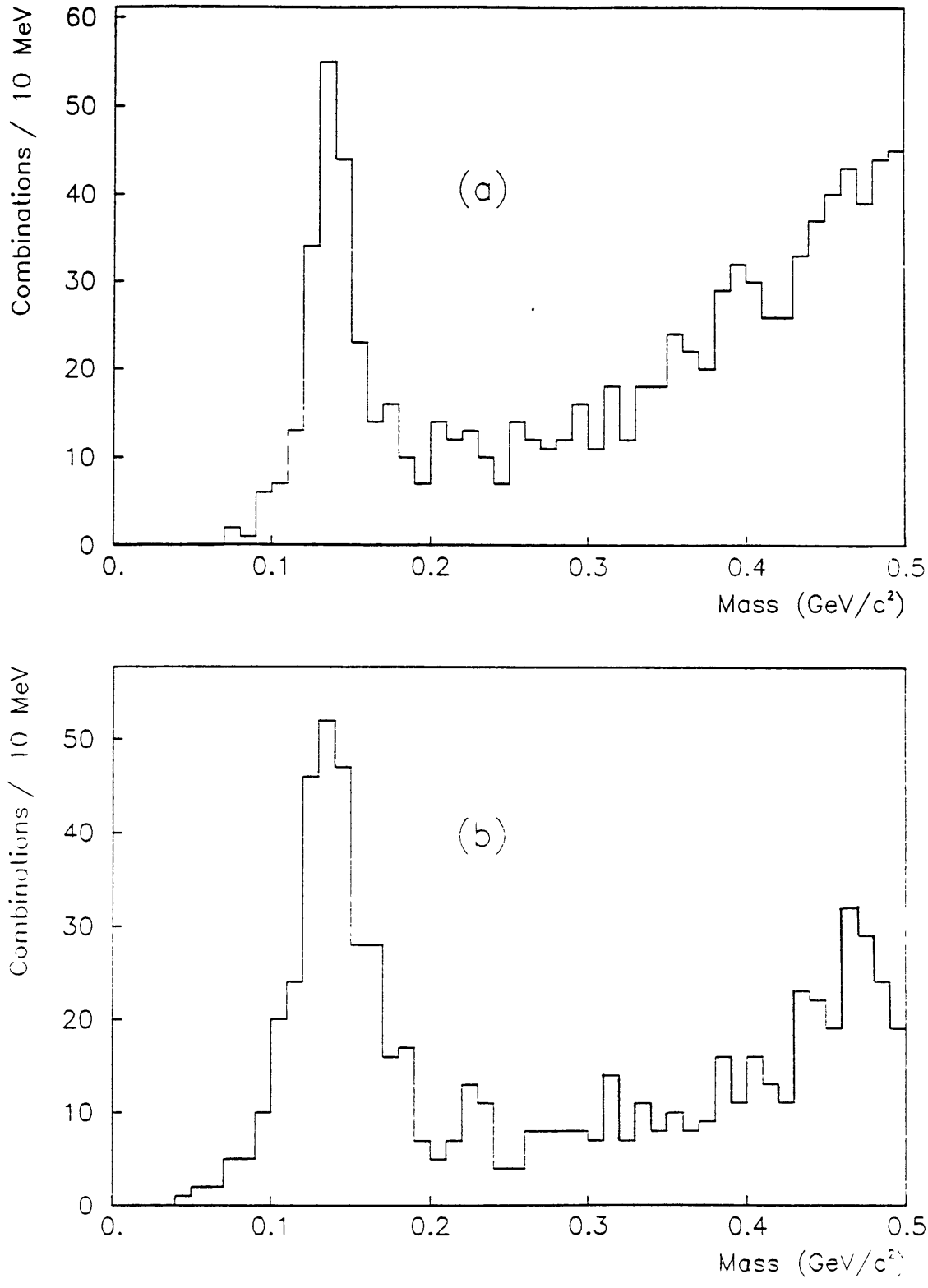


Figure 27: $\gamma\gamma$ invariant mass plots combining ILSA triggers with photons in (a) OLGA, (b) CROWN

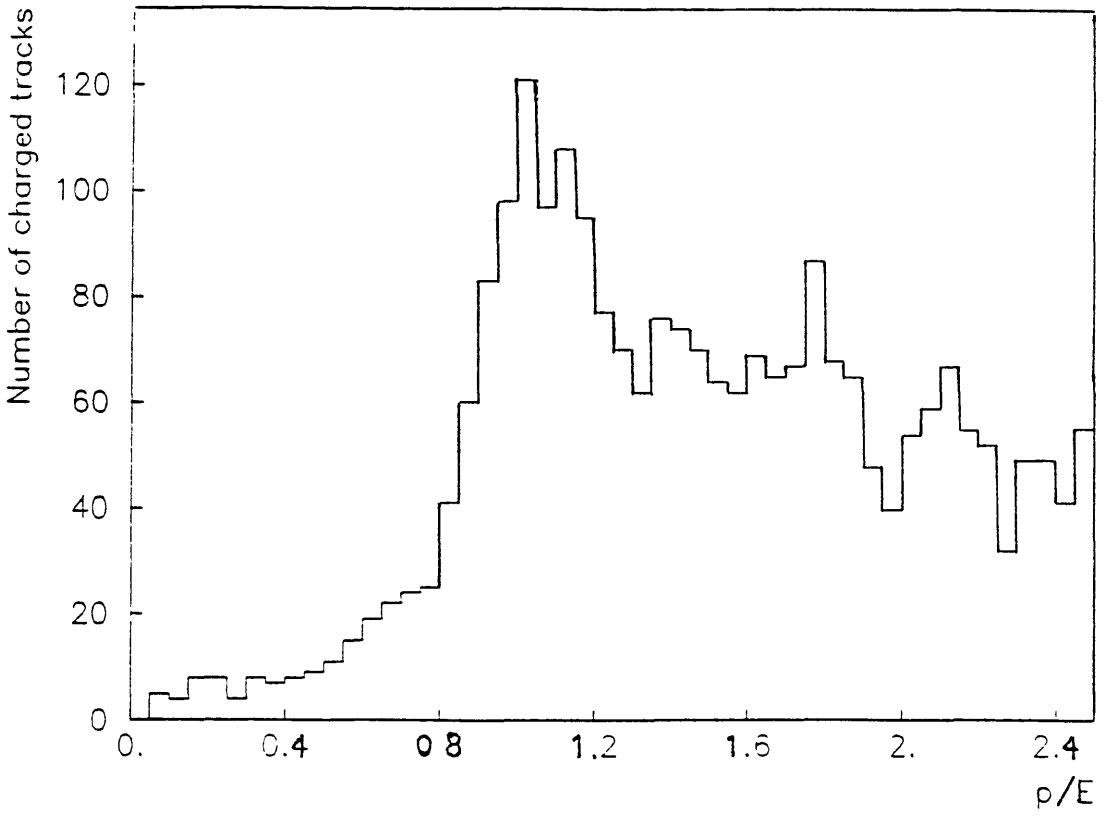


Figure 28: P/E for charged tracks hitting the calorimeters. An electron is defined as a particle with $0.7 < p/E < 1.25$.

5.4 Assessment of the enrichment achieved.

The sample to be used in the analysis is that containing photons with $p_t > 2.45$ GeV/c. From figure 24 can be extracted the numbers of events believed to be present as indirect background and as hard scattering candidates. These numbers are shown in table 5. Also given are the numbers of events expected from the Born term calculation and from Born term plus higher order corrections. This is not exactly the same number as appear on the inclusive plot because that has been corrected for the random vetoing of events because of hits in the μ filter. Additionally, about 4% of the events

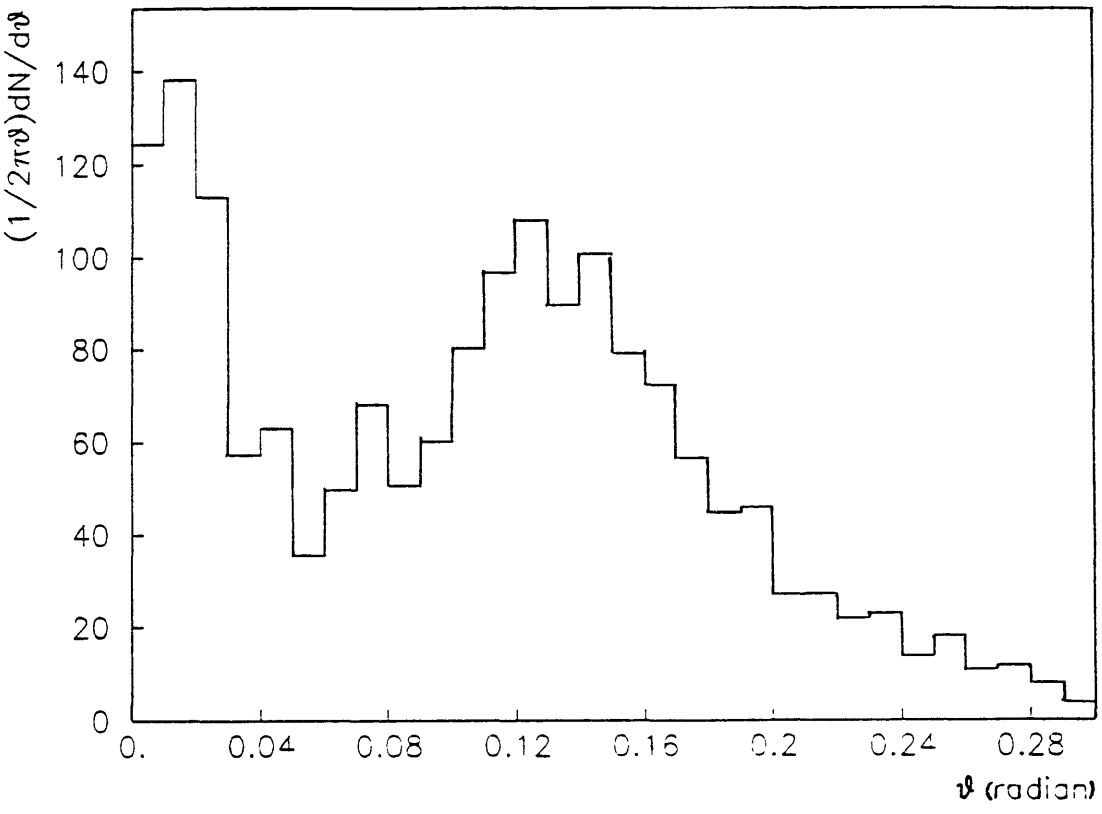


Figure 29: Angular distribution of electrons about the trigger particle. The quantity $(1/2\pi\theta)dN/d\theta$ unfolds the solid angle effect to give the number of electrons per unit solid angle.

were dropped by the track fitting program [8] These events are included in the inclusive plot with no check on the possibility of there having been a charged track pointing towards the trigger particle. This has negligible effect on the plot since only about 5% of the events are caused by charged particles. For the analysis of topology and charge asymmetry the events are obviously useless so the numbers in table 5 have been scaled down from those measured and calculated for the inclusive plot. The prompt signal is not directly comparable to the expected theoretical numbers because some

[8] This problem has since been found to be data independent.

genuine prompt events may have been thrown away in the process of enrichment. The uncertainty in the sensitivity of 20% should also be borne in mind.

Table 5: Measured and theoretical origin of events above 2.45 GeV/c.

Total number of events	238
Indirect background	142
Prompt signal	96
Born Contribution	60
Born + higher orders	88

The fraction of all the events in the $\gamma N \rightarrow \gamma X$ sample rejected by each of the cuts already discussed is shown on figure 30 as a function of trigger p_t. The relevant question however is; has the QED Compton:non-QED Compton ratio been improved by the process and, if so, has it been done without seriously affecting the size of the sample? This is discussed below.

Merged π^0's: It is not possible to use the VDM monte-carlo to estimate how many π^0's have been rejected by tightening this cut. In the monte-carlo, on no occasion when there is only one γ hitting the trigger quadrant does the cut throw away the event. However the distribution of P for the real data has a rather different shape in the region $.7 < P < 1$ (figure 20).[9] It may not be

[9] This may well be due to the uncertainty in the relative calibration of the Ariadne fingers which is not well simulated in the monte-carlo.

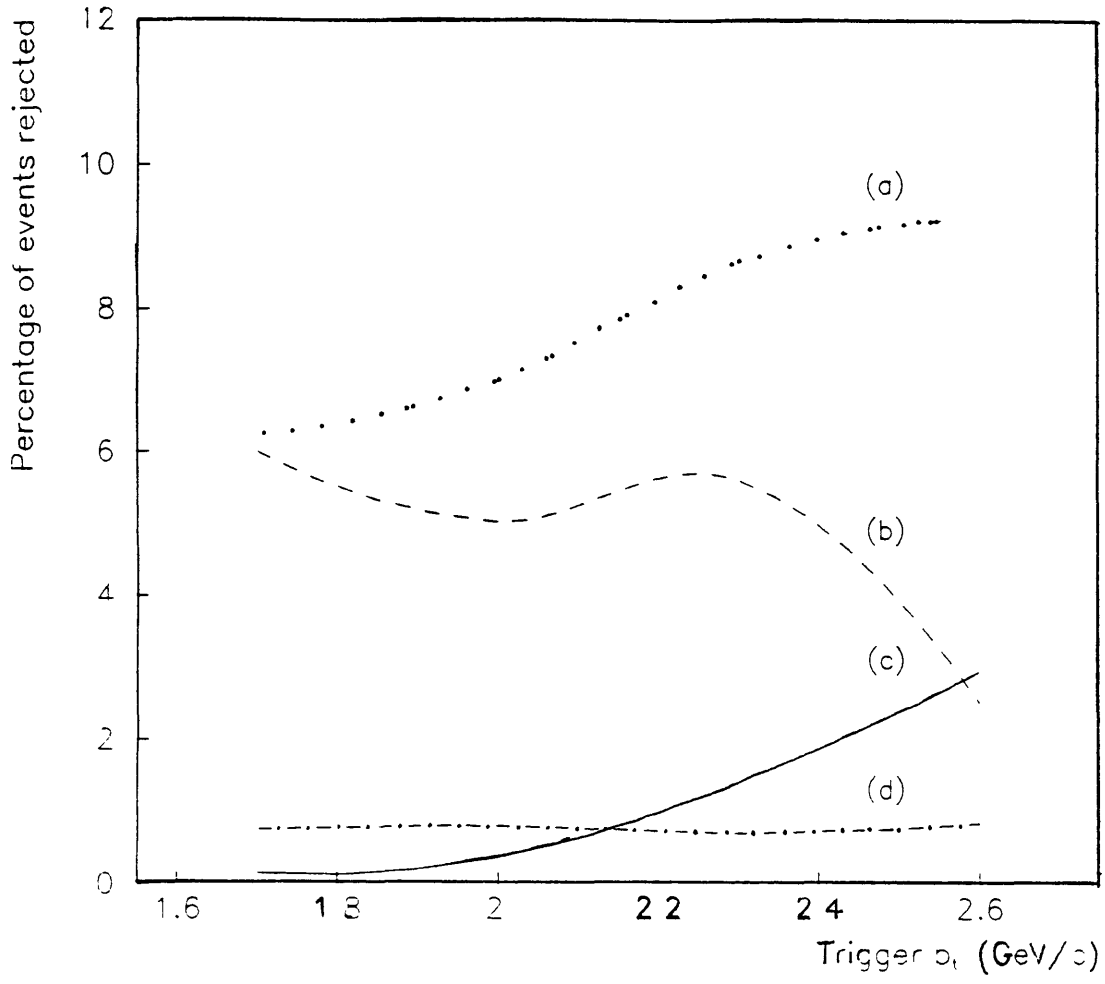


Figure 30: Fraction of events rejected by enrichment as function of p_t

(a) Relaxation of reconstruction conditions.
(b) π^0's made with OLGA,CROWN γ's.
(c) Merged π^0's.
(d) Electrons from photon conversion.

valid, therefore, to assume that the cut is 100% efficient.

Figure 30 shows quite clearly that this cut has its greatest effect at high trigger p_t. This is exactly as expected since π^0's at high p_t (and hence high energy) are more likely to have their two γ's merged in ILSA. It seems not unreasonable, therefore to assume that about 2/3 of the 7 events rejected above trigger p_t = 2.45 GeV/c are indeed merged π^0's.

Relaxation of reconstruction conditions: It is difficult to estimate the effect of this cut. The VDM monte-carlo could perhaps be used but it is in just this kind of situation (low energy, very early or very late shower development) that one would expect it to be at its least accurate. The mass plot (figure 25b) indicates that at high p_t between 60% and 70% of the events rejected by this cut are genuine π^0's. 22 events are rejected from the sample.

π^0's made with OLGA,CROWN: From the effective mass plots (figure 27) the π^0 signal/background ratio is about 3 in the case of OLGA and 8 for π^0's made using a photon from the CROWN. A total of 6 events is rejected, 2 by OLGA and 4 by CROWN, and these should be approximately 100% genuine π^0's.

Electrons from photon conversion: This signal is again quite clean (figure 29) but unfortunately only 2 events are rejected. This is not entirely unexpected since the average photon traverses just 7% of a radiation length in the target and only about 7% of the approximately 100 π^0's in the sample will have a converted 'other' gamma. The pairs will be of quite low energy (section 3.2) and to have a good chance of recognition they must therefore be asymmetric and hence 2 events is reasonable.

A total of 37 of the original 238 events are rejected of which one would expect about 25-30 to be genuinely reconstructed π^0's. Taking all these effects into account the prompt/total ratio improves from 40% to 45%. However it should be noted that for the purposes of the analysis of topology and charge asymmetry many of the higher order processes are not relevant. Either they do not contribute to the asymmetry or they have a different topology from the one shown by

the Born diagram. Those, like the box diagram, which would be expected to contribute are only a small part of the cross-section at $p_t > 2.45$ GeV/c.

If one just considers the Born diagram contribution (assuming it to be present in the prompt signal in the theoretically calculated proportion, then the ratio signal/total has improved from 27% to 31%.

- Chapter 6 -

TOPOLOGY AND CHARGE ASYMMETRY IN DICS EVENTS.

6.1 Introduction

Any measure A_γ can be represented as

$$A_\gamma = \varepsilon A_{QED} + (1-\varepsilon)A_{back} \qquad (6.1)$$

If the measure A is the charge asymmetry or some measure of event topology, then for the reasons discussed in the previous chapter, A_{QED} represents essentially the lowest order contribution and A_{back} the indirect background plus higher order corrections.

Starting from the inclusive measurement (i.e. $A_\gamma = dN_\gamma/dp_t$) and taking into account the enrichments achieved then one has a value for the single photons above 2.45 GeV/c of

$$\varepsilon = .31 \pm .04 \qquad (6.2)$$

where the error is purely statistical. For confirmation of this result, one turns to the features of the hadrons in the events which will provide a value for ε entirely independent of that from the inclusive study.

One further demand is made of the data before looking at the topology and the charge asymmetry. As mentioned in section 5.1, the QED monte-carlo does not include any information about the beam. In real data, when there is no track measured before and after Goliath, the beam information plays an important role in vertex reconstruction. Therefore, in order to make the comparison with

monte-carlo more realistic and improve the quality of momentum measurement , events are only considered if they contain, fitted to the vertex, at least one track measured both upstream and downstream of Goliath. Unfortunately this removes 37 events from the prompt γ sample leaving just 164 events to be analysed.

In this chapter, first the topological aspects of the events are investigated, then the search for a charge asymmetry is described. Finally the results are discussed and conclusions drawn.

6.2 Topological Aspects

Three methods of studying the topology of the events are used, the aim being to extract a value of ε from equation 6.1. VDM has been seen to describe very well the production of π^0's seen in ILSA. It is, therefore, justified to add to this dataset, those containing the $\pi^-X \rightarrow \pi^0 N$ and $\pi^-X \rightarrow \gamma N$ events to produce a relatively high statistics representation of what the VDM events in the candidate prompt photon sample look like topologically. This dataset is referred to in the remainder of this thesis as the 'indirect dataset'. The $\gamma N \rightarrow \gamma X$ events are then compared to this combined dataset and to the QED monte-carlo events to produce a value for ε.

The events may be topologically biased by the requirement that only 1 shower (in the case of the single photons) and 2 showers (for the π^0's) be reconstructed in the trigger quadrant. Also, the enrichment process, to the extent that it does not remove exclusively events caused by π^0's, adds a topological bias. For these reasons, only charged particles are used in the topology studies.

6.2.1 Acceptance Correction

The general philosophy of this analysis is that acceptance effects can be ignored because they apply equally to γ beam and π^- beam, to both single γ triggers and π^0's. However a significant fraction of the π^- beam data was recorded with the moustache regions of the chambers active, rendering it not directly comparable to the rest of the data. Additionally, in the azimuthal distribution of charged tracks (section 6.2.2) the effect is quite strong and while it does not affect the difference between single photons and indirect background it would make the quantification of the effect more difficult. At any rate, it is necessary to make a correction to demonstrate that the unusual features of the distributions are due to acceptance effects.

The method of correction described here in relation to the azimuthal distribution of charged tracks about the trigger applies equally to the other distributions shown in this chapter.

The QED monte-carlo data was digitized twice: once with the moustaches active and once with them inactive. The $\Delta\phi$ distributions for these datasets are shown in figure 31a,b. Dividing these plots, point by point, produces the dashed line on figure 31c. The data points on figure 31c are those of the $\gamma N \rightarrow \gamma X$ dataset before correction (the scale refers to these points). Multiplying these by the correction produces the plot of figure 31d. All 'indirect' data recorded with the moustaches inactive was summed, corrected and then added to the moustaches active data to produce the final indirect plots.

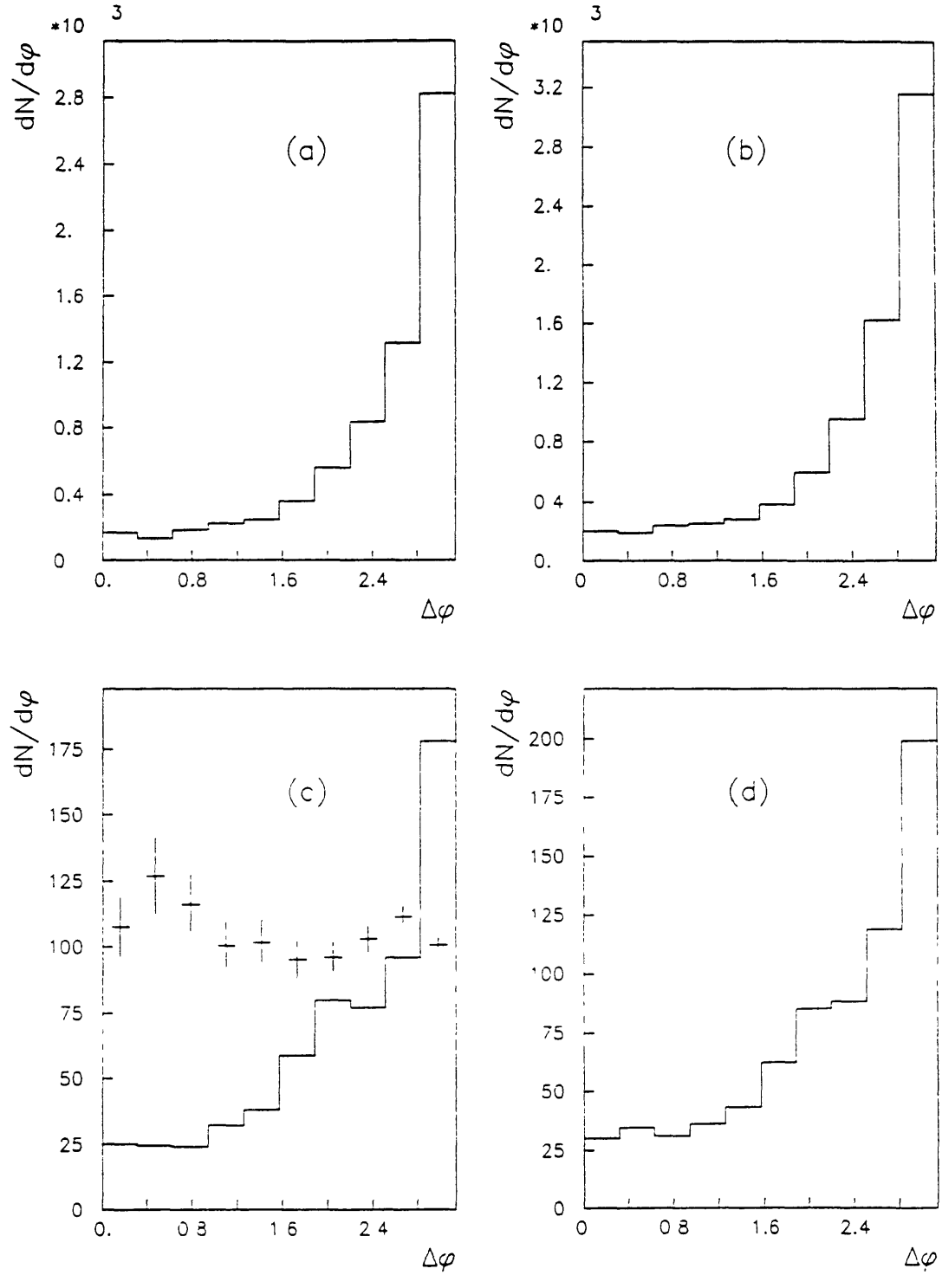


Figure 31: Correcting for moustache acceptance in Δφ plots. The moustaches active monte-carlo plot (a) is divided by the inactive plot (b) to produce the points on (c), the uncorrected distribution of real data. Multiplying curve (c) by this correction produces (d).

6.2.2 Azimuthal Distributions

The first measure of event topology considered is the simple azimuthal distribution of charged tracks measured from the trigger direction, $\Delta\phi$. This distribution is shown for the prompt photon candidates in figure 32. The dashed histogram on the same figure is the indirect $\Delta\phi$ plot normalised to the same number of events as are present on the single photon plot.

There is a significant difference between the two, particularly in the region of $\Delta\phi = \pi$. Here, the single photon distribution peaks sharply as would be expected if the photons have quark jets recoiling against them. The indirect events do not necessarily have such jets and should not therefore be so sharply peaked. This is just the behaviour observed. Additionally, the prompt γ candidates have fewer particles close to $\Delta\phi = 0$. This is expected because of the topology of the Born term contribution to QED Compton scattering.

At low p_t these effects should not exist as the single photons are from the same source as the indirect events: VDM. The same plot for all trigger p_t's is shown in figure 33. The single photon and indirect distributions are closely similar. There are only small differences and in any case these are largely accounted for by the fact that the single photon distribution does still include all the hard scattering events.

In order to extract a value of ε, the single γ distribution is considered to consist of a linear sum of the indirect background and the QED Compton events (i.e. the QED monte-carlo). To the normalised indirect and QED monte-carlo distributions were fitted fourth order polynomials, $y_1(\Delta\phi)$ and $y_2(\Delta\phi)$ (figure 34a,b).

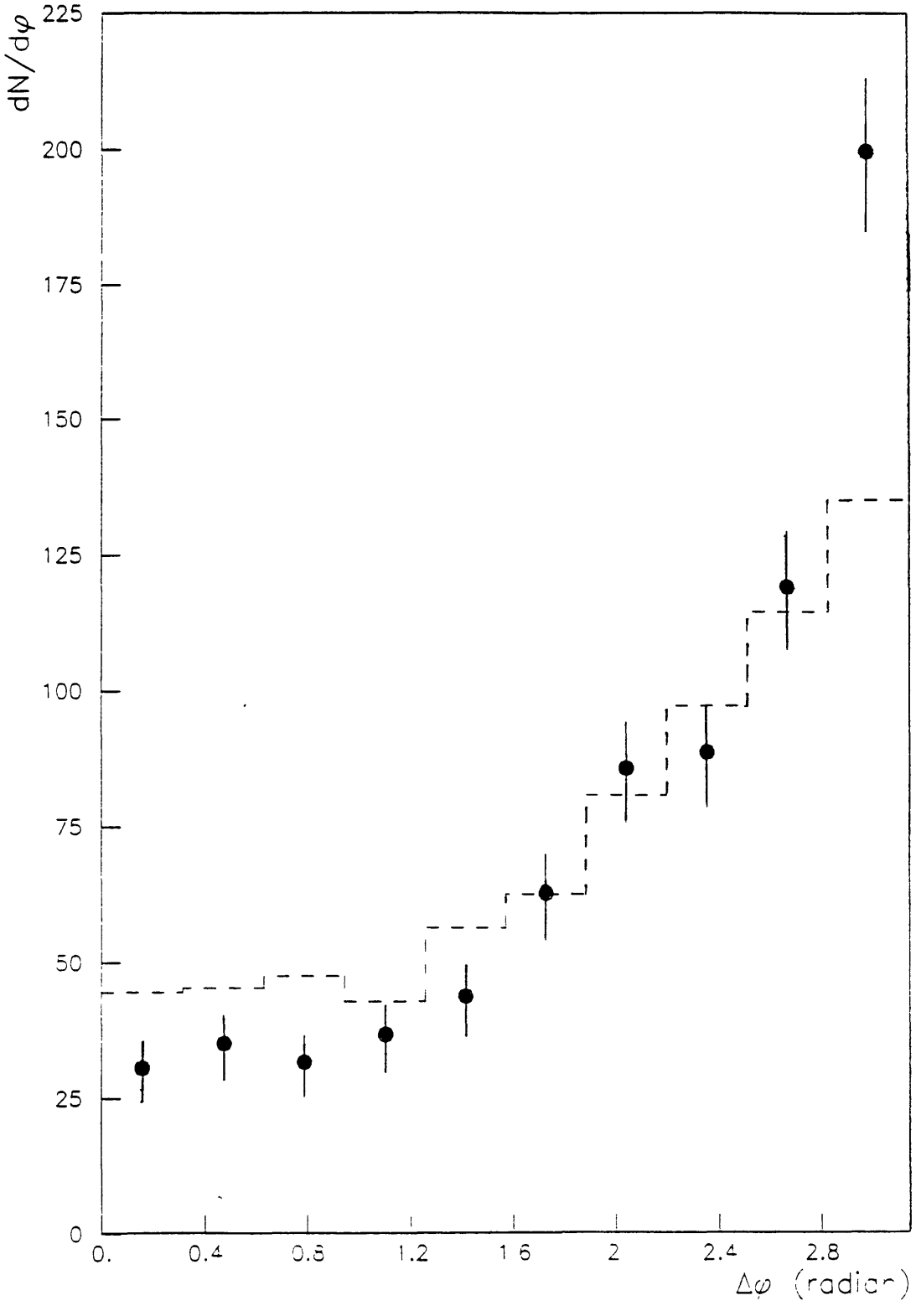


Figure 32: Azimuthal distribution of charged tracks about the trigger photon in $\gamma N \rightarrow \gamma X$ interactions at high p_t. The dashed line shows the same distribution for indirect events.

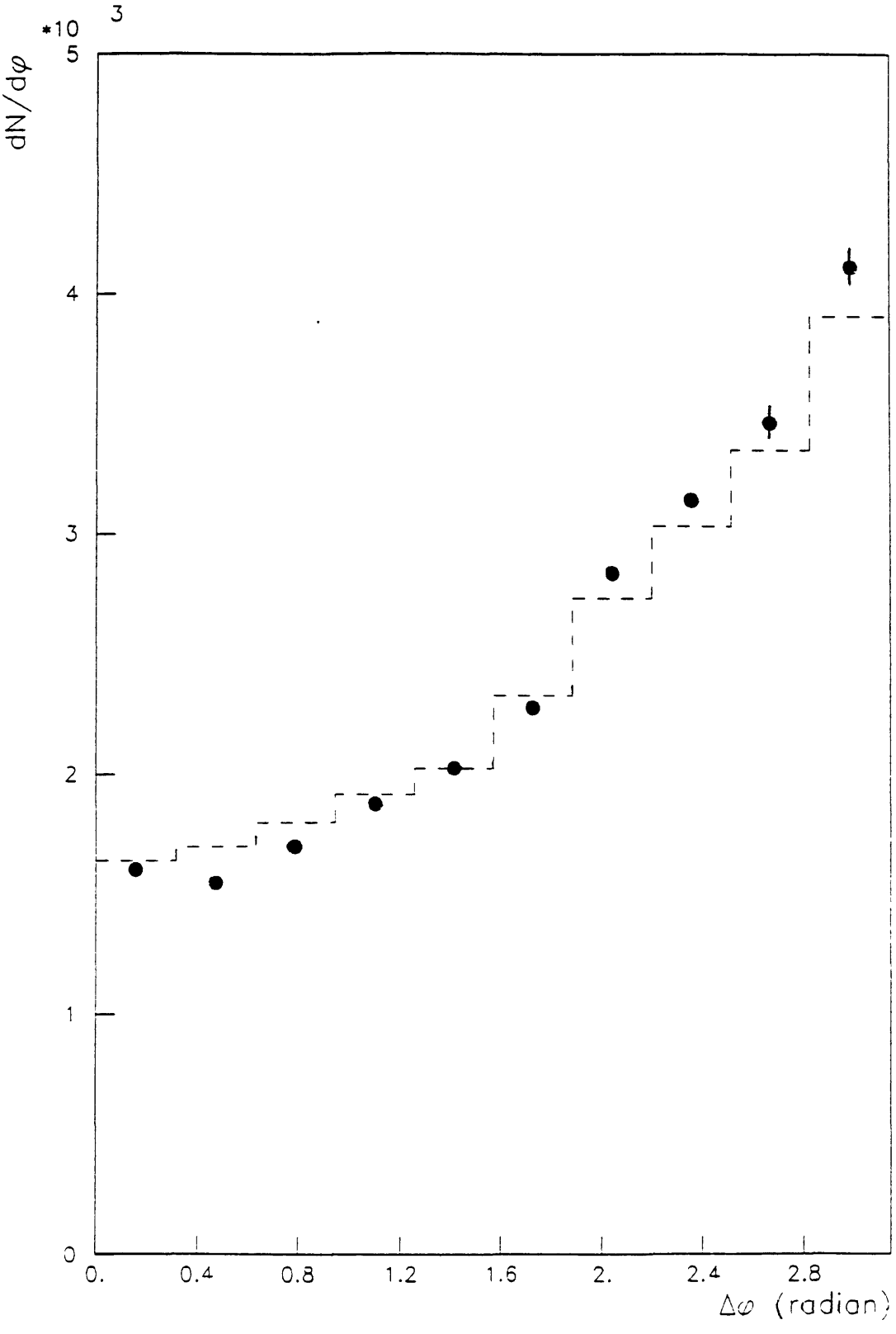


Figure 33: $\Delta\phi$ distributions for trigger p_t > 1.5 Gev/c.

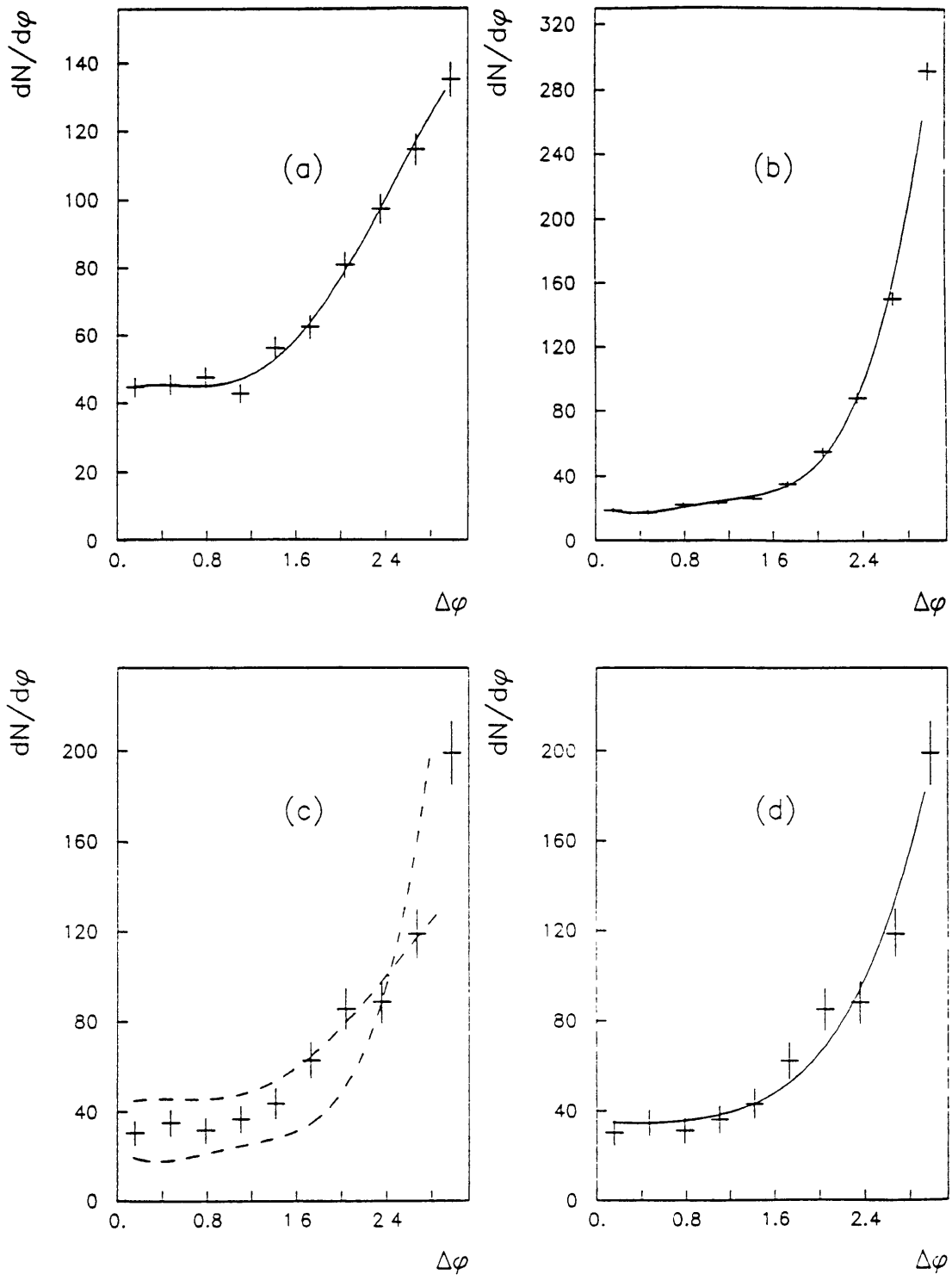


Figure 34: The extraction of ε from Δφ distributions. (a), (b) are indirect and QED monte-carlo data with fitted order-4 polynomials. (c) is photon data with curves (a),(b) superposed, (d) the photon data with the best linear sum of curves (a),(b) superposed.

Since from equation 6.1 we know that

$$y_\gamma = (1-\varepsilon)y_1 + \varepsilon y_2 \qquad (6.3)$$

where y_γ is a curve describing the single photon data, it is possible, by fitting a linear combination of y_1, y_2 to the candidate prompt photon distribution, to obtain a value of ε. These data points along with the curve y_γ so obtained are shown in figure 34d.

The resulting value is $\varepsilon = .36 \pm .08$. The error includes only that due to the γ data points. This is not too serious since the indirect and especially the QED monte-carlo statistical errors are somewhat smaller then are those on the γ data points. There may also, however, be significant systematic errors due to the fact that the indirect events are not a good description of the topology of higher order QED contributions and the fact that the monte-carlo does not include an exact simulation of the apparatus. In addition, the result will be biased to the extent that the polynomials chosen are not a correct analytical representation of the distributions fitted. The result is therefore consistent with that obtained from the inclusive analysis. When the same procedure is applied to distributions of data with trigger $p_t > 1.5$ GeV/c the resulting value is $\varepsilon = .05 \pm .01$.

Another way to look at the distribution in the azimuthal angle $\Delta\phi$ is to plot the flow of the energy fraction ξ where:

$$\xi = E_{ch}/E_{tot} \qquad (6.4)$$

where E_{ch} is the energy of the charged particle
E_{tot} is the total energy of the event

This is shown in figure 35 and the result is very similar to that obtained for $\Delta\phi$. The single photon distribution is again lower for small $\Delta\phi$ and rather more strongly peaked towards $\Delta\phi = \pi$. Carrying

out the same procedure as in the previous case produces the result: $\varepsilon = .42 \pm .13$ at high trigger p_t compared to $\varepsilon = .08 \pm .02$ when $p_t > 1.5$ GeV/c is considered.

It should be noted that if similar plots are made of the distribution of neutral particles in the events, the photon data turns out to have greater accompaniment than the indirect trigger particles. This is to be expected since a considerable fraction of the photon events are caused by neutral meson $\overset{\text{interactions}}{\Lambda}$ where the parent particle has not been reconstructed.

6.2.3 A More Sophisticated Measure

The azimuthal distribution of charged tracks does indeed show a difference in topology between indirect events and γ events. It can be improved upon, however, by making use of the angle information which thus far has been ignored. The polar angle $\theta = \tan^{-1}(p_t/p_x)$ is not Lorentz invariant and is therefore not itself a good measure to use. The variable chosen is the pseudorapidity η:

$$\eta = -\ln(\tan(\theta/2)) \qquad (6.5)$$

Although this too is not invariant, differences in pseudorapidity are. To then combine the azimuthal information with the $\overset{\text{polar}}{\Lambda}$ angle information the quantity X is defined where:

$$X = \sqrt{[\ (\Delta\eta)^2 + (\Delta\phi)^2\ ]} \qquad (6.6)$$

A particle at $\theta = 100$mrad (this is the average angle covered by ILSA) has a pseudorapidity of about 3 and since $0 < \Delta\phi < \pi$, the two variables have approximately the same magnitude.

The X-distribution for γ's with $p_t > 1.5$ GeV/c is shown in figure 36. Since the distribution falls very rapidly for $X > 3.25$, for the purposes of the comparison only the region $X < 3.25$ is used.

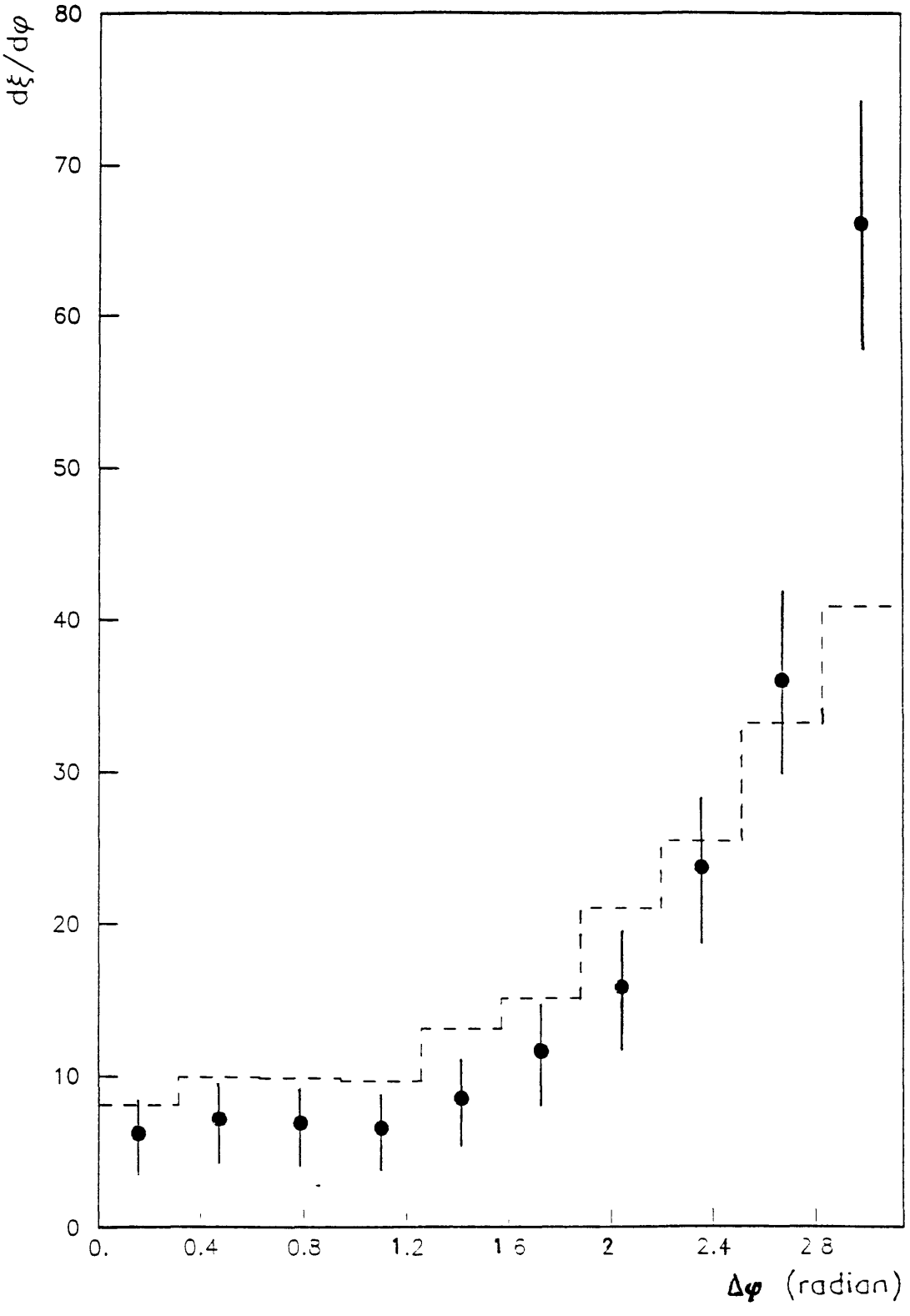


Figure 35: ξ as a function of $\Delta\phi$ for $p_t > 2.45$ GeV/c.

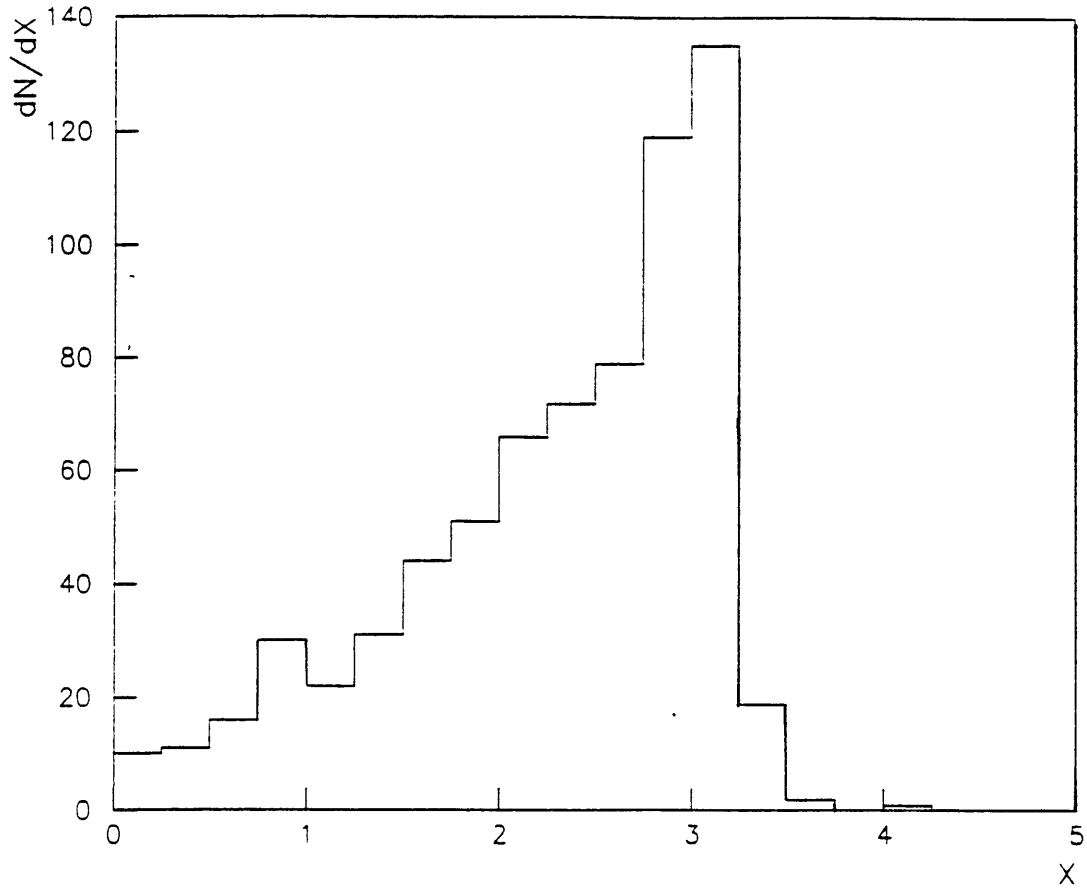


Figure 36: X-distribution for γ events with p_t > 2.45 GeV/c

Figure 37a shows again the distribution of X in single photon events, the dashed histogram being the distribution obtained for the indirect dataset As expected the two distributions are very similar Figure 37b shows the same thing again for trigger p_t > 2.45 GeV/c and there is, as with the azimuthal distributions, an appreciable difference. The γ's have less accompaniment at X=0 and the distribution is more strongly peaked as X=3.25 than is the indirect distribution.

ε can be computed as before by fitting polynomials to the indirect and QED data points and then finding the linear combination which

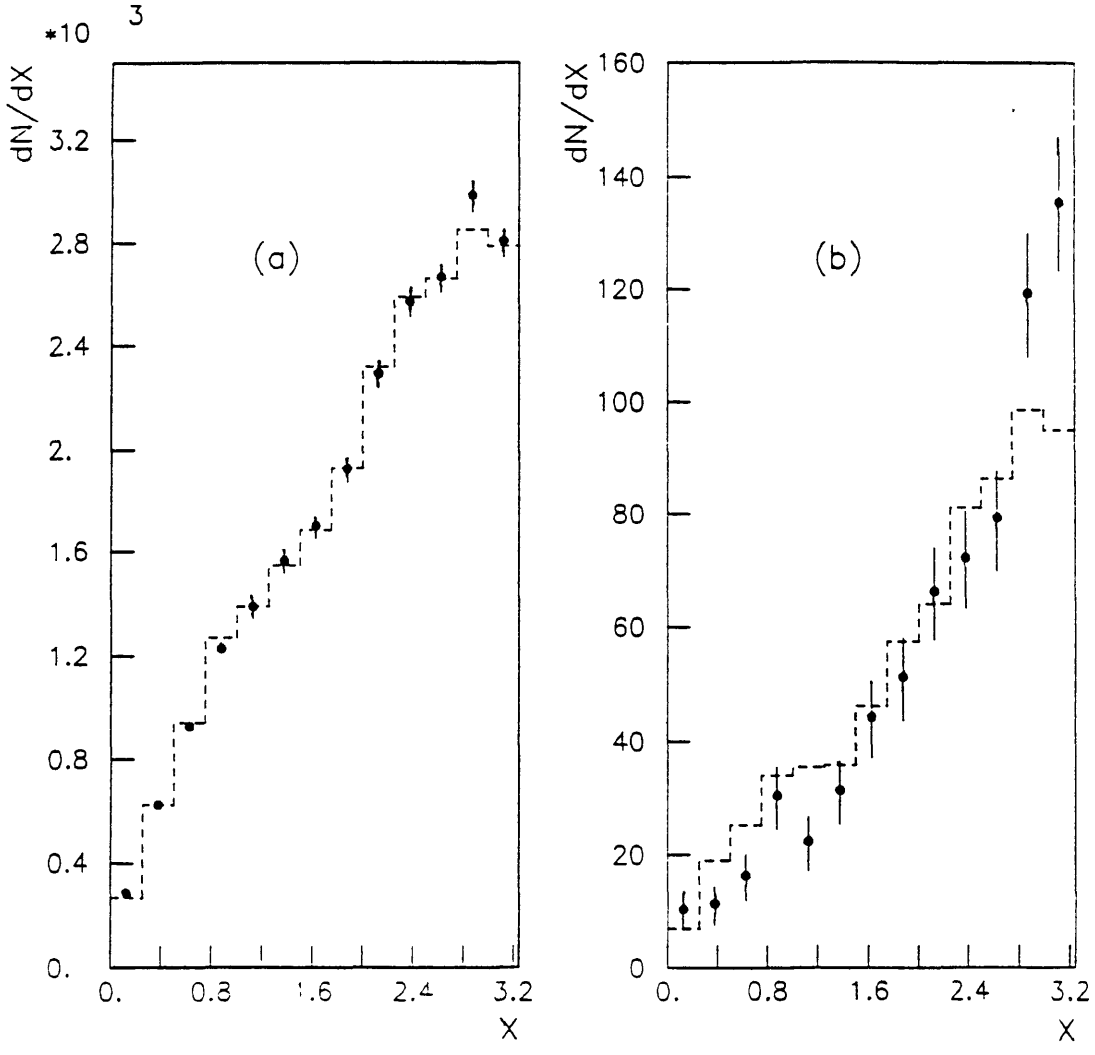


Figure 37: X-distributions at (a) all p_t, (b) $p_t > 2.45$ GeV/c. The data points are photon data, the dashed lines indirect data.

best describes the single photon data. Figure 38 shows the X-distribution with the various polynomials superimposed. From this ε is found to be .35±.08 in agreement with previous values.

6.2.4 A Lund Clustering Algorithm (LUCLUS)

LUCLUS is a routine, provided with the Lund monte-carlo program for e^+e^- physics, which uses a simple clustering algorithm to find

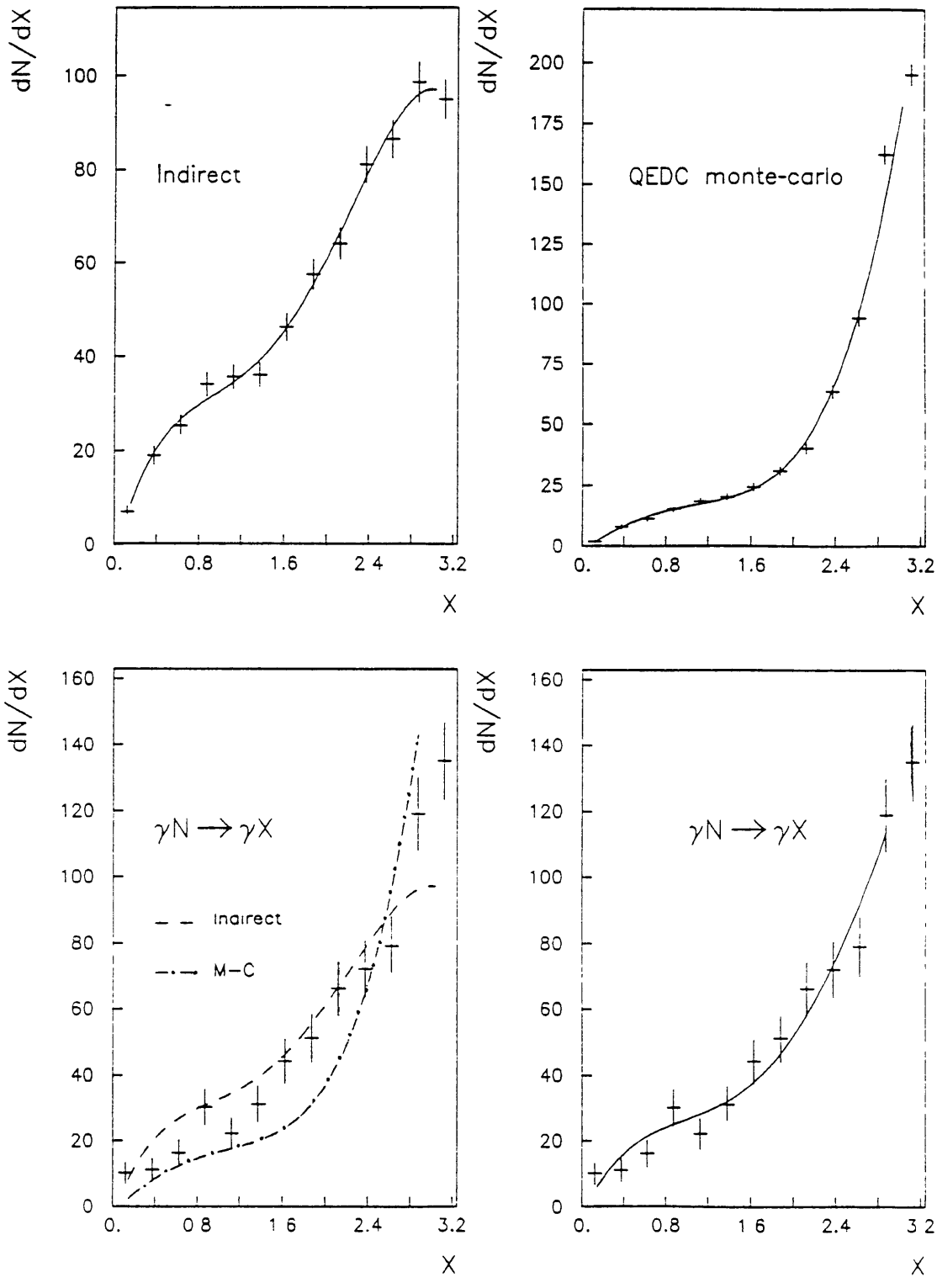


Figure 38: Evaluation of ε from X-distributions. The same method is used as was used for the Δφ distributions.

jets. It is apparent that at the centre of mass energies available to NA-14 (about 13 GeV) it is highly unlikely that jets could be found in the laboratory frame. However, LUCLUS does provide a simple, objective measure of the topology of events and should indicate differences, if differences there be, between indirect events and single γ's.

The algorithm is described in detail elsewhere.[50] It relies on the fact that particles in a jet have limited transverse momentum relative to the jet direction. A variable d_{ij} is defined as

$$d_{ij}^2 = \frac{4p_i^2 p_j^2 \sin^2(\theta_{ij}/2)}{(p_i+p_j)^2} \qquad (6.7)$$

where p_i, p_j are the momenta of clusters i,j
θ_{ij} is the space angle between the clusters.

This quantity measures, for small values of θ_{ij}, the transverse momentum of 2 clusters relative to the direction given by the sum of their momenta. To begin with each particle is treated as a separate cluster. A parameter d_{join} is input and when 2 clusters are found with $d_{ij} < d_{join}$ they are combined to form a single cluster. The procedure is iterated until a stable state is achieved.

An energy cut $E > 3$ GeV/c was imposed to remove from the events tracks due to target fragmentation and then the value of d_{join} was chosen by tuning it until the algorithm found 2 jets (and only 2 jets) in 70% of the QED monte-carlo events.

Table 6 shows the fraction, as a function of p_t, of γ, indirect and monte-carlo events in which LUCLUS found 2 jets, one of them being the isolated trigger particle. In this case the indirect dataset does not include those π^- beam events recorded with the moustache

areas of the chambers active. This is because, unlike for the other topology methods, there is no obvious way to correct the other datasets for the acceptance effect. The value of ε necessary to reproduce the γ result from the indirect and monte-carlo data is also shown.

Table 6: The LUCLUS jet finding results.

Trigger p_t	γ	Indirect	m-c	ε
> 1.5 Gev/c	3.54±.25	2.55±.19	30.8±.55	.03±.01
> 2.45 Gev/c	44±4	31±2	62.5±1	.43±.13

The value of ε (.43±.12) at high p_t agrees well with the evaluations already made.

6.3 Charge Asymmetry

The existence of a +/- charge asymmetry in the leading particle of the spray of hadrons which balances the trigger in p_t, is a crucial test of the proposition that the excess of high p_t photons is caused predominantly by QED Compton scattering. Unfortunately, the quantity of data available is small so that the extraction of a statistically significant result is even theoretically unlikely.

The single γ data set, consisting of 164 events should, given equation 6.1, contain a Born term contribution of about 41 events. Assuming that all of these have a positive leading hadron in the final state, and that all other contributions lead to zero asymmetry, the

+/- ratio detected would be about 100:60. Fragmentation, the presence of neutral hadron leaders, and experimental inefficiency all conspire to wash out this effect making it very difficult to detect.

Two different definitions of the leading particle are used in the analysis: the 'p_t-leader' and the 'E-leader'. The p_t-leader is defined as the particle with the most positive p_{opp} where:

$$p_{opp} = -p_t^i \cdot p_{tt} \qquad (6.8)$$

where p_{tt} is the trigger p_t
and p_t^i is the p_t of the hadron

The energy leader is defined as the highest energy particle with positive p_{opp}.

The variable used to quantify the asymmetry is

$$\alpha = \frac{N^+ - N^-}{N^+ + N^-} \qquad (6.9)$$

where N^+ is the number of positive leaders
and N^- is the number of negative leaders

The numbers, as a function of trigger p_t, of positive and negative p_t-leaders is shown in table 7 The corresponding figures for the E-leader definition are contained in table 8. In all cases the number of neutral leaders found is about 15% of the total number of events. A few events fail to provide an entry since they do not contain a track with positive p_{opp} having an acceptable $\Delta p/p$.[10]

α was calculated for these same bins and figure 39 a and figure 39b show the results for the p_t-leader and the E-leader respectively. It is clear that no statistically significant result can be extracted from these data. There is, perhaps, a slight indication of a

[10] The $\Delta p/p$ must be less than 25%.

Table 7: Asymmetry results using the p_t definition of leader

Trigger p_t	Events positive:negative		
	γ	π^0	m-c
1.5→T.8	1745:1627	3016:2846	473:333
1.8→2.1	512:472	757:742	1139:705
2.1→2.45	184:154	301:253	858:563
2.45→∞	81:65	116:99	1305:840

Table 8: Asymmetry results using the energy definition of leader

Trigger p_t	Events positive:negative		
	γ	π^0	m-c
1.5→1.8	1698:1735	1376:1438	493:334
1.8→2.1	471:514	751:749	1158:725
2.1→2.45	164:174	293:265	884:561
2.45→∞	83:60	103:99	1337:858

difference between prompt γ's and π^0's at high p_t but the small numbers of events combined with the fact that a ratio has been taken, produce very large errors on the measurements. This result is, however, consistent with the theoretical expectation.

6.4 Conclusions

The inclusive analysis clearly demonstrates the existence of an excess of high p_t photons in the high energy γN interactions. It can be

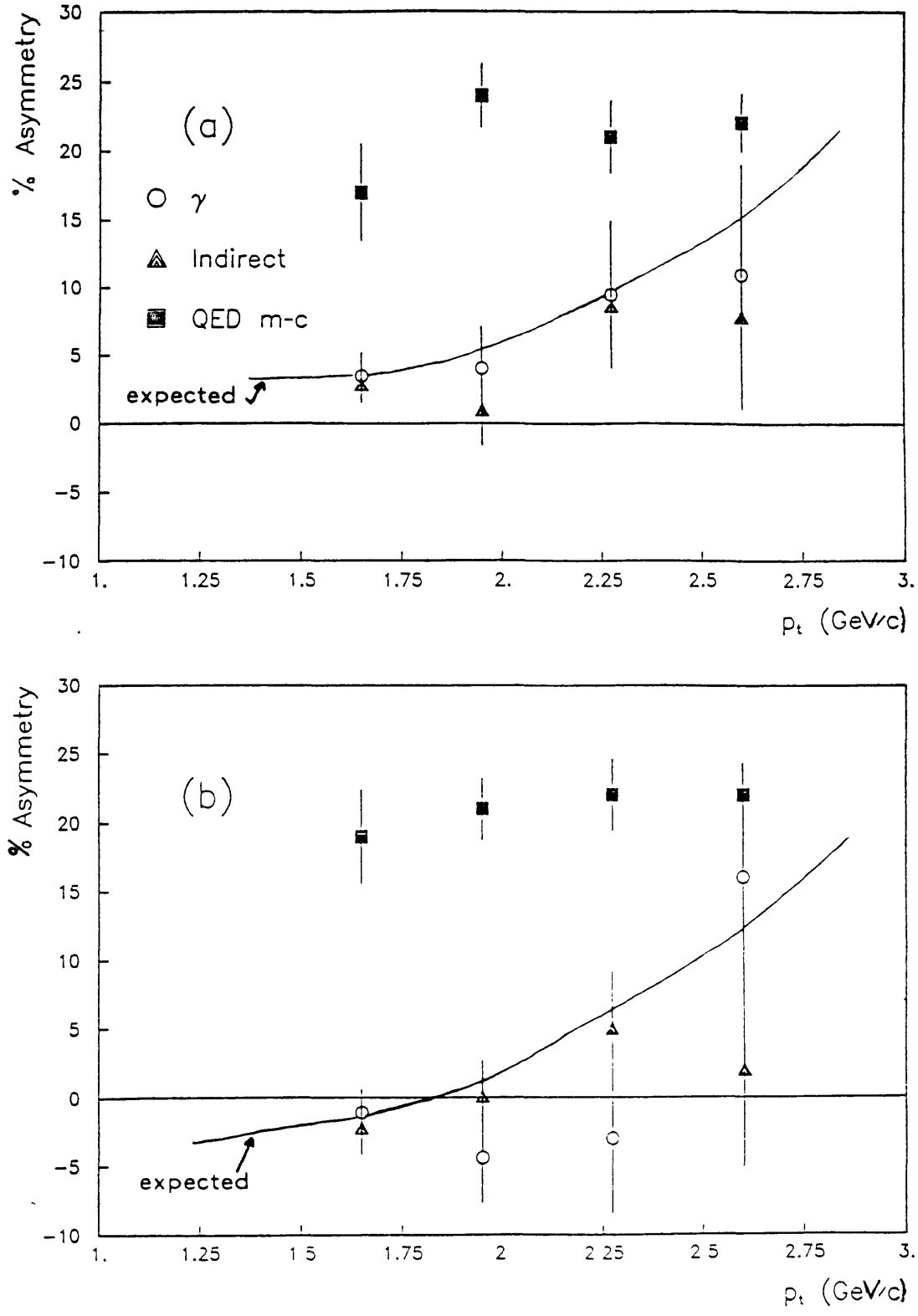


Figure 39: Asymmetry as a function of p_t. (a) p_t-leader definition. (b) E-leader definition.

The 'expected' lines show the expected asymmetry in the γ dataset calculated using α values from the inclusive plot in conjunction with the monte-carlo and indirect data points.

argued that all experimental effects tend to flatten the p_t spectrum but this has been taken into account by comparing the results to those obtained using a π^- beam. This comparison indicates that all experimental effects are understood and under control.

The magnitude of the inclusive signal is consistent with it having been caused by events where the incident photon has coupled directly to the constituents of the nucleon where those constituents are fractionally charged in accordance with the standard theory of QCD. Theories in which the nucleon constituents have integral charges are disfavoured by the data but cannot be ruled out if the arguments of Lipkin[22,23] are accepted.

Results from an analysis of the charged hadrons in the events support the above conclusions. Topologically the photoproduced prompt photon events appear to be more 'jet-like' in character than are the π^0 events and the pio-produced events. These prompt photons also have fewer charged hadrons close to them in space than do the indirect events. The magnitude of these effects agrees with that expected from the inclusive result.

No charge asymmetry is apparent but this fact is entirely explained by the small magnitude of the expected effect combined with the low statistics.

The topology results are entirely independent of the inclusive result and therefore provide good supporting evidence for the hypothesis that the high p_t prompt photon signal is indeed due to Deep Inelastic Compton Scattering.

REFERENCES

[1] There is a vast amount of literature on the subject of deep inelastic lepton scattering. One of the more recent papers, published by the European Muon Collaboration is :Aubert et al, Phys. Lett. 123B, 275 (1983).

[2] The subject is covered in many papers and reviews. One recent review is: S.L Wu, Phys. Rep. 107, (1984) 59.

[3] J. Bjorken and A. Paschos, Phys. Rev. 185, 1975 (1969)

[4] E. Witten, Nucl. Phys. B120, 189 (1977)

[5] C.H. Llewellyn Smith, Phys. Lett. 79B, 83 (1978)

[6] R.J. DeWitt, L.M. Jones,J.D. Sullivan, D.E. Willen, H.W. Wyled, Phys. Rev. D19, 2046 (1979)

[7] R.J. DeWitt, L.M. Jones,J.D. Sullivan, D.E. Willen, H.W. Wyled, Phys. Rev. D20, 1751 (1979)

[8] G. Donaldson et al, Phys. Rev. Lett., 40 684 (1978)

[9] T. H. Bauer, R.D. Spital, D.R. Yennie, F.M. Pipkin, Rev. Mod. Phys. 51, (1978) 261 and errata in Rev. Mod. Phys. 51, (1979) 407

[10] M-Y. Han and Y. Nambu, Phys. Rev. 139, B1006 (1965)

[11] M-Y. Han and Y. Nambu, Phys. Rev. D10, 674 (1974)

[12] G.M. Vereshkov, S. A. Zharinov, S.V. Ivanov and S.V. Mikhailov, Sov. J. Nucl. Phys. 32, 117 (1980)

[13] Gorski et al., Acta Phys. Pol. B13, 511 (1982)

[14] A.V. Efremov, S.V.Ivanov, S.V. Nesterenko, JINR Dubna preprint E2-82-433 (1982)

[15] J. C. Pati and A. Salam, Phys. Rev. D8, 1240 (1973)

[16] J.C. Pati, Phys. Rev. D10, 275 (1974)

[17] M.S. Chanowitz, Phys. Rev. Lett. 44, 59 (1980)

[18] T. Jayaraman, G. Rajasekaran and S.D. Rindani, Phys. Lett. 119B, 215 (1982)

[19] R.M. Godbole, J.C.Pati, T. Jayaraman, G. Rajasekaran , Phys. Lett. 142B, 91 (1984)

[20] A.V. Efremov, S.V.Ivanov, S.V. Mikhailov, JETP Lett. 32, 669 (1980)

[21] C. Berger et al., Phys. Lett. 142, 119 (1984) Interpretation of this result is considered in references 19 and 20.

[22] H.J. Lipkin, Phys. Lett. 85B, 236 (1979)

[23] H.J. Lipkin, Nucl. Phys. B155, 104 (1979)

[24] L.B. Okun, M.B. Voloshin and V.I. Zakharov, Moscow ITEP preprint ITEP-79 (1979)

[25] P. Aurenche, R. Baier, A.Douiri, M. Fontannaz and D. Schiff, Z. Phys C 24, (1984) 309.

[26] D. W. Duke and J. F. Owens, Phys. Rev. D26, 1600 (1982) Erratum Phys. Rev. D28, 1227 (1983)

[27] T. Jayaraman, G. Rajasekaran and S.D. Rindani, Phys. lett. 119b, 215 1982.

[28] Tung-sheng Tu and Chi-min Wu, Nucl. Phys. B156, 493 (1979)

[29] M. Fontanaz, Talk given at Int. Conf. on High Energy Physics, Lisbon, 1981

[30] J.J. Aubert et al., Phys. Lett. B89, (1980) 267

[31] R.L. Anderson et al., Phys. Rev. Lett. 38, (1977) 263

[32] T. Nash et al., Phys. Rev. Lett. 36, (1976) 1233

[33] U. Camerini et al., Phys. Rev. Lett. 35, (1975) 483

[34] B. Knapp et al., Phys. Rev. Lett. 34, (1975) 1040

[35] B. Gittelman et al., Phys. Rev. Lett. 35, (1975) 1616

[36] C. Seez, Ph. D. Thesis, University of London, 1983.

[37] J. W. Morris, Ph. D. Thesis, University of London, to be published.

[38] F. Lobkowicz, Talk given at 17th Rencontre de Moriond, 1982, vol 2, p185.

[39] R.L. Ford and W.R. Nelson, SLAC-210 (1978)

[40] Compilation of cross-sections π^+,π^-, CERN-HERA-83-01

[41] A.S. Carroll et al, Phys. Letts. 80B (1979) 319.

[42] D.O. Caldwell et al, Phys. Rev. D7 (1973) 1362.

[43] D.O. Caldwell et al, Phys. Rev. Letts., 40 (1978) 1222.

[44] D. Aston et al,Nucl. Phys. B209, (1982) 56.

[45] D. Aston et al,Nucl. Phys. B172, (1980) 1.

[46] T. Ferbel, W.R. Molzon, Rev. Mod. Phys. 56, (1984) 181

[47] Buras and Gaemers, Nucl. Phys. B132 (1978) 249.

[48] Anderson et al, Phys. Rep. 97, (1983) 31

[49] J.C. Lassalle, F. Carena, S. Pensotti, Nucl. Instr. Methods 176, (1978), 371

[50] T. Sjostrand, Computer Phys. Communications, 28 (1983) 229.